

Development of a Novel Diamond Based Detector for Machine Induced Background and Luminosity Measurements

Von der Fakultät für MINT - Mathematik, Informatik, Physik, Elektro- und Informationstechnik
der Brandenburgischen Technischen Universität Cottbus - Senftenberg
zur Erlangung des akademischen Grades eines
Doktors der Naturwissenschaften
(Dr. rer. nat.)

genehmigte Dissertation vorgelegt

von

Master of Science
Maria Hempel

geboren am 28.09.1987 in Berlin

Gutachter: Prof. Dr. Wolfgang Lohmann

Gutachter: Prof. Dr. Rüdiger Schmidt

Gutachtet: Prof. Dr. Jürgen Reif

Tag der mündlichen Prüfung: 6. April 2017

Selbstständigkeitserklärung

Hiermit bestätige ich, Maria Hempel, dass die vorliegende Arbeit selbständig und unter Verwendung der angegebenen Quellen und Hilfsmittel angefertigt wurde.

Zeuthen, 27.09.2016

Maria Hempel

Erklärung über frühere Promotionsanträge

Hiermit versichere ich, Maria Hempel, dass ich bisher noch keinen Antrag für ein Promotionsverfahren eingereicht habe.

Zeuthen, 27.09.2016

Maria Hempel

Erklärung zu Schutzrechten

Hiermit versichere ich, Maria Hempel, dass die Veröffentlichung der Dissertation keine bestehenden Schutzrechte verletzt.

Zeuthen, 27.09.2016

Maria Hempel

Contents

Abbreviations	13
Abstract	16
Kurzfassung	19
1 The Large Hadron Collider LHC	21
1.1 Physics Program of the Large Hadron Collider	21
1.2 Description of LHC Layout	24
1.2.1 Magnets	25
1.2.2 Collimators	27
1.2.3 Beam Loss Monitors	29
1.3 Beam Optics and Structure	30
1.4 Luminosity of a Circular Collider	33
1.5 Machine Induced Background	34
2 The CMS Experiment in Brief	37
3 Beam Radiation, Instrumentation and Luminosity Project	41
3.1 The Fast Beam Condition Monitor BCM1F	42
3.2 Upgrade of BCM1F	45
3.3 BCM1F Signal Processing	47
4 Diamond Detectors	51
4.1 Diamond Properties	51
4.2 Diamond Production	52
4.2.1 Chemical Vapour Deposition	52
4.2.2 Metallization of Diamond Sensors	55
4.3 Signal Generation in Diamond	56
4.3.1 Charge Carrier Drift	61
4.3.2 Signal Generation in the Presence of Defects	63
4.4 Characterization of Diamond Sensors	66
4.4.1 Optical Inspection	67
4.4.2 Leakage Current	70
4.4.3 Signal Stability	71
4.4.4 Charge Collection Efficiency	73
4.5 Characterization Results of NonIrradiated Diamond Sensors	78
4.6 Characterization of Metallization	83
5 Test-Beam of the Upgraded Beam Conditions Monitor	87
5.1 Test-Beam Area	87
5.2 The Pixel Beam Telescope	89
5.3 Setup of the Device Under Test	90
5.4 Test-Beam Offline Analysis	91
5.4.1 Track Reconstruction	92

5.4.2	Data Structure and Statistics	95
6	Results from the Test-Beam	99
6.1	Laboratory Measurements of Diamond Sensor Used for the DUT	99
6.2	Calibration of the Setup	100
6.3	Signal Shape and Impact Position	102
6.4	Charge Collection Efficiency as a Function of Bias Voltage	105
6.5	Charge Collection Efficiency as a Function of Beam Particle Impact Point on the Sensor	108
6.6	Simulations of Test-Beam Studies	110
6.6.1	Simulation of Electrical Field at the Metallization Boarder	110
6.6.2	Simulation of Signal Sharing for Particles Crossing Near the Metallization Gap	112
7	Data Taking with the Beam Condition Monitor	117
7.1	Luminosity	117
7.1.1	Luminosity Estimation	117
7.1.2	Luminosity Measurement	119
7.2	Machine Induced Background	120
7.2.1	Machine Induced Background Estimation	121
7.2.2	Measurements of Machine Induced Background and the Vacuum in the Beam Pipe	122
7.2.3	Machine Induced Background as a Function of Collimator Settings	125
8	Summary and Conclusion	131
	References	141
	Acknowledgment	149

Abbreviations

ADC	Analog-to-Digital Converter
ALICE	A Large Ion Collider Experiment
AOH	Analog Optical Hybrid
ASIC	Application-Specific Integrated Circuit
ATLAS	A Toroidal LHC Apparatus
BCM1F	Fast Beam Condition Monitor
BKGD	Background
BLM	Beam Loss Monitor
CAEN	Costruzioni Apparecchiature Elettroniche Nucleari S.p.A.
CCE	Charge Collection Efficiency
CERN	European Organization for Nuclear Research
CH	Channel
CMS	Compact Muon Solenoid
CVD	Chemical Vapour Deposition
DESY	Deutsches Elektronen-Synchrotron
DUT	Device-Under-Test
EUDAQ	EUDET Data Acquisition
EUDET	Detector R&D Towards the International Linear Collider
EUDRB	EUDET Data Reduction Board
FBCT	Fast Beam Current Transformer
FPGA	Field Programmable Gate Array
FWHM	Full Width at Half Maximum
HF	Hadron Forward Calorimeter
IP	Interaction Point
IR	Insertion Region
LHC	Large Hadron Collider
LHCb	LHC beauty
LTD	Low-Threshold Discriminator
MIB	Machine Induced Background
MIMOSA	Minimum Ionizing MOS Active Pixel Sensor
MIP	Minimum Ionising Particle
MPV	Most Probable Value
pCVD	Polycrystalline CVD Sensor
PLT	Pixel Luminosity Telescope
RHU	Real Time Histogramming Unit
SUSY	Super Symmetry
sCVD	single-crystal CVD Sensor
S/N	Signal-to-Noise Ratio
TCLA	Target Collimator Long Absorber
TCP	Target Collimator Primary
TCSG	Target Collimator Secondary Graphite
TCT	Target Collimator Tertiary
TLU	Trigger Logic Unit
VME	Versa Module Europa (bus or crate)
μ TCA	Micro Telecommunications Computing Architecture

Abstract

The Large Hadron Collider (LHC) is the largest particle accelerator and storage ring in the world, used to investigate fundamentals of particle physics and to develop at the same time the technology of accelerators and detectors. Four main experiments, located around the LHC ring, provide insight into the nature of particles and search for answers to as yet unexplained phenomena in the universe. These four experiments are ATLAS (A Toroidal LHC Apparatus), ALICE (A Large Ion Collider Experiment), CMS (Compact Muon Solenoid) and LHCb (LHC beauty). Two proton or heavy ion beams circulate in the LHC and are brought into collision in the four experiments.

The physics potential of each experiment is determined by the luminosity, which is a ratio of the number of the events during a certain time period to the cross section of a physics process. A measurement of the luminosity is therefore essential to determine the cross section of interesting physics processes.

In addition, safe and high-quality data-taking requires stable beam conditions with almost no beam losses. So-called beam loss monitors are installed in the LHC rings to monitor beam losses around the LHC. Each experiment has in addition its own detectors to measure beam losses, hereafter called machine induced background. One such detector is installed in CMS, the Fast Beam Condition Monitor (BCM1F). Based on diamond sensors it was designed and built to measure both, the luminosity and the machine induced background.

BCM1F ran smoothly during the first LHC running period from 2009-2012 and delivered valuable beam loss and luminosity information to the control rooms of CMS and LHC. At the end of 2012 the LHC was shut down for an upgrade to improve the performance by increasing the proton energy from 4 TeV to 7 TeV and decreasing the proton bunch spacing from 50 ns to 25 ns. Due to the success of BCM1F an upgrade of its sensors and readout components was planned in order to fulfil the new requirements.

The upgrade of the sensors comprises a two pad instead of one pad metallization. 24 instead of the previous 8 single crystal diamond sensors were foreseen for the new BCM1F to enhance the robustness and redundancy. To instrument BCM1F, 59 sensors were electrically characterized by measuring the leakage current, signal stability and charge collection efficiency. Quality criteria were defined to select sensors for the final installation. An overview of these measurements including a summary of the results is given in this thesis.

In addition, an upgraded amplifier was developed within the collaboration in 130 nm CMOS technology. It has a peaking time of 7 ns instead of the 22 ns of the one previously installed. A BCM1F prototype comprising a two pad sensor and the upgraded amplifier was tested at the DESY-II accelerator in a 5 GeV electron beam. Results of these test-beam measurements are presented in this thesis as well as simulations to interpret the measurements.

The installation of the upgraded BCM1F was completed in 2014. In 2015 BCM1F was commissioned and started to measure luminosity and machine induced background. At the end, the thesis will describe both types of measurements with the focus on machine induced background demonstrating the functionality of BCM1F.

Kurzfassung

Der Large Hadron Collider (LHC) ist der größten Teilchenbeschleuniger und -speicherring der Welt. Er wurde gebaut, um Teilchenphysik bei höheren Energien zu erforschen bei gleichzeitiger Entwicklung der Beschleuniger- und Detektorphysik. Vier große Experimente befinden sich am LHC, welche einen Einblick in die grundlegenden Strukturen des Universums und der Teilchenphysik geben. Diese vier Experimente sind ATLAS (A Toroidal LHC Apparatus), ALICE (A Large Ion Collider Experiment), CMS (Compact Muon Solenoid) and LHCb (LHC beauty). Zwei Protonen- oder Schwerionenstrahlen kreisen im LHC und werden in den vier Experimenten zur Kollision gebracht.

Das Physikpotential in den jeweiligen Experimenten wird durch die Luminosität bestimmt. Die Luminosität ist das Verhältnis der Zahl der Ergebnisse während einer bestimmten Zeiteinheit zum Wirkungsquerschnittes eines physikalischen Prozesses. Die Messung der Luminosität ist daher notwendig, um die Wirkungsquerschnitte interessanter Prozesse zu messen. Eine sichere und hochwertige Datennahmen benötigt stabile Strahlbedingungen, möglichst ohne Strahlverluste. So genannte Strahlverlustmonitore sind im LHC installiert, um Strahlverluste um den LHC Ring anzuzeigen. Jedes Experiment hat zusätzlich seine eigenen Detektoren. Einer dieser Detektoren im CMS ist der Fast Beam Condition Monitor (BCM1F), welcher Diamantsensoren verwendet.

BCM1F ist in der ersten LHC Laufzeit von 2009-2012 problemlos gelaufen und lieferte wertvolle Strahlverlust- und Luminositätsinformationen zum CMS- und LHC-Kontrollraum. Ende 2012 beendete der LHC seinen Betrieb für das Upgrade von 4 TeV auf 7 TeV und der Reduzierung des Abstandes der Protonenpakete von 50 ns auf 25 ns. Um diese neuen Anforderungen zu erfüllen, wurde ein Upgrade der BCM1F Sensoren und Ausleseelektronik durchgeführt.

Auf die Oberfläche der Sensoren wurden zwei Metallelektroden, genannt Pads, aufgebracht, um die Zählrate zu halbieren. Die Robustheit und Redundanz von BCM1F wurde gesteigert, indem die Anzahl der Sensoren von 8 auf 24 erhöht wurde. Insgesamt wurden 59 Sensoren elektrisch charakterisiert, was Messungen von Leckstrom, Signalstabilität und Ladungssammlungseffizienz beinhaltet. Qualitätskriterien für die Auswahl von Sensoren wurden definiert. Ein Überblick dieser Messungen wird mit einer Zusammenfassung der Resultate in dieser Arbeit gegeben.

Zusätzlich wird ein verbesserter Verstärker in 130 nm CMOS Technologie und einer Anstiegszeit der Ausgangsspannung (proportional zur Eingangsspannung) von 7 ns, statt der vorherigen 22 ns, zur Signalauslese verwendet. Ein BCM1F Prototyp mit Zweikanalauslese und dem verbesserten Verstärker wurde am DESY-II Beschleuniger bei einem Elektronenstrahl von 5 GeV Elektronen getestet. Resultate dieses Testes werden in dieser Arbeit gezeigt und mit Simulationen verglichen. Die Installation des neuen BCM1F Systems fand 2014 statt und 2015 startete BCM1F seine Messungen der Luminosität und der Rate von Teilchen des Strahlhintergrundes, der im Beschleuniger anfällt. Am Ende wird diese Arbeit Resultate der Messungen zeigen, sich dabei aber auf den maschinen-induzierten Hintergrund konzentrieren und dabei die sichere Funktionsweise von BCM1F demonstrieren.

1 The Large Hadron Collider LHC

The LHC is a particle accelerator and storage ring for protons or heavy ions located close to Geneva at CERN. It is about 100m underground with a circumference of 27km. The main purpose of the LHC is to answer fundamental questions in particle physics such as “What is mass?”, “Why are we made out of matter?” and “What happened just after the time of the big bang?”. To answer these questions two counter-rotating hadron beams are brought into collision in the four main experiments ATLAS, ALICE, CMS and LHCb. ATLAS and CMS are two multi-purpose experiments to search for new physics and investigating the previously found Higgs particle [1, 2]. ALICE investigates the condition right after the big bang by using heavy ion collisions, creating a quark-gluon plasma similar to the condition in the early universe. LHCb is specialized to investigate slight differences of matter and antimatter by studying b quarks produced during the collision.

The LHC was designed to collide two 7 TeV proton beams containing 2808 bunches each with a bunch spacing of 25 ns and having a nominal peak luminosity of $1 \cdot 10^{34} \text{ cm}^{-2} \text{ s}^{-1}$. Each bunch contains $1.15 \cdot 10^{11}$ protons and stores an energy of 362 MJ comparable to 100 kg of TNT [3]. Just after the first start in 2008 a faulty electrical connection caused a mechanical damage in one of the magnets. After a reparation phase the LHC restarted its operation in 2009 but with more relaxed beam parameters ensuring a high safety margin. During the first LHC long run (Run 1) the beam parameters converged to the nominal settings but still had around half of the beam energy and number of bunches. In beginning of 2013 the LHC was shut down for a long stop (LS1) to upgrade the LHC ring and its devices in order to increase the beam energy and the number of bunches. The LHC started then its second run in 2015, with the parameters given in Table 1 being very close to the nominal parameters [4].

It has to be pointed out that a pilot bunch with a lower intensity of 10^9 protons is sometimes injected into the LHC after a commissioning or when the LHC changes one of the listed parameters. This is done for probing the settings and testing the machine protection margins.

LHC Parameter	Designed	2012	2016
beam energy [TeV]	7	4	6.5
number of bunches	2808	1380	2064
Protons per bunch [10^{11}]	1.15	1.7	1.2
peak luminosity [$\text{cm}^{-2} \text{s}^{-1}$]	$1 \cdot 10^{34}$	$7.7 \cdot 10^{33}$	$1.2 \cdot 10^{34}$
β^* at IP1 and IP5 [m]	0.55	0.6	0.4
bunch spacing [ns]	25	50	25
RF frequency [MHz]	400.8	400.8	400.8
Revolution time [μs]	88.93	88.93	88.93

Table 1: Comparison of the nominal LHC parameters with the operational ones in Run 1 (2012) and Run 2 (2016).

1.1 Physics Program of the Large Hadron Collider

One of the major tasks of the LHC is to probe the Standard Model which describes the elementary particles that matter is made of. These particles occur in two groups, leptons and quarks. Each group consists of six particles which are classified in generations. The first generation is given by the lightest and most stable particles, the “up” and “down” quarks and the electron with its electron-neutrino. All stable matter in the universe is made out of particles from the first generation.

The second and third generations include all heavier and non-stable fundamental particles which decay into lighter particles. An illustration of all quarks, leptons and their generations is given in Figure 1. Particles of all three generations have a half-integer spin and are called Fermions. All matter particles interact with each other by exchanging gauge bosons that are associated to one of the three forces, the strong (gluon), electromagnetic (photon) and weak force (W and Z boson). The strong force is only experienced by quarks and gluons. However, the Standard Model only works if the predicted Higgs boson exists. The Higgs mechanism breaks the electroweak symmetry. The consequence is that the W and Z bosons are heavy and γ is massless. An excitation of the Higgs field, the Higgs boson, is predicted. In addition, Fermions acquire mass due to the Yukawa coupling to the Higgs field [5,6].

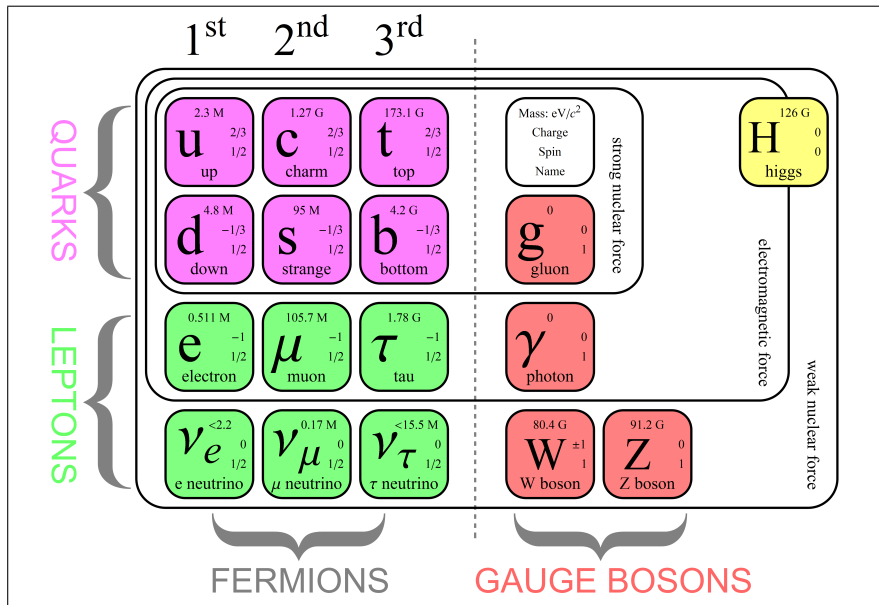


Figure 1: Illustration of the Standard Model containing fermions and bosons (taken from [7]).

The four production mechanisms of the Higgs boson at the LHC are gluon fusion, weak-boson fusion, Higgs-strahlung and associated production with top quarks as illustrated in Figure 2. The gluon fusion process has the largest cross section mediated by a virtual heavy top quark loop. The second largest cross section is present for the vector boson fusion, where two quarks emit a W or Z fusing to a Higgs boson. An even smaller cross section is measured for the Higgs production in Higgs-strahlung and association with $t\bar{t}$.

In 2012 the ATLAS and CMS experiment published the observation of a new boson with the mass of 125 GeV and one year later in 2013 the physicists became confident that they have found the Higgs boson. Its properties as so far known are the same as predicted in the Standard Model [1,2,8]. This result was a milestone in the understanding of particle physics. The Higgs boson is observed in different decay channels with the corresponding branching fractions as listed in Table 2. The most important one is the $H \rightarrow \gamma\gamma$ since only two photons with high energy are produced and the mass resolution is high. However, this channel has a large background due to prompt $\gamma\gamma$ production and other processes producing photons. A similar mass resolution is reached in the channel $H \rightarrow ZZ \rightarrow l^+l^-l'^+l'^-$ ($l, l' = e, \mu$) having a smaller background ($q\bar{q} \rightarrow ZZ \rightarrow 4l$) and a higher branching fraction.

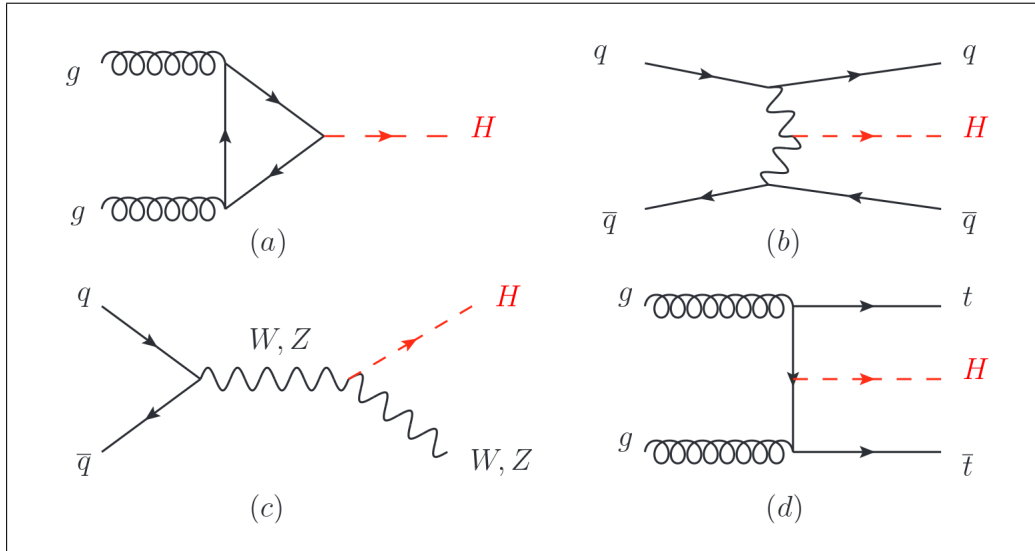


Figure 2: Feynman diagrams for Higgs production by (a) gluon fusion, (b) weak-boson fusion, (c) Higgs-strahlung and (d) associated production with top quarks.

While the branching fraction of $H \rightarrow W^+W^- \rightarrow l^+\nu_l l'^-\nu_{l'}$ is large, the mass resolution is poor due to the produced neutrinos¹. The other listed channels suffer from large background and a worse mass resolution. In the channel $H \rightarrow \tau^+\tau^-$ the tau leptons decay rapidly and produce as well neutrinos $\tau^- \rightarrow \mu^- \bar{\nu}_\mu \nu_\tau, e^- \bar{\nu}_e \nu_\tau$.

Decay Channel	Branching Fraction	Mass Resolution
$H \rightarrow \gamma\gamma$	$2.28 \cdot 10^{-3}$	1-2%
$H \rightarrow ZZ \rightarrow l^+l^-l'^+l'^-$	$2.64 \cdot 10^{-2}$	1-2%
$H \rightarrow W^+W^- \rightarrow l^+\nu_l l'^-\nu_{l'}$	$2.15 \cdot 10^{-1}$	20%
$H \rightarrow b\bar{b}$	$5.77 \cdot 10^{-1}$	10%
$H \rightarrow \tau^+\tau^-$	$6.32 \cdot 10^{-2}$	15%

Table 2: Decay channels of Higgs boson with their branching fractions and the mass resolution when reconstructing the mass of the Higgs boson from the decay products.

The discovery of the Higgs boson is however not the end of the research at the LHC. A spin of 0 and a parity of +1 represented as 0^+ of the Higgs boson is predicted by the Standard Model. So far the data of ATLAS and CMS are consistent with a 0^+ Higgs boson, but further data is taken to confirm it [9, 10]. The CP transformation² combines charge conjugation C with parity P and needs also studied in detail. In addition, the self coupling of the Higgs boson when producing a Higgs boson pair has to be studied in detail since it is an important direct probe of the Higgs potential given by the Standard Model. This process interferes negatively with a Higgs boson pair production through a top-quark and b-quark loop [11, 12].

However, the Standard Model does not explain other phenomena like the Dark Matter. Hence physics beyond the Standard Model is expected. So called Super Symmetric (SUSY) particles are one candidate for Dark Matter and the search at the LHC is ongoing. The SUSY model also predicts additional neutral and charged Higgs bosons and the search has already begun [13]. The

¹Neutrinos cannot be directly detected and are reconstructed by missing energy.

²Particles and antiparticles are interchanged by conjugating the internal quantum number as the charge and the handedness of space is reversed.

neutral Higgs bosons have a different CP quantum number. There are still many open questions to be answered by the usage of the LHC and its experiments. For all these studies data of high-quality and the measurement of the cross sections are of utmost importance.

1.2 Description of LHC Layout

The LHC ring is sectioned in eight insertion regions (IR) having arc and straight sections as illustrated in Figure 3. Each arc section connects two straight sections and is equipped with dipole magnets. The four experiments ATLAS in IR1, ALICE in IR2, CMS in IR5 and LHCb in IR8 are located at the straight sections having the intersection points (IP) in the middle. The other four straight sections contain the two collimator systems to absorb most of the beam losses (IR7), the accelerating radio-frequency (RF) system (IR4), beam instrumentation (IR3) and the beam dumping system (IR6) to extract the beam in case of an end of the fill or adverse beam conditions. However, before the protons are used in the LHC they need to be pre-accelerated in the accelerator complex shown in Figure 4.

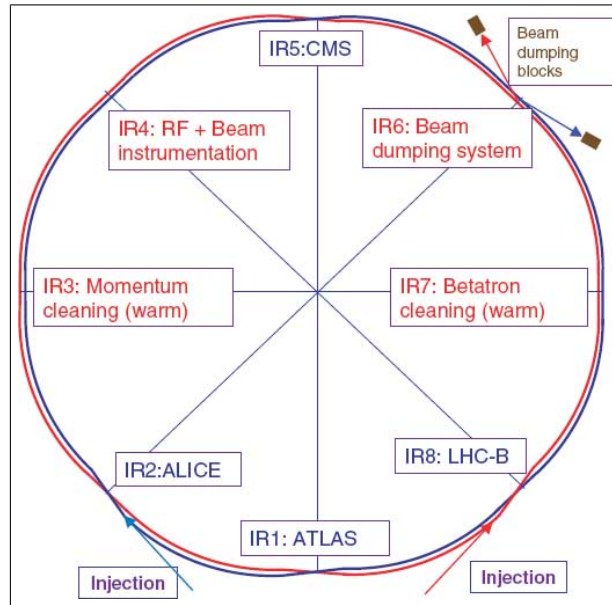


Figure 3: Schematic of the sectioning of the LHC with its eight insertion regions.

Protons coming from a hydrogen source are first accelerated in the Linear Accelerator 2 (LINAC2) up to an energy of 50 MeV before they are then transferred to the Proton Synchrotron Booster (BOOSTER) where a maximum energy of 1.4 GeV is reached. The BOOSTER consists of four individual rings that are equally filled with proton bunches. Bunches from all four rings are then injected to the Proton Synchrotron (PS) and accelerated to 26 GeV. After the PS the bunches are transferred to the Super Proton Synchrotron (SPS) which brings them to an energy of 450 GeV being sufficient for injecting them into the two final LHC rings. The two transfer lines from the SPS to the LHC are located at the ALICE (IR2) and LHCb (IR8) experiments to realise the two beams rotating in opposite directions. Beam 1 is given by bunches rotating clockwise and beam 2 by bunches rotating anti-clockwise.

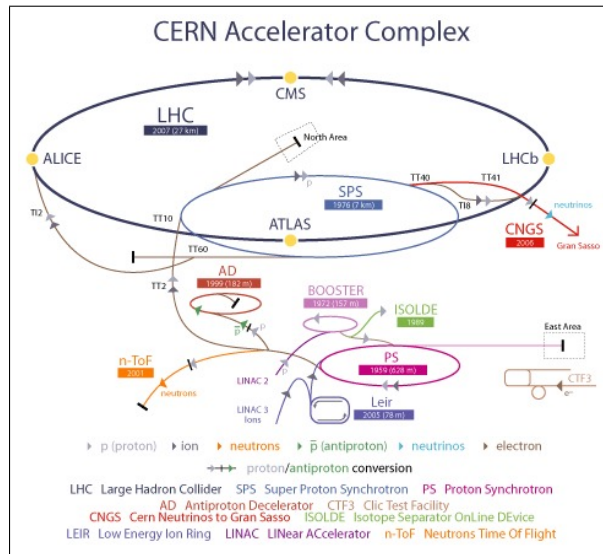


Figure 4: Accelerator complex of the LHC including the main pre-accelerators LINAC2, BOOSTER, PS and SPS.

The final bunch scheme being in the LHC ring is shown in Figure 5 where several bunches spaced by 25 ns form one bunch train. Between two bunch trains is a bunch free time interval of 300 ns (12 times 25 ns). This time is needed to rise the PS ejection kicker. After three or four trains is an additional bunch free gap of around 1 μ s called injection gap corresponding to the rise time of the LHC injection kicker magnet [14]. Between the last and the first bunch is a so called abort gap of 3 μ s that is used to deflect the bunches from the LHC to the dumping system by a dump kicker magnet. This ensures to extract the bunches without uncontrolled particle losses caused by deflection.

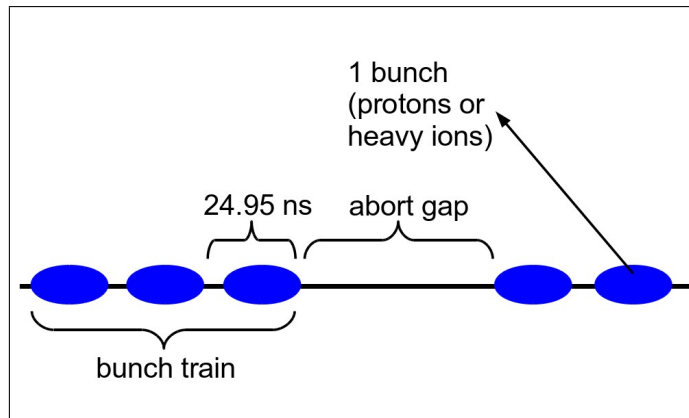


Figure 5: Illustration of the LHC bunch structure containing the abort gap between the very last and first bunch in the LHC ring.

1.2.1 Magnets

The LHC ring is instrumented with dipole magnets keeping the particles on the circular track and ensuring the steering of particles around the ring. Mostly sector magnets are used where the particle enters and leaves the dipole with 90° as shown in Figure 6.

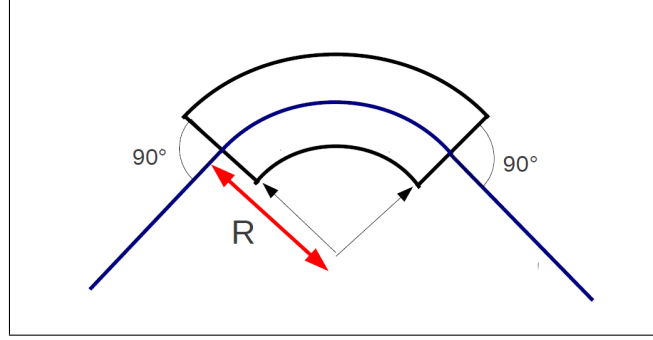


Figure 6: Particle trajectory bended by a sector magnet.

The magnetic field of this dipole is set such that the bending radius R is ensured. In order to get the magnetic field strength, a Cartesian Coordinate is defined by $C = (x, y, s)$ where s is the beam direction of a ring. The particle moves now parallel to the beam direction with the velocity $\vec{v} = (0, 0, v_s)$ and is bent by the magnetic field $\vec{B} = (B_x, B_y, 0)$. The resulting Lorentz force on the particle with the charge q and the mass m is then

$$\vec{F} = q(\vec{v} \times \vec{B}) \quad (1.1)$$

$$F_x = -qv_s B_y . \quad (1.2)$$

This force is of course equal to the centrifugal force F_R

$$F_R = \frac{mv_s}{R} , \quad (1.3)$$

resulting with the momentum $p = mv_s$ in

$$\frac{1}{R} = \frac{q}{p} B_y . \quad (1.4)$$

If however the particle is displaced from the nominal trajectory higher order multi-poles become important which are treated by using Taylor series:

$$\frac{q}{p} B_y = \frac{q}{p} B_{y0} + \frac{q}{p} \frac{dB_y}{dx} x + \frac{1}{2!} \frac{d^2 B_y}{dx^2} x^2 + \dots \quad (1.5)$$

$$= \underbrace{\frac{1}{R}}_{\text{dipole}} + \underbrace{kx}_{\text{quadrupole}} + \underbrace{\frac{1}{2!} l x^2}_{\text{sextupole}} + \dots , \quad (1.6)$$

$$(1.7)$$

where k is the quadrupole and l sextupole strength. Despite of dipoles also quadrupoles and sextupoles become important in this case. A quadrupole as shown in Figure 7 focus the beam in the vertical direction and defocus in the horizontal direction for a positive charge moving into the plane. A focusing in the horizontal beam direction for the given example is done by rotating the

quadrupole by 90° . Focusing and defocusing quadrupoles are installed in the LHC to ensure strong focusing of the beams in the horizontal and vertical beam direction [15]. Sextupoles are installed as well in the LHC to compensate large deviation in the particle momentum.

The LHC uses superconducting magnets made of Nb-Ti cooled down below the critical temperature of 9.2K. Above the critical temperature the magnets become normal conducting. The transition from superconductivity to normal conductivity is called quenching. To bend a proton with 7 TeV energy a magnetic field of 8.3 T is needed. This requires an operation temperature of 2 K that is only be reached by superfluid helium. The operation temperature is set to take into account a temperature increase caused by energy deposition. An energy deposition as beam losses of only a few mJ/cm^3 are sufficient to quench a magnet. Since beam losses cannot be avoided an interception of them is necessary.

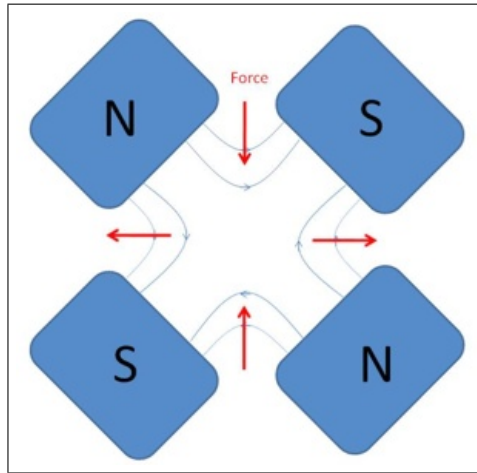


Figure 7: Magnetic field of a quadrupole focusing in the vertical and defocusing the horizontal direction.

1.2.2 Collimators

In order to intercept beam losses, collimators are installed around the LHC ring. They consist of two jaws and absorb as much energy as possible. Collimators are placed between the beam and the vacuum pipe to absorb particles having a large deviation from the nominal trajectory. The distance between the beam centre and the surface of the collimator jaw is the half-opening gap and given in units of σ , the Gaussian beam width, with $\sigma = 0.2 \text{ mm}$ [16]. Depending on the type of collimator the material and half-opening gap differs. One example of a collimator is shown Figure 8. This collimator intercepts beam losses appearing in the horizontal beam direction. In addition, collimators being 45° and 90° rotated are installed to intercept beam losses from any beam direction. All in all, 118 collimators are placed along the LHC rings and most of them are given in Figure 9. Collimators before and after the four LHC experiments are placed to prevent the experiments from large beam losses and to absorb luminosity debris. In addition, several collimators are placed around the injection in IR2 and extraction in IR6 areas to intercept beam losses in the case of a failure during the injection/extraction process. An accumulation of collimators is located at the beam cleaning region in IR3 and IR7. Particles having a large deviation from the nominal momentum are intercepted in IR3 and particles having a large deviation from the nominal trajectory are absorbed in IR7.

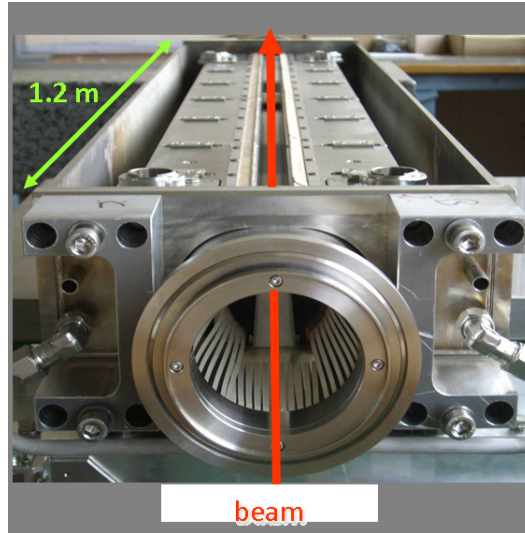


Figure 8: Photo of a collimator with an illustration of the beam trajectory between the two collimator jaws.

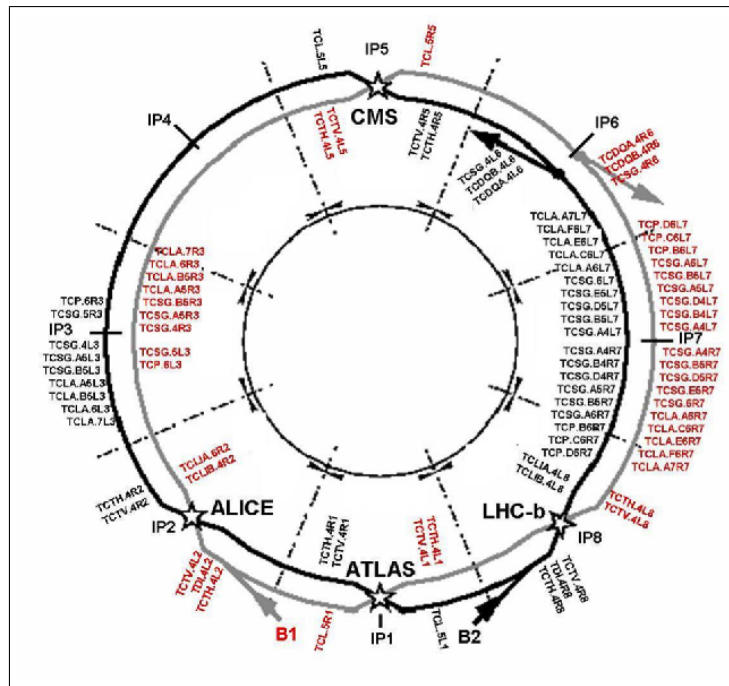


Figure 9: Locations of collimators in the LHC ring with a concentration around IR7 (taken from Reference [17]).

The beam cleaning is done by three different types of collimators. First, the beam loss particles hit the primary collimator (TCP) being made of a carbon fibre composite making them extremely robust. The beam losses interact with the material and the secondary particles hit then the secondary collimator (TSCG). These ones are as well made out of a carbon fibre composite and interactions take again place. The shower produced in the TSCG is afterwards absorbed in the tertiary collimator (TCT) or an absorber (TCLA). These collimators are made of a high-Z material

like tungsten to absorb as much energy as possible [17]. An illustration of the beam loss cleaning is shown in Figure 10. It is clearly visible that the half opening gap is the smallest for the TCP and becomes larger with the TSCG and TCT/TCLA. This avoids high energetic particles hitting the TCT/TCLA since they are sensitive to beam damage.

Especially the TCT and TCLA around CMS become later important since particles hitting these collimators produces as well a secondary shower entering the CMS experiment (see Chapter 1.5).

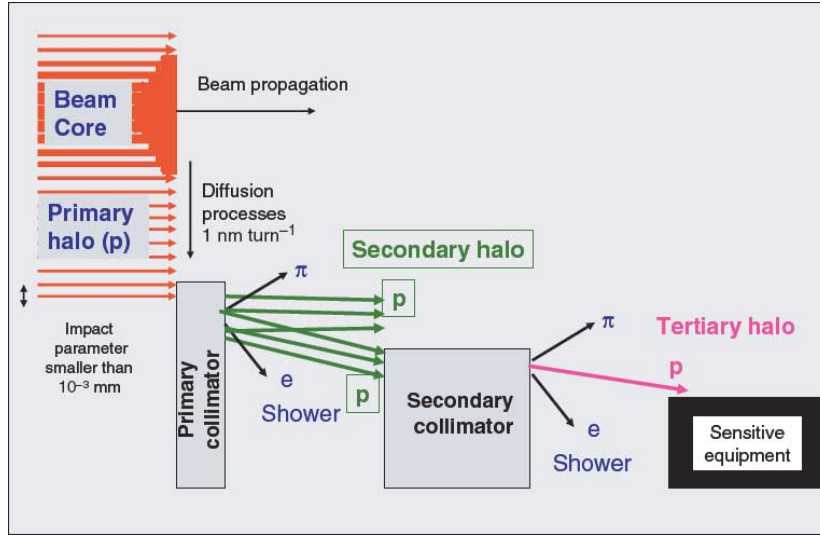


Figure 10: Layout of the beam cleaning containing three types of collimators primary, secondary and tertiary (taken from Reference [3]).

1.2.3 Beam Loss Monitors

In order to measure the amount of beam loss particles, so called beam loss monitors (BLM) are installed at collimators or critical loss locations as for example the superconducting magnets. Ionization chambers as shown in Figure 11 are used. They are installed outside of a dipole magnet [18]. Each ionization chamber is 50 cm long and has a diameter of 9 cm. Inside there are several parallel aluminium plates being separated by 0.5 cm allowing to generate an electrical field. Ionisation chambers are filled with nitrogen at a pressure of 100 mbar. If secondary particles created by the beam loss cross the ionization chamber they ionize the gas creating a signal of a size depending on the amount of particles crossing. In the case the signal reaches a certain threshold the system initiates a beam dump to avoid magnet quenching or damage of LHC material as vacuum pipes or detectors. All in all, around 3700 of the BLMs are installed in the LHC machine to measure the amount of beam losses and to protect the LHC in case of adverse beam condition [19]. Diamond based beam loss monitors are as well installed in the LHC ring as given in Reference [20] having the same working principle. This thesis will focus on the diamond based beam loss monitors installed in CMS. A comparison of beam loss measurements with diamond sensors and BLMs is done in Chapter 7.2.



Figure 11: Ionization chambers in the little yellow cylinders and installed outside of a dipole magnet (taken from Reference [18]).

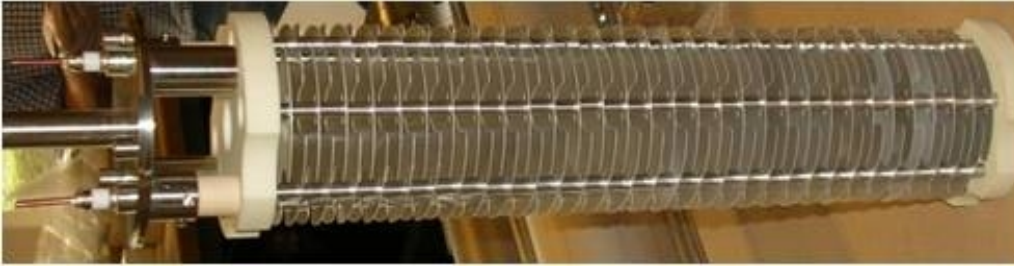


Figure 12: Photo of an ionization chamber showing the electrode plates.

1.3 Beam Optics and Structure

The understanding of the cause of beam losses is derived from the calculation of a particle trajectory in a circular ring. The ring structure and instrumentation along the ring defines the designed trajectory being called design orbit. However, the particles in the LHC pass through the magnetic field structure defining the nominal trajectory called closed orbit. The closed orbit is periodically and all particles follow the same trajectory in each turn. Nevertheless, any angular divergence causes a deviation from the closed orbit and the particles start to oscillate around the closed orbit. This oscillation is called betatron oscillation. In the following the betatron oscillation is shortly described. More details can be found in Reference [21].

It is assumed that a particle moves on a trajectory being in the vicinity of the closed orbit through a magnetic structure of quadrupoles and dipoles. Again the Cartesian coordinates $C = (x, y, s)$ are used where s is the closed orbit as illustrated in Figure 13. The magnetic field has again only a x - and y -component (see Chapter 1.2.1). The equation of motion is then given by:

$$x''(s) + \left(\frac{1}{R^2(s)} - k(s) \right) x(s) = \frac{1}{R(s)} \frac{\Delta p}{p} \quad (1.8)$$

$$y''(s) + k(s) y(s) = 0, \quad (1.9)$$

where x and y is the deviation from the closed orbit in the x- and y-direction with a dipole impact only in the x-direction causing a bending radius of R . The quadrupole impacts the vertical and horizontal direction with the field strength k . Equation 1.8 takes into account as well a small momentum deviation Δp from the nominal momentum p_0 resulting in a particle momentum of $p = p_0 + \Delta p$.

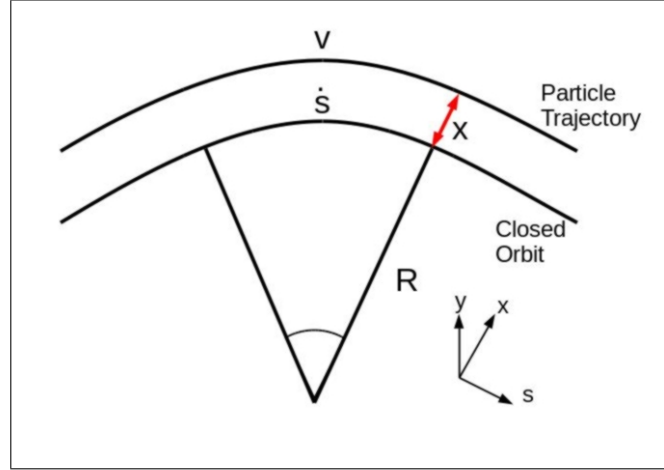


Figure 13: Illustration of particle movement relative to the closed orbit. The particle velocity is given by v .

Equation 1.8 is now simplified by assuming a large bending radius $1/R = 0$ and a very small momentum deviation $\Delta p/p = 0$:

$$x''(s) - k(s)x(s) = 0. \quad (1.10)$$

The solution of this equation is the previously mentioned betatron oscillation in the x-direction

$$x(s) = Au(s) \cos(\Psi(s) + \Phi), \quad (1.11)$$

where $Au(s)$ is the amplitude of the oscillation and $\Psi(s)$ the phase containing $k(s)$. In the same way the betatron oscillation in the y-direction is described. Both the amplitude and phase of the oscillation depend on the location s since the magnetic field strength is different for each magnet. Φ is however a constant phase of the oscillation. Summarizing, particles having an angular divergence oscillate around the closed orbit with the amplitude $Au(s)$ and the phase $\Psi(s)$. The constant part of the amplitude A is also defined as

$$A = \sqrt{\epsilon}, \quad (1.12)$$

with the emittance ϵ [22]. It represents the beam size that is small if ϵ is small. In addition, the amplitude $u(s)$ is given by

$$u(s) = \sqrt{\beta(s)}, \quad (1.13)$$

where $\beta(s)$ is called the betatron function and defined by the LHC magnet structure depending on s and the focusing. Often the quantity β^* is used being the betatron function at the interaction points of the experiments. Finally, the equation of motion becomes:

$$x(s) = \sqrt{\epsilon} \sqrt{\beta(s)} \cos(\Psi(s) + \Phi). \quad (1.14)$$

It has to be pointed out that the trajectories of all particles lie within a range quoted as the envelope $E(s) = \sqrt{\epsilon} \sqrt{\beta(s)}$. This fact is illustrated for one particle trajectory and many of them in Figure 14. The envelope defines at the end the transverse beam size as the function of s .

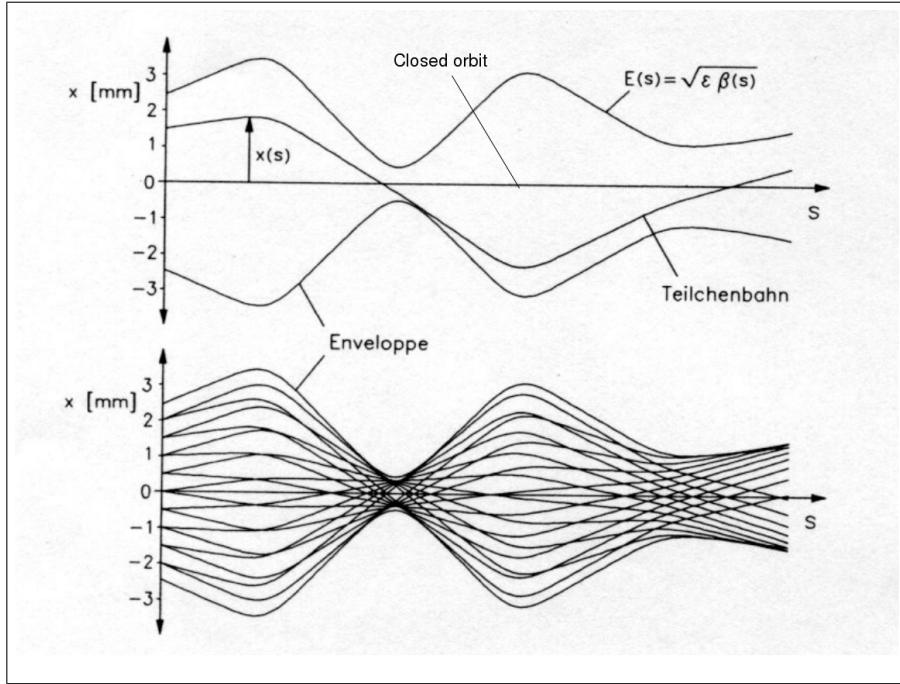


Figure 14: Betatron oscillation and its envelope (taken from Reference [21]).

This raises the question of how the particles within a bunch are distributed. A good approximation for the charge density $\rho(x, y)$ in the vertical and horizontal beam direction is the Gaussian distribution given by

$$\rho(x, y) = \frac{Ne}{2\pi\sigma_x\sigma_y} \exp\left(-\frac{x^2}{2\sigma_x^2} - \frac{y^2}{2\sigma_y^2}\right), \quad (1.15)$$

where Ne is the total charge within a bunch and $\sigma_{x/y}$ the vertical and horizontal beam size corresponding to one standard deviation. The beam size $\sigma(s)$ is related to the emittance as:

$$\sigma(s) = \sqrt{\epsilon\beta(s)} \quad (1.16)$$

$$\rightarrow \epsilon = \frac{\sigma^2(s)}{\beta(s)}. \quad (1.17)$$

Equation 1.17 will be later important to obtain the luminosity.

1.4 Luminosity of a Circular Collider

The luminosity is the key parameter to determine the cross section σ_p of a certain relevant physics process being defined as

$$\sigma_p = \frac{\dot{N}_p}{L}, \quad (1.18)$$

where L is the luminosity and \dot{N}_p the production rate of events of the process. We assume now proton bunches with the previous mentioned Gaussian particle density distribution in the x-y plane [21]. The surface density n_2 of one bunch with the number of particles N_2 of beam 2 is then given as

$$n_2 = \frac{\partial^2 N_2}{\partial x \partial y} \quad (1.19)$$

$$= \frac{N_2}{2\pi\sigma_x\sigma_y} \exp\left(-\frac{x^2}{2\sigma_x^2} - \frac{y^2}{2\sigma_y^2}\right). \quad (1.20)$$

The surface density for beam 1 is obtained by replacing N_2 by N_1 . If now b bunches from beam 1 and beam 2 with a revolution frequency f_{rev} crossing each other within the surface element $dA = dxdy$, the differential event rate $d\dot{N}_p$ of a physics process depends on its cross section σ_p and the surface density of the colliding bunches:

$$d\dot{N}_p = \sigma_p b f_{rev} n_1 n_2 dxdy \quad (1.21)$$

$$= \sigma_p \frac{b f_{rev} N_1 N_2}{(2\pi)^2 \sigma_x^2 \sigma_y^2} \exp\left(-\frac{x^2}{\sigma_x^2} - \frac{y^2}{\sigma_y^2}\right) dxdy. \quad (1.22)$$

The integral is solved by

$$\int \exp\left(\frac{-x^2}{\sigma^2}\right) dx = \sqrt{\pi}\sigma. \quad (1.23)$$

The total event rate becomes then:

$$\dot{N}_p = \sigma_p \frac{b f_{rev} N_1 N_2}{4\pi\sigma_x\sigma_y}. \quad (1.24)$$

A comparison of Equation 1.18 and 1.24 leads to the following expression for the luminosity:

$$L = \frac{bf_{rev} N_1 N_2}{4\pi \sigma_x \sigma_y} . \quad (1.25)$$

Often the integrated luminosity is given being defined as the integral of the luminosity over a certain time interval:

$$L_{int} = \int_{t_1}^{t_2} L dt . \quad (1.26)$$

The vertical and horizontal bunch size is often quoted as bunch cross sections and its product is the effective transverse area $A_{eff} = 2\pi\sigma_x\sigma_y$. The aim of the LHC operation is to have the highest possible luminosity in order to have as much as possible events of interesting physic processes and to analyse them within a reasonable time. An optimization of the luminosity is done by reducing the betatron amplitude at the interaction point since the bunch size at the interaction point depends on its betatron function (see Equation 1.17):

$$L = \frac{bf_{rev} N_1 N_2}{4\pi \beta^* \epsilon} . \quad (1.27)$$

A reduction of the emittance increase the luminosity as well. However, this requires a tuning of the emittance during the creation of the bunches in the pre-accelerators.

1.5 Machine Induced Background

The so called machine induced background (MIB) is monitored to give information about the LHC performance. MIB are particles hitting the detector but are not collision products originating from the interaction point. Various sources are responsible for the MIB and can be summarized as beam losses. One source of beam losses are deflected bunch particles. This happens if bunch particles scatter on residual gas atoms in the vacuum chamber. Beam losses from this source are also quoted as beam gas interactions. A deflection by a micro particle detached from the vacuum chamber falling into the beam is another source called Unidentified Falling Object (UFO). The deflected beam particles can now generate a signal in a detector or they are intercepted by the collimators since the deflection causes an increased betatron amplitude. If such beam losses appear near the CMS experiment then the secondary particles created behind the collimator may enter the CMS experiment and generate signals in various detectors. Also other mechanisms of beam losses exist but the above mentioned are the most important ones for this thesis and the later measurements. A detailed description of additional beam loss sources is given in Reference [23].

The MIB depends also on the vacuum pressure since a higher amount of residual gas particles lead to an increased number of bunch particles being deflected. The so called electron-clouds increase the vacuum pressure [24]. Electron-clouds are created by synchrotron light from the bunch particles releasing electrons from the vacuum chamber wall. These electrons are accelerated by the electric field of the beam and can hit the vacuum chamber releasing a second electron as illustrated in Figure 15. Also the secondary electron is accelerated by subsequent bunches leading to a build-up

of a cloud of electrons around the beam [25]. Such electrons can potentially detach particles from the vacuum chamber causing beam losses and a vacuum pressure increase.

It is crucial to monitor the MIB and to dump the beam in case of adverse beam condition in order to avoid magnet quenches or damage on any material in the LHC ring and its experiments (ATLAS, ALICE, CMS and LHCb). A monitoring of the MIB allows a better understanding of the sources helping to avoid or reduce them. In addition, a feedback of the MIB to the CMS pixel detector is essential since they start their system if the MIB is below a certain threshold (see Chapter 2). MIB particles traverse the CMS pixel detector and produce a huge number of signals having a long readout time. This causes a long dead time of around 10% leading to a reduced efficiency of data taking and track reconstruction.

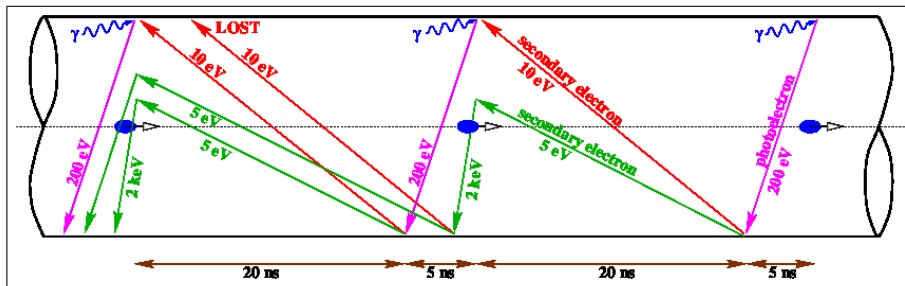


Figure 15: Illustration of electron cloud caused by synchrotron light producing photo-electrons.

2 The CMS Experiment in Brief

One of the larger experiments at the LHC is CMS being a multipurpose detector symmetrically build around the interaction point at IR5. The design is driven by the choice of the magnetic field that needs to be large enough to bend the trajectory of particle created during collision to precisely measure the momentum even at high energies [26]. Different sub-detector layers within the CMS experiment are needed in order to reconstruct the collision products, their charges, momenta and energies. An illustration of all layers within CMS is given in Figure 16. The most inner layer is the pixel detector followed by the silicon tracker. These two layers are used for the track reconstruction of charged particles and to determine their charge and momenta. The next layers are the electromagnetic and hadronic calorimeter that quantify the particle energy. The superconducting solenoid, situated around the hadronic calorimeter, is generating a magnetic field of 3.8 T. The outermost detectors are the muon chambers for detecting muons and to measure their charges and momenta. In the following each subdetector is described in more detail.

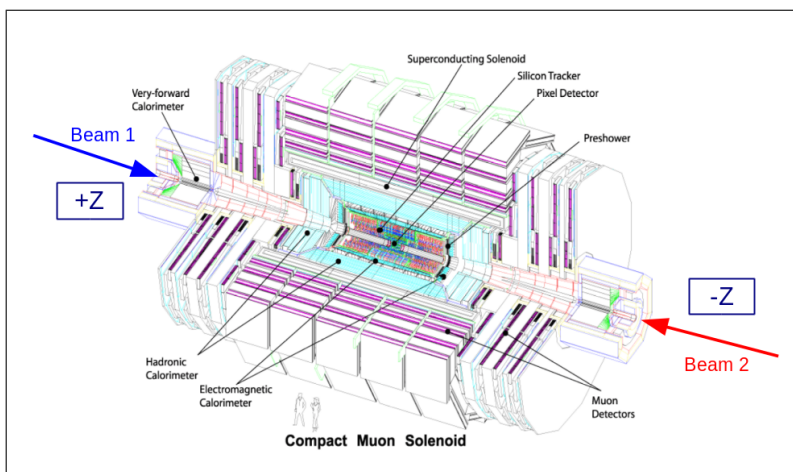


Figure 16: Layout of CMS with its components. The z-axis points in the direction of beam 2 and the x-axis to the center of LHC.

Pixel Detector

The pixel detector consists of 3 cylinders and two end-cap layers of silicon pixel sensors and is located very close to the CMS interaction point. It measures the tracks of charged particles and is particularly important for the measurement of primary and secondary vertices³ in a collision [27]. The cylinders with a length of 53 cm are placed at radii of 4.4, 7.3 and 10.2 cm. Each pixel cell has a size of $100 \times 150 \mu\text{m}^2$ and a resolution of the track position of $180 \mu\text{m}$ in the azimuthal angle φ and of $30 \mu\text{m}$ in z [28]. The high spatial resolution in φ is possible due to the high magnetic field causing a Lorentz drift of the charged particles and leading to a signal charge spread over more than one pixel. In order to reduce the occupancy of the pixels, it is only switched on if the MIB is below a certain level. It allows a separation of particles originating from different primary vertices and to reconstruct the path of short living particles. In addition, it allows to trigger on events with secondary vertices.

³The primary vertex is the location of the particle collision. Secondary vertices are created by collision products decaying further away from the interaction point.

Silicon Tracker

The radial region between 20-116 cm is occupied with the silicon strip detector having three different sub-systems, the tracker inner barrel and disk, the tracker outer barrel and the tracker end-caps. The previously mentioned pixel detector is surrounded by the tracker inner barrel with 4 barrel layers and a disk with 3 layers respectively. Then the tracker outer barrel follows with 6 barrel layers and the tracker end-caps with 9 layers on each side, respectively. Depending on the sub-system and layer the strip pitch varies from 80 to 184 μm as well as the single point resolution from 23-53 μm [29]. The total silicon detector area amounts to 198 m^2 . Due to the strong magnetic field and the high precision space point measurement the transverse momentum is measured with high resolution. Also the tracker is only switched on when the MIB is small enough in order not to enhance the occupancy of the strip channels.

Electromagnetic Calorimeter

The electromagnetic calorimeter is made of lead tungstate (PbWO_4) crystals with 61,200 in the barrel and 7,324 in each of the two end-caps. The photodetectors for the barrel crystals are avalanche photodiodes made out of silicon [30]. However, the end-cap region has a much higher gamma and neutron radiation field and therefore vacuum phototriodes are used [31]. The electromagnetic calorimeter is designed to determine the energy of photons and electrons with high precision. The measurements of photons is essential to reconstruct Higgs bosons in the decay of $H \rightarrow \gamma\gamma$.

Hadronic Calorimeter

The electromagnetic calorimeter is surrounded by a hadronic calorimeter to determine the energy of hadronic jets⁴ or neutral hadrons like the neutron [32]. The hadronic calorimeter is a sampling calorimeter consisting of absorbers and scintillators. Absorber layers are made of steel in the barrel region and of brass in the end caps. Impinging particles interact with the absorber material and produce secondary particles. In the scintillator layers the secondary particles produce light being read out with avalanche photodiodes or silicon photomultipliers.

Superconducting Solenoid

The superconducting solenoid is the heart of the CMS experiment and generates a homogeneous magnetic field of 3.8 T in the barrel region. The high magnetic field is required in order to have a high resolution of the particle momentum in the tracker part. The large size of the solenoid with a length of 12.5 m and a diameter of 6 m is needed since tracker and both calorimeters are placed within the coil. Outside of the magnet is the iron yoke for returning the magnetic field. The field strength inside the iron is 2 T [33].

Muon Detectors

Muon detectors are placed within slots in the iron yoke. Three different types of gaseous detectors are used [34]. Drift tubes are used in the barrel region where the magnetic field is homogeneous. The magnetic field in the end-cap is non-uniform and therefore cathode strip chambers are installed in the end-cap. Resistive plate chambers are complementary detectors in addition to the other two with excellent time resolution. Therefore, they are also used to trigger on events containing muons.

⁴A bunch of particles emitted in a small cone, created by the hadronization of a quark, is called jet.

These events are of interest due to the decay of the Higgs boson into two Z bosons that decay again into four leptons. The four muon decay produces clear signals with low background.

Beam Radiation, Instrumentation and Luminosity Project

A system being part of the CMS experiment, not displayed in Figure 16, is the beam radiation, instrumentation and luminosity project (BRIL) being responsible to measure luminosity and MIB. It consists of several sub-systems (see Chapter 3) and provides luminosity and background measurements to the CMS and LHC control room. Luminosity monitoring is needed to maximize the rate of interesting events and precise luminosity measurement to measure precisely the cross sections of the physics processes occurring during the collision. Background monitoring is essential to protect CMS and to ensure high quality data taking. In the case of adverse beam conditions it initiates a beam dump.

3 Beam Radiation, Instrumentation and Luminosity Project

The BRIL project consists of six different sub-systems for different purposes at locations inside and outside of CMS. An overview of the sub-systems is given in Table 3 and an illustration of the installation positions is shown in Figure 17.

Luminosity measurements are obtained by three systems, the Pixel Luminosity Telescope (PLT), the Hadron Forward (HF) Calorimeter and the Fast Beam Condition Monitor (BCM1F). All three systems are independent online luminometers for bunch-by-bunch luminosity measurements. An offline luminosity measurement is in addition done with the pixel tracker and allows a cross check and reduction of systematic errors. The three luminometers use different detector technologies. PLT is based on silicon pixel sensors as used in the pixel barrel [27]. It comprises four small angle telescopes around $z=1.8$ m away from the interaction point on each side. Each telescope has three equally spaced planes of pixel sensors [35]. The luminosity is obtained from the rate of the coincidences in the three planes. The full pixel readout gives a track reconstruction and is used to determine systematic corrections, efficiencies and a measurement of the collision point.

HF is $z=11.5$ m away from the CMS interaction point and uses photomultipliers that collect the light from quartz fibres. Cherenkov light is generated in the fibres when a relativistic charged particle passes through [36].

The third luminometer BCM1F is again close to the interaction point at $z=1.8$ m using single crystal diamond sensors. It is a particle counter and a detailed description of the BCM1F system is given in Chapter 3.1.

BCM1F provides in addition MIB rates measured inside CMS at low radii with a high sensitivity to beam gas interactions as well as to beam losses interacting with collimators (see Chapter 7.2). The Beam Condition Monitor “Leakage” (BCML) measures also MIB at small $z=1.8$ m and 14.4 m distance to the interaction point. It is based on poly-crystalline and a few single crystal diamond sensors. BCML integrates the signal current over different time periods (from 40 μ s till 83 s) and compares them to a threshold value. As soon as the integrated signals exceeds the threshold, a beam dump is initiated [37].

The Beam Halo Monitor (BHM) is installed outside of CMS at a radius of 20.6 m to be most sensitive to beam losses interacting with the collimators [38, 39]. It is based on quartz bars and UV-sensitive photomultipliers to measure Cherenkov light produced in the quartz bars by secondary shower particles from the collimators.

The last sub-system of the BRIL project is a so called Beam Pick-up Timing eXperiment (BPTX) being placed outside of CMS at a distance of $z=175$ m to the interaction point to measure the arrival time of incoming bunches. BPTX uses beam position monitors (BPM) that consist of electrodes installed symmetrically around the beam [40, 41]. A mirror current is induced into the beam pipe while the bunches are passing. It is travelling over the electrode surface and thus generating a signal.

System	Distance to IP	Distance to Beam Centre	Detector Type	Responsibilities
PLT	1.75 m	5 cm	silicon pixel sensors	luminosity measurement
HF	11.5 m	<1.8 m	quartz fibres and photomultiplier	luminosity measurement
BCM1F	1.8 m	6.9 cm	single crystal diamond sensors	luminosity and MIB measurements
BCML	1.8 m 14.4 m	4.5 cm 5 cm & 28 cm	single and polycrystalline diamond sensors	MIB measurement included in beam dumping system
BHM	20.6 m	1.8 m	quartz bars and photomultipliers	MIB measurement
BPTX	175 m	-	electrodes	Timing, Triggering and Gating

Table 3: Detectors within the BRIL project with their location, type of sensor and responsibility.

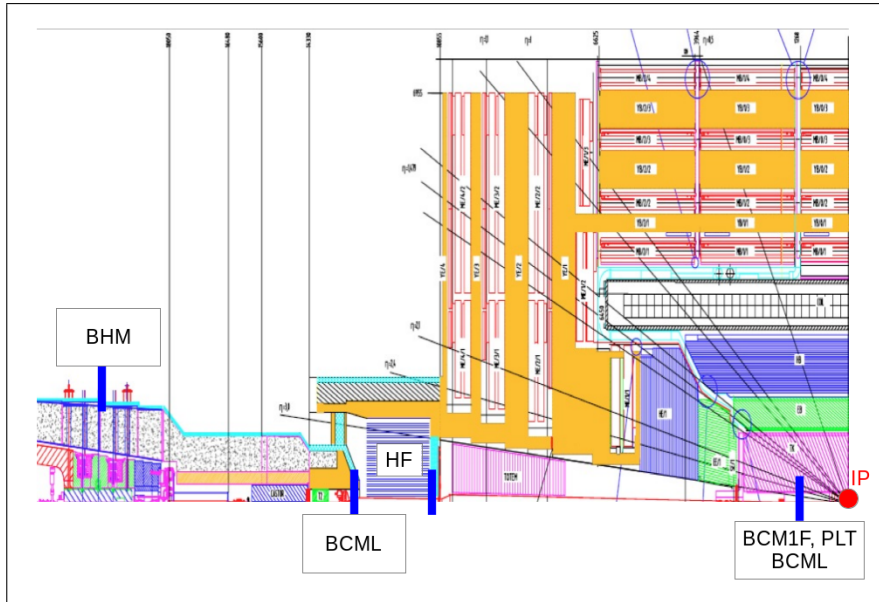


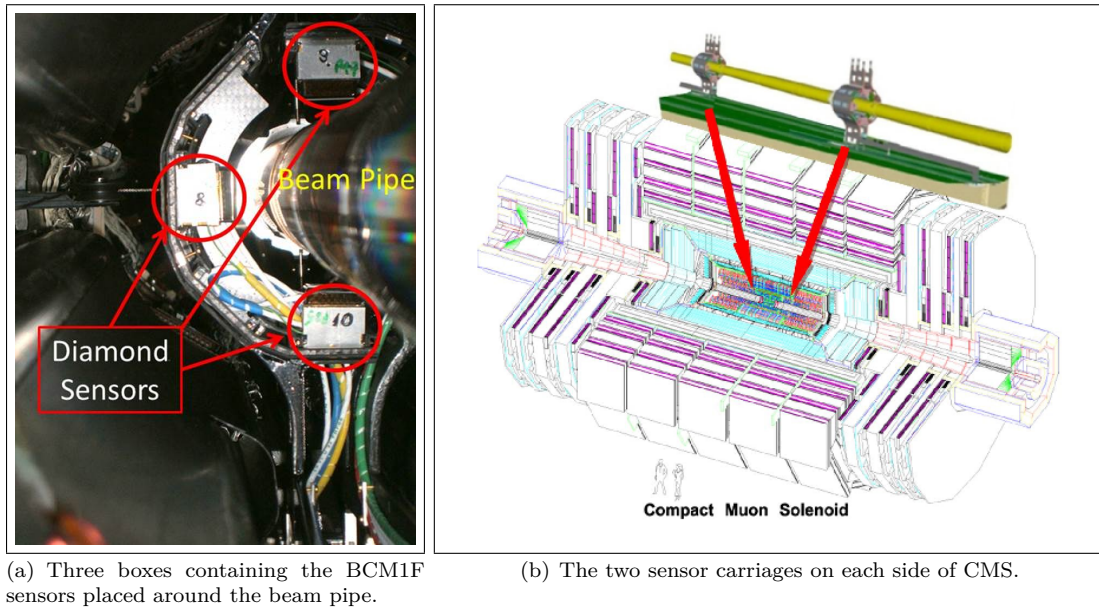
Figure 17: Quarter of CMS with the locations of the BRIL detectors.

3.1 The Fast Beam Condition Monitor BCM1F

BCM1F is a diamond based detector measuring bunch-by-bunch luminosity and MIB at the same time inside the CMS experiment. Diamond was the material of choice due to the low leakage current at room temperature and the lack of space for cooling at its location. It delivered valuable information to the LHC and CMS control room during Run 1 from 2010 to 2013. Due to its success as presented in Reference [42] an upgrade of BCM1F was planned during LS1. This chapter explains shortly the former BCM1F systems with its front-end components as used in Run 1. Additionally, a motivation of the BCM1F upgrade is given as well as an explanation of the upgraded parts. At the end a brief overview of the signal processing is shown.

Layout of BCM1F

The BCM1F system during Run 1 consists of four single crystal diamond sensors placed around the beam pipe on each side of the CMS interaction point [43]. The distance between interaction point and sensor position is 1.8m in Z-direction being optimized to distinguish MIB particles from incoming and outgoing bunches. The radius from the beam centre is 4.5cm. Each sensor has a size of $5 \times 5 \text{ mm}^2$ with an average thickness of $500 \mu\text{m}$. They are metallized with one pad (see Chapter 4.4.1). The sensors are placed within a shielding box together with the front-end electronics consisting of an amplifier and an optical hybrid. An illustration of the setup is given in Figure 18.



(a) Three boxes containing the BCM1F sensors placed around the beam pipe.

(b) The two sensor carriages on each side of CMS.

Figure 18: BCM1F setup inside the CMS experiment in Run 1.

Signal Readout

If a charged particle crosses the sensor it produces electron-holes pairs that are separated by an external electrical field. As soon as free charge carriers within the sensor start to move a signal on the metal electrode is generated. This signal is amplified by a radiation hard charge sensitive amplifier (ASIC) developed in $0.25 \mu\text{m}$ CMOS technology. It provides a peaking time of 22 ns and an equivalent noise charge (ENC) of around 700 electrons for an input capacitance of 5 pF [44]. The measured charge gain is 20 mV/fC [45].

The amplified signal is then coupled to a linear laser driver (LLD) array (AOH), also called optical hybrid, which converts a differential input voltage into a single ended output current added to a pre-set DC current allowing correct biasing of the laser diode above its threshold [46]. The optical signals of each sensor are then transmitted to the counting room by single mode fibres being merged together to a 12-fibre ribbon cable [47].

In the counting room the ribbon cable is connected directly to the optical receiver converting the optical signals back to electrical signals [48]. The complete front-end chain containing the amplifier and optical converter is illustrated in Figure 19.

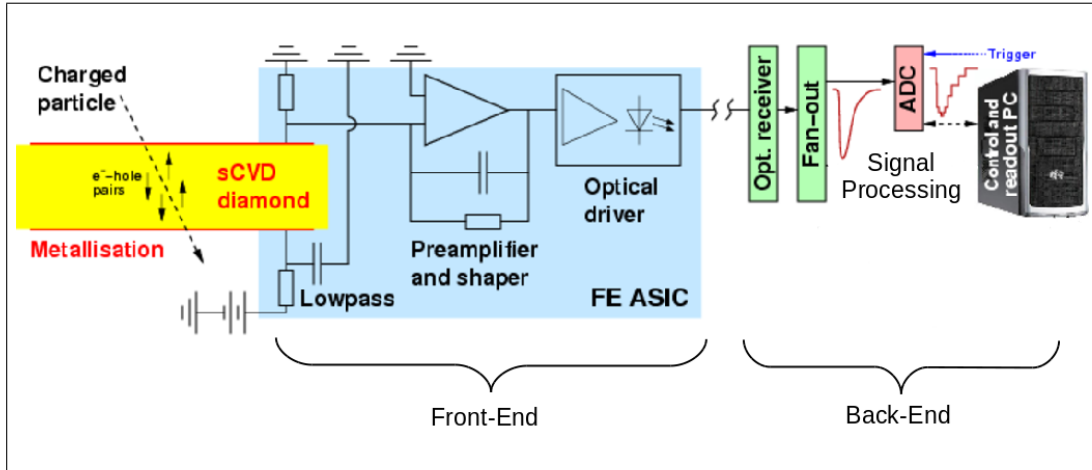
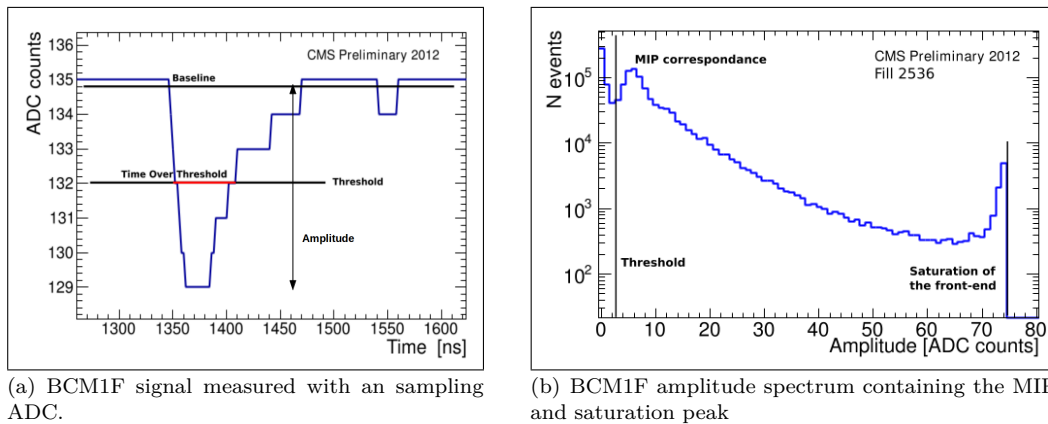


Figure 19: Readout scheme of BCM1F sensors containing the front-end electronics of amplifier and optical converter. The back-end modules are indicated by the optical receiver and the fan-in fan-out copying the sensor signal.

Signal Processing

The electrical signal is then processed by readout modules as an Analog-to-Digital Converter (ADC). In addition, other readout modules were used during Run 1 and results are for example shown in Reference [20]. ADC data is representatively shown in this thesis. A sampling ADC⁵ v1721 with 2 ns sampling rate is used for the signal sampling as shown in Figure 20(a) [49]. The baseline of the signals is defined by the electronics. In order to reject electronic noise a threshold is set. The signal amplitude is defined by subtraction of the baseline by the minimum signal height. A typical amplitude spectrum measured with the ADC without a threshold set is shown in Figure 20.



(a) BCM1F signal measured with an sampling ADC.

(b) BCM1F amplitude spectrum containing the MIP and saturation peak

Figure 20: BCM1F ADC Signal Processing

First, a pedestal peak at small ADC counts is visible due to electronic noise. This is cut by setting the previously mentioned threshold slightly above the pedestal value. Right after the threshold a peak at 8 ADC Counts is visible that corresponds to the energy deposition of relativistic particles,

⁵A sampling ADC uses a linear voltage ladder and compares the input signals successive to reference voltages.

hereafter denoted as MIP⁶. Most of the generated signals are originating from such charged particles (see Chapter 4.3). A saturation peak is visible at the end of the spectrum due to the limitation of the dynamic range of the front-end laser driver [46].

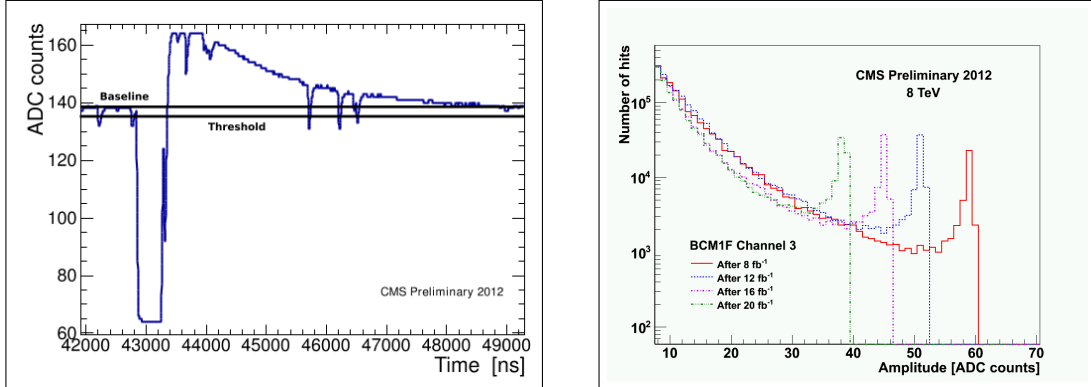
The positions of the MIP and saturation peak give information about the radiation damage of the sensor or front-end as explained in Reference [50].

3.2 Upgrade of BCM1F

In 2015, the LHC beam energy was increased from 4 TeV to 6.5 TeV and the bunch spacing reduced from 50 ns to 25 ns. However, the peaking time of the previously used amplifier is 22 ns being not sufficient to distinguish signals from two consecutive bunches with a spacing of 25 ns. Additionally, due to the dynamic range of the front-end ASIC, large signals as shown in Figure 21(a) saturate the front-end ASIC. On top an undershoot together with a baseline shift is observed. The recovery time of the baseline is about 6 μ s. Signals arriving within the undershoot are not counted and an increased inefficiency of the detector is caused [50].

The laser diode of the optical hybrid suffered as well from radiation damage leading to a reduction of the dynamic range being visible in a decrease of the saturation peak as a function of the integrated luminosity as shown in Figure 21(b). In addition, the sensors are as well damaged as illustrated in Reference [37]. This leads to additional decrease of the detector performance.

Therefore, an upgrade of the BCM1F systems was done during LS 1 including the sensors, front-end electronics and the complete BCM1F layout.



(a) Large signal appearing the BCM1F system and measured with the ADC. The signal is saturated and an undershoot is observed.

(b) The position of the saturation peak decreases with higher integrated luminosity.

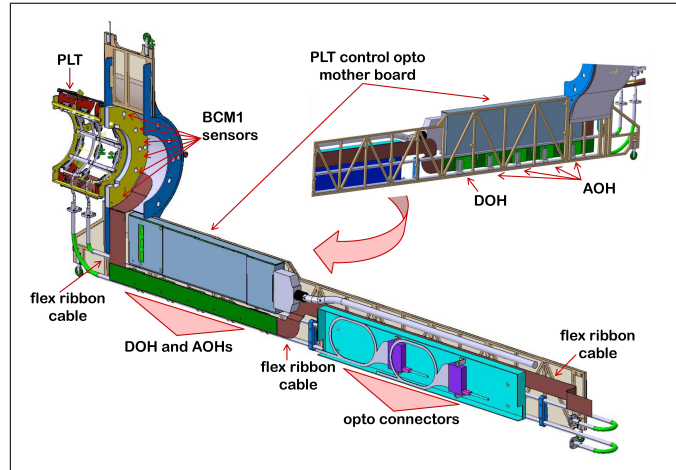
Figure 21: Limitations of the BCM1F front-end.

Holding Carriage

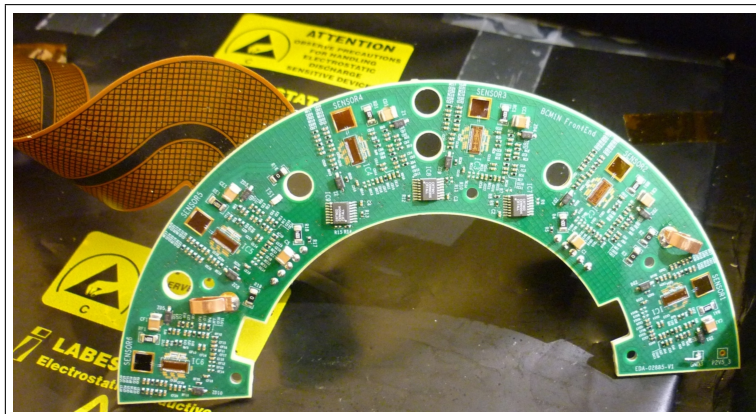
A new holding carriage as shown in Figure 22(a) is developed for placing the sensor and front-end ASIC close to the beam pipe but the optical hybrid with laser driver further away. The sensors are placed on a printed circuit board, the so called C-shape, together with the front-end ASIC. All in all 4 C-shapes are installed and each C-shape holds six diamond sensors. The total number of sensors is increased from 8 to 24 in order to increase the acceptance and robustness of the BCM1F

⁶MIP means strictly speaking minimum ionising particle. Relativistic particles deposit energy slightly above the minimum energy deposition predicted by the Bethe-Bloch formula at $\beta \cdot \gamma = 3.5$.

system. A 1.9m long flexible ribbon cable connects the C-shape with the optical hybrids that are of the same type as during Run 1. Due to the larger distance between beam centre and optical hybrid, the radiation damage is expected to be significantly reduced.



(a) Holding carriage for BCM1F, BCML and PLT including optical hybrids.



(b) C-shape assembled with the BCM1F sensors and the amplifier readout. The brown flexible ribbon cable connects the C-shape and optical hybrids (AOH).

Figure 22: BCM1F holding Carriage.

Diamond Sensors

The higher expected luminosity comes together with an increased particle flux. To reduce the count rate the metallization of the sensors has been subdivided in two pads as illustrated in Figure 23. The upgrade foresees an individual pad readout but with a common backplane for biasing both pads.

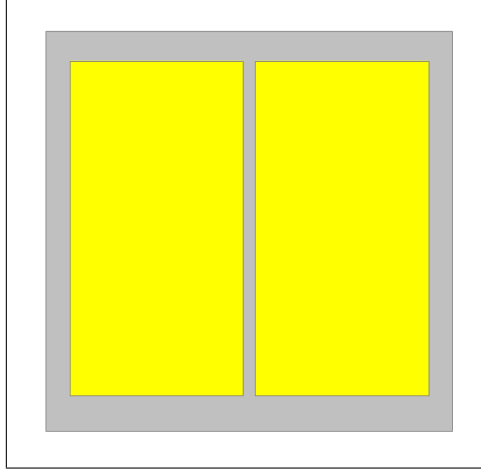
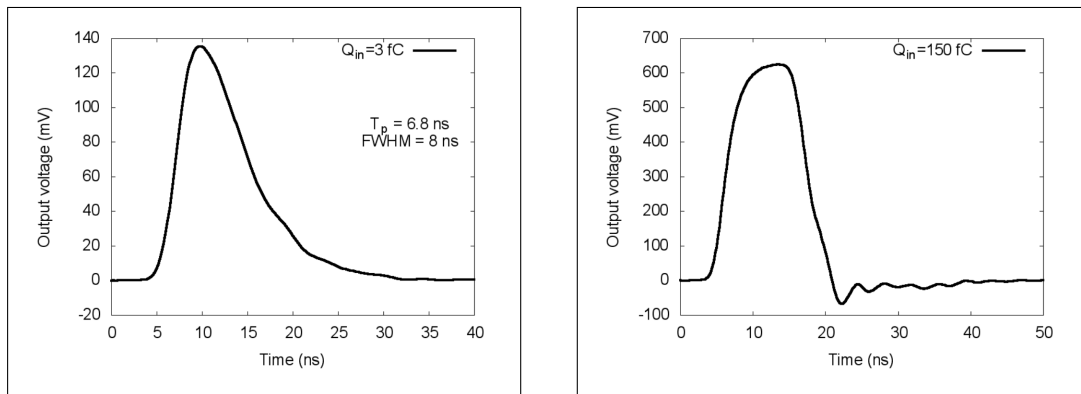


Figure 23: Metallization with two pads.

Amplifier

A dedicated front-end ASIC was developed at CERN in cooperation with the University of Science and Technology AGH Krakow on a commercial 130 nm CMOS technology [51]. It includes a trans-impedance pre-amplifier with an active feedback, a shaper stage and a fully differential output buffer [38]. A signal gain of 50 mV/fC is reached with a peaking time of around 7 ns and a full width at half maximum (FWHM) of less than 10 ns for a MIP particle of 3 fC as shown in Figure 24(a). The ENC is measured to be less than 400 electrons at a detector capacitance of 1 pF. A test of the signal response for a large signal of 150 fC (50 times larger than a MIP signal) does not show a long undershoot right after the signal as shown in Figure 24(b). The peaking time for such signals is in the order of 10 ns.



(a) Signal response of new front-end ASIC by feeding in a MIP like signal of 3 fC

(b) Signal response of new front-end ASIC by feeding in a large signal of 150 fC

Figure 24: Pulse shape of generated test signals to check the front-end ASIC performance [courtesy to D. Przyborowski].

3.3 BCM1F Signal Processing

Signals from all 24 diamond sensors corresponding to 48 channels are transmitted to the optical receiver as in Run 1 and then fed into the back-end modules, an ADC v1721, a Micro Telecom-

munications Computing Architecture (μ TCA) and a Real Time Histogramming Unit (RHU). Both ADC and μ TCA are sampling the signals allowing a detailed signal analysis but the ADC has a sampling time of 2 ns and the μ TCA of 0.8 ns. The ADC will be replaced by the μ TCA as soon as it is fully functioning. The RHU histograms the arrival time of incoming signals that allows to measure the machine induced background and luminosity (see Chapter 7).

Analog-to-Digital Converter

In order to monitor the BCM1F performance, ADC data is permanently taken and analysed. The signals are sampled with a 8 bit ADC v1721 operating at 500 MSamples/s. A sampled MIP signal of the upgraded BCM1F system is shown in Figure 25(a). The baseline is visible and the threshold for the certain channel is set to 5 ADC counts. However, the signal rise time is in contrast to the previous BCM1F system significantly reduced (scaling of the arrival time in Figure 20(a) is the same) resulting in a potentially higher time resolution. The corresponding amplitude spectrum in Figure 25(b) taken after an integrated luminosity of 0.2 fb^{-1} shows again a MIP peak. The dynamic range of the upgraded BCM1F is increased. Additionally, the position of the MIP peak is at a higher ADC value (11 ADC Counts) due to the increased signal amplification of the upgraded front-end ASIC. Even a two MIP peak resulting from simultaneous crossing of two particles is as well visible. The saturation peak is not sharp as for the previous BCM1F systems since the front-end ASIC has a non-linear behaviour for large pulses and the differential amplification is decreasing for high input voltages [51, 52].

A second amplitude spectrum is taken at an integrated luminosity of 2 fb^{-1} . The MIP peak position is shifted to lower values due to radiation damage in the diamond sensor causing traps that reduce the charge collection efficiency (see Chapter 4.3.2). A detailed ADC signal analysis can be found in Reference [53].

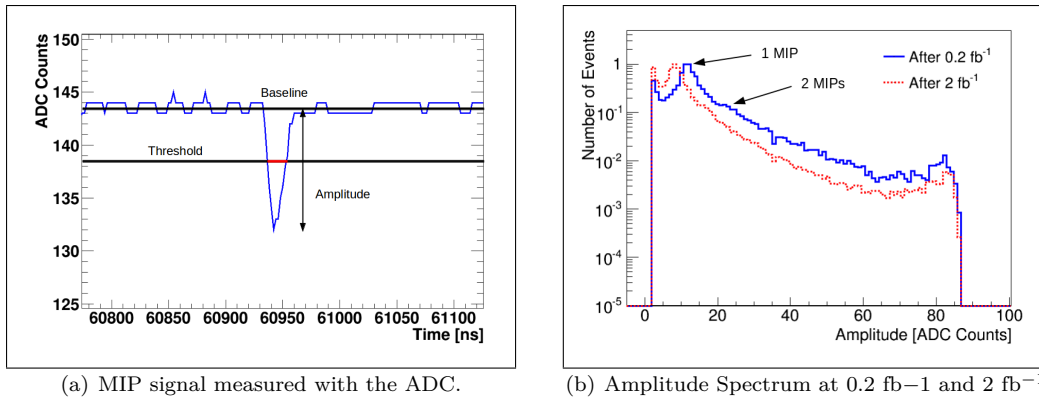


Figure 25: BCM1F signal processing with the ADC.

Outlook: Micro Telecommunications Computing Architecture

The Micro Telecommunications Computing Architecture (μ TCA) unit is an ADC based on FMC125 mezzanine boards [54, 55]. It samples the signals with 8 bits and a sampling rate of 1.25 GSamples/s corresponding to a sampling resolution of 0.8 ns. The 8 bit samples are transmitted to Advanced Mezzanine Card (AMC) carriers that host a peak finding algorithm to detect the arrival time and amplitude of the BCM1F sensor signals. The advantage of the μ TCA is the high time resolution

and a fast online peak-finding algorithm allowing also to resolve overlapped signals. Figure 26(a) shows a MIP signal sampled with the μ TCA. A FWHM of less than 10 ns is visible as specified by the upgraded front-end ASIC. The amplitude spectrum in Figure 26(b) is obtained by the peak finding algorithm⁷ and shows as well a MIP peak. Due to the low statistics, three bins are merged together in this measurement.

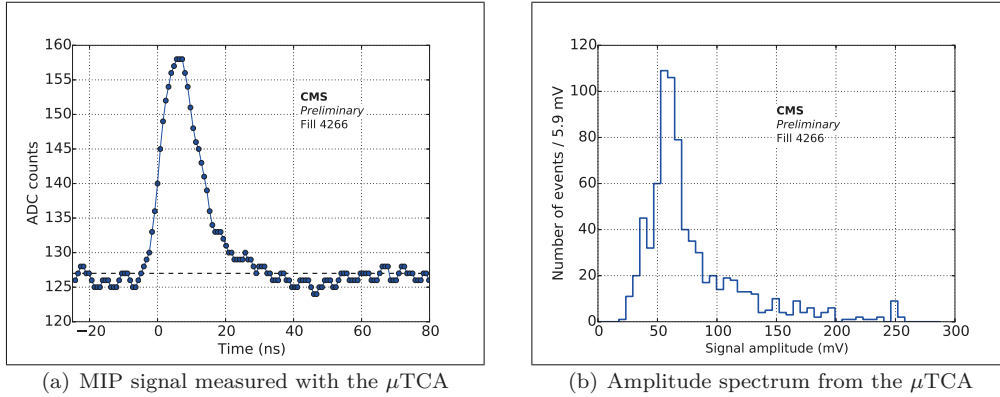


Figure 26: BCM1F signal processing with the μ TCA [courtesy to A. Zagodzinska]

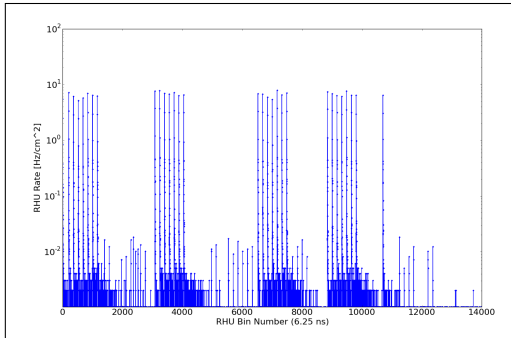
Real Time Histogramming Unit

The Real Time Histogramming Unit (RHU) consists of a 5 Mbit RAM Field Programmable Gate Array (FPGA), an on-board embedded Linux system and an ethernet readout. It was developed at DESY Zeuthen and records luminosity and MIB rates [56]. Before the signals are fed into the RHU, they pass a discriminator for rejecting signals being below a set threshold. The arrival time of all signals above the threshold are histogrammed in the RHU unit with a binning of 6.25 ns or 4 bins per bunch crossing (25 ns bunch spacing) over one LHC turn⁸ [57]. Histograms from each sensor channel are integrated over 4096 LHC turns (one lumi nibble). One lumi nibble is defined by $4096 \times 89 \mu s$. The RHU bins are read out via an ethernet connection and converted into a rate per cm^{-2} . The conversion is done by adding the RHU bin of all active channels from beam 1 or beam 2 and normalizing them by the diamond area of $5 \times 5 mm^{-2}$ and a lumi nibble.

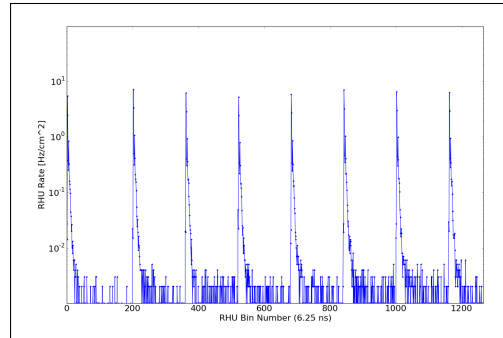
Since usually the number of collision products crossing the sensor is much higher than from MIB, the RHU rates are dominated by collisions as visible in Figure 27(a). A zoom into the RHU histograms makes the time pattern of the first bunch train visible as shown in Figure 27(b). The colliding bunches are spaced by 160 RHU Bins that corresponds to $1 \mu s$. Non colliding bunches, when only MIB particles are counted, show a much lower rate.

⁷A detailed description of the peak finding algorithm is given in Reference [52]

⁸One bunch needs $89 \mu s$ to perform one LHC turn.



(a) RHU rates showing the time pattern of bunch collisions in CMS



(b) Zoom to colliding bunches spaced by 160 RHU bins corresponding to $1 \mu s$.

Figure 27: BCM1F arrival time histogram taken with BCM1F. The units of the x-axis are RHU bins with a width of 6.25 ns.

4 Diamond Detectors

Diamond sensors become more and more attractive for the high energy particle detection as demonstrated in many publications and research studies [50, 58, 59]. In addition to luminosity measurements obtained by diamond sensors, they also provide crucial information to various beam loss sources as illustrated in Reference [20]. Diamond sensors are also used in CMS to protect the LHC in case of adverse beam condition triggering a beam dump [37].

This success is mainly based on the diamond material properties being reported in this chapter together with the explanation of the production of a diamond sensor. Detailed informations about the growth of the material and the metallization of the surface in order to use diamond as a sensor are as well given. In addition, the signal generation and the charge carrier mobility is explained being responsible for the electrical behaviour of the sensors. 58 sCVD sensors are electrically characterized to chose the best sensors for the BCM1F upgrade. This chapter gives an overview of each characterization measurement and summarizes its results.

4.1 Diamond Properties

The lattice structure of a diamond is shown in Figure 28. It is formed of carbon atoms having four bonds to each neighbouring atom. This results in a strong covalent tetrahedron forming a face-centred cubic lattice. The orbitals of the carbon atom form sp^3 hybridization to the neighbour atoms. The resulting material hardness is of minor interest for the sensor usage but an advantage by handling the sensor. Most important are the electrical properties making diamond based sensors applicable for high radiation environments.

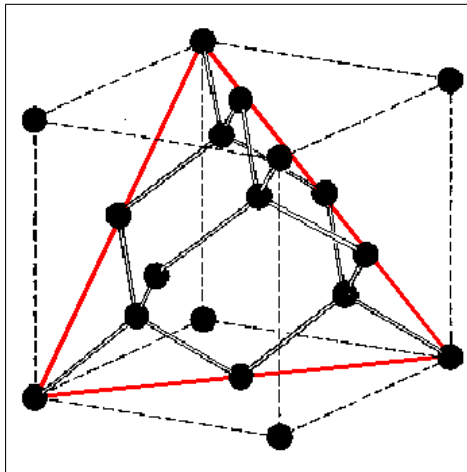


Figure 28: Illustration of diamond lattice (taken from <http://biointerface.org>)

Diamond is an insulator with a large band gap of 5.5 eV leading to a high ohmic resistivity of 10^{13} - 10^{16} Ω cm. This leads to a negligible leakage current of a sensor in the pA range even at room temperature. Therefore, a cooling of the sensor is not required allowing an installation in areas where no cooling is available due to a lack of space. The high charge carrier mobility of 1900 cm^2/Vs for electrons and 2300 cm^2/Vs for holes offers a very fast signal in the ns range allowing a fast timing response of the detector. A low sensor capacitance for the front-end electronics is as well given due to the low dielectric constant of diamond of 5.7. Moreover, the radiation hardness is of great

interest being defined by the displacement energy. The high displacement energy of 42 eV offers a high radiation hardness and a long life time even under high irradiation.

4.2 Diamond Production

Two different types of artificial diamond material are available, the high-pressure-high-temperature (HPHT) diamond and diamonds produced by chemical vapour deposition (CVD). HTHP diamond is not suitable for detectors due to a large number of impurities in the material. Diamonds produced by the CVD process have less impurities, a small defect density and are less cost-intensive. The understanding of the process parameters is, however, still in progress and the quality varies between each production batches [60].

4.2.1 Chemical Vapour Deposition

The CVD is based on a gas phase chemical reaction occurring above a substrate that leads to a deposition of C-atoms one-at-a-time with diamond configuration on the substrate. Commonly, a microwave plasma CVD reactor is used being illustrated in Figure 29 [61].

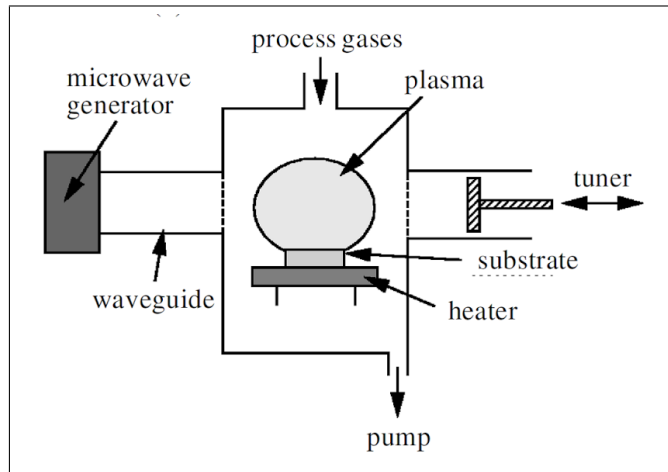
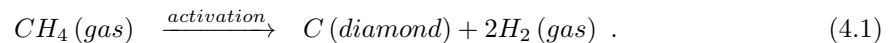


Figure 29: Illustration of microwave plasma reactor CVD used to grow diamond (taken from Reference [61]).

A gas mixture of CH_4 (concentration of 1%) and H_2 is pumped into the vacuum chamber with low pressure of 0.02-0.04 bar and being activated by the microwave power. This leads to heating and dissociation of gas molecules resulting in reactive radicals and atoms like H, H_2 , CH, CH_2 and CH_3 . A few thousand kelvins of the gas temperature are reached by this process. The plasma covered substrate is in addition heated up to temperatures higher than 700-900 °C in order to ensure diamond growth and suppress the formation of amorphous carbon. All reactive radicals and atoms undergo an adsorption and reaction with the surface and can also desorb back into the gas phase. In general, the CVD diamond growth is described by the simple reaction:



This however does not describe the complexity of diamond growth. Figure 30 shows in more detail

the schematics of the reaction process where CH_3 is stepwise added to the substrate surface being diamond in this case.

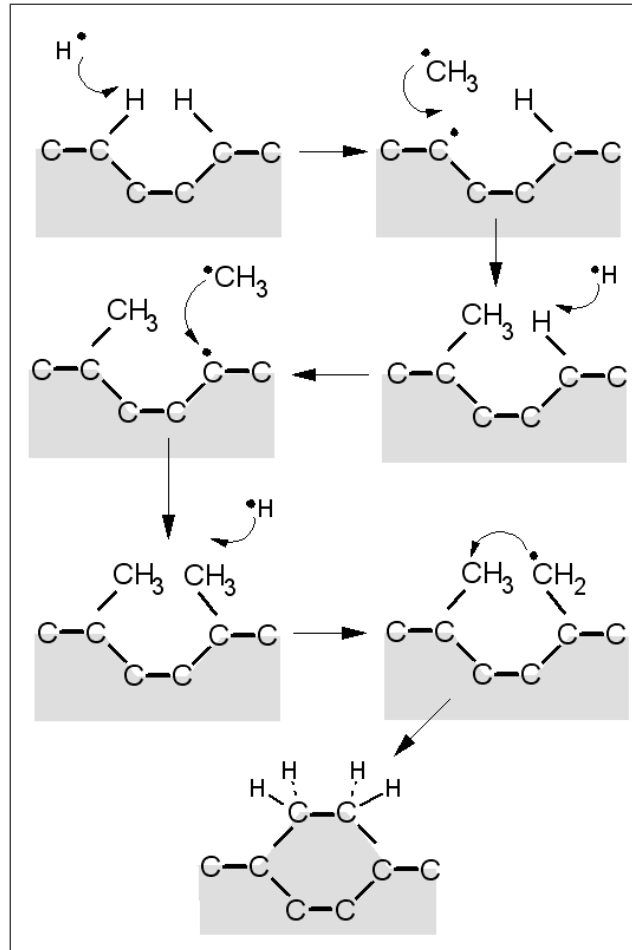
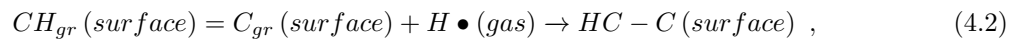


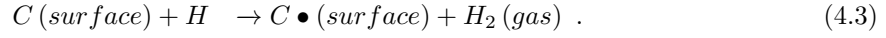
Figure 30: Illustration of diamond growth during the CVD process (taken from Reference [62]).

The whole bulk of the diamond substrate is sp^3 hybridized but so called “dangling bonds”⁹ remain at the surface. In order to avoid cross-linking of these atoms and a reconstruction to graphite, the surface is terminated with H keeping the diamond surface with sp^3 bonds stable. In addition, hydrogen etches graphitic sp^2 as well as sp^3 carbon but the reaction with sp^2 is much faster resulting in a removal of graphitic clusters back to the gas phase. A thermal decomposition of sp^2 surface carbons with hydrogen may happen with the following reaction:

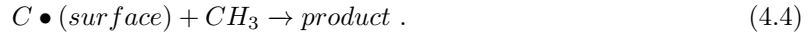


where C_{gr} denotes graphitic sp^2 carbons. Also the reverse reaction takes place depending on the process parameter. Hydrogen plays a key role in the CVD process not only by the prevention of graphitization but also by the diamond growth itself. The H atoms are detached from the surface by gaseous hydrogen atoms building a reactive surface atom:

⁹Danglings bonds are free radicals in an immobilized environment.



Due to the large number of radical H atoms, the surface atoms are quickly bonded to a H atom as soon as a free dangling bond appears. In addition, a second reaction can take place where a CH₃ molecules attaches to the dangling bond [63]:



A ring structure with diamond formation is created by abstraction of two H atoms if two nearby C atoms have CH₃ molecules attached.

Two types of diamonds are grown with the CVD process, single-crystal (sCVD) and polycrystalline (pCVD) diamond later denoted as sCVD or pCVD sensors. sCVD diamond is typically grown on a HPHT diamond substrate having single-crystal structure. The growth rate of such high quality diamond is low being 1 μm per hour and only small pieces in the order of 5×5 mm² are grown to ensure one crystal orientation for the whole diamond [64]. In contrast, most of the pCVD diamonds are grown on single crystal Si wafers due to good availability and low costs. This is only possible since Si has a similar lattice structure and an expansion coefficient similar to diamond [61]. pCVD diamond is grown 10 times faster with large wafer size being laser cut to the desired size. However, the seed side of the pCVD diamond contains grain boundaries. Several of them are stopped during the growth process by the neighbouring grain. The number of grains therefore decreases with an increasing diamond thickness but they never disappear completely as illustrated in Figure 31.

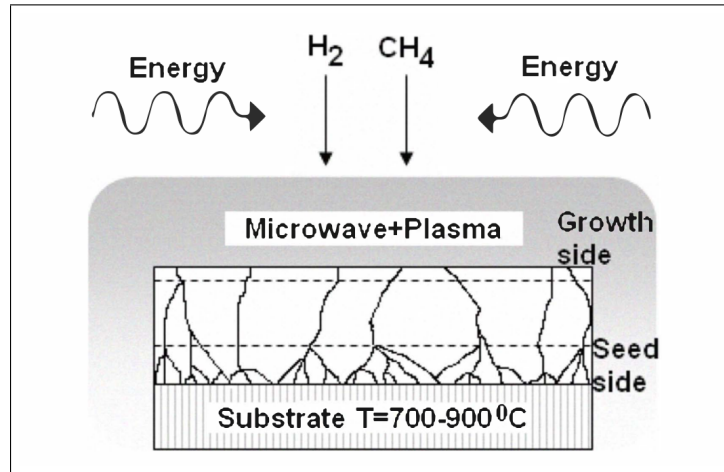


Figure 31: Illustration of pCVD diamond grains grown during the CVD process (taken from Reference [64]).

The crystal orientation of each grain is completely random. An improvement of the homogeneity is reached by removing a certain thickness of the material at the seed side. A polishing enhances the roughness for the surface of the pCVD as well as for the sCVD diamond. Typically, a thickness of sCVD and pCVD diamond of 300-500 μm is obtained after the polishing.

The advantage of sCVD sensors is a very good resolution of the deposited energy by ionization

and a full charge collection efficiency. However, only small sizes are available. Sensors made of pCVD are in contrast less cost intense and large sizes are available. However, pCVD sensors have a reduced charge collection efficiency being in addition non-homogeneous over the sensor bulk [65]. This thesis comprises only measurements done with sCVD sensors since BCM1F is equipped with sCVD to achieve full charge collection efficiency for the signal generation.

4.2.2 Metallization of Diamond Sensors

In order to use sCVD as a sensor, an electrode on each side of the diamond surface is needed. Two types of metallization are done. One is done at the GSI Helmholtz Centre for Heavy Ion Research with a 50 nm thick layer of chromium and then a 150 nm thick gold layer (Cr/Au). The other one is done at the Princeton University with an alloy of tungsten (90% of weight or 50% of atoms) titanium (10% of weight or 50% of atoms) (W/Ti). Usually, photolithography is used to make the metallization where first the metal is sputtered on the diamond surface and then a photoresist is coated on top. A metallization mask is then created by exposing the photoresist with laser light followed by an etching process building the metallization pattern. At the end the photoresist is removed. More details of the metallization process with photolithography is given in Reference [66,67].

Both metallization types were done to produce the one and two pads metallization. Pictures of these metallization types and pattern are given in Figures 42, 78 and 79.

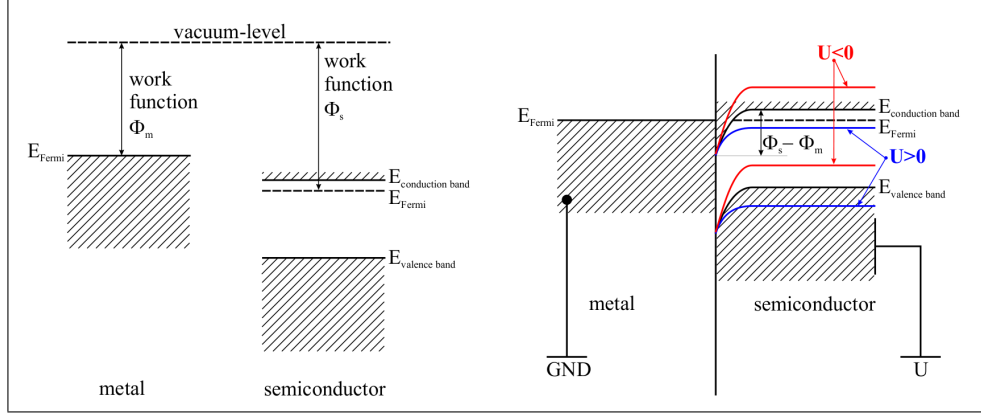
The interface of the metal and the diamond material is of interest for the electrical behaviour. Two possible interface contacts are possible, ohmic and Schottky contact. In order to distinguish between an ohmic and Schottky contact, the work function Φ of the metal and semiconductors are compared. The work function is defined by the energy needed to bring an electron from the Fermi level¹⁰ out of the bulk to infinite distance, the vacuum level.

Ohmic contacts are recommended for radiation detection since the current flows in both direction through the contact [68]. It is created if the work function Φ_m of the metal is smaller than the one of the semiconductor Φ_s . The Fermi levels are adapted to each other by electron migrating from the metal to the semiconductor as shown in Figure 32(a). The band edges are bent downwards and no potential barrier is created allowing the electrons to traverse from both directions (positive and negative bias voltage).

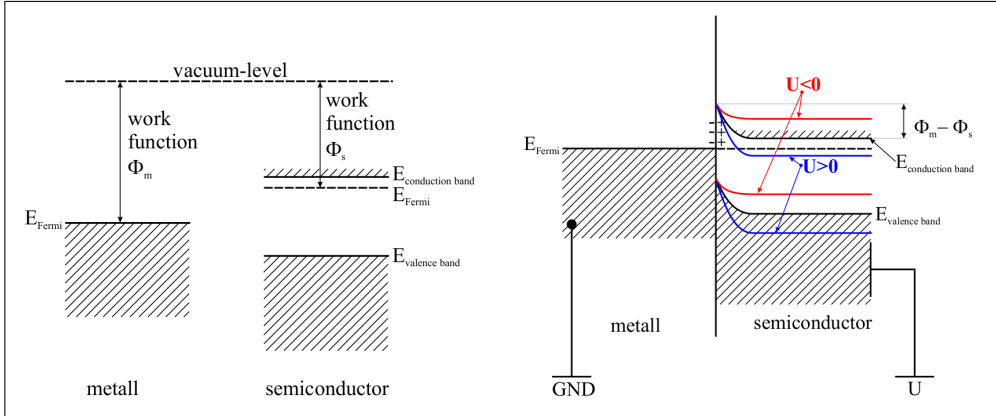
However, due to the large band gap of diamond, a real ohmic contact is difficult to reach and a Schottky behaviour is often observed [69]. A Schottky contact is created if a metal and a n-type semiconductor or insulator with $\Phi_s < \Phi_m$ are connected. Electrons from the semiconductor migrate to the metal leaving positive charge at the surface adjusting the Fermi levels. The band edge of the semiconductor is pulled down in the bulk and a barrier height of $\Phi_m - \Phi_s$ is created as shown in Figure 32(b). If a negative bias voltage is applied the barrier height is reduced and electrons can cross the metal-semiconductor interface leading to a current flow. In the case of a positive bias voltage the barrier height increases and only a small current can flow due to tunnelling. A Schottky contact is therefore rectifying.

¹⁰The difference of a metal and a semiconductor is the Fermi level being within the conduction band for the metal and located in the band gap for the semiconductor.

This Schottky behaviour is therefore important since carbide forming metals create electrically active defects that lower the barrier height and lead to an increased leakage current [69]. It is known that Titanium may create such a carbide being used by the Princeton metallization.



(a) Ohmic contact before (left) and after (right) connecting the metal with semiconductor/insulator



(b) Schottky contact before (left) and after (right) connecting the metal with semiconductor/insulator

Figure 32: Band structure for ohmic and Schottky contact (taken from Reference [68]).

4.3 Signal Generation in Diamond

Charge carriers in a diamond sensor are generated as soon as a charged particle crosses the sensor and is losing its energy being explained by two dominant mechanisms, bremsstrahlung and ionization/excitation [70]:

$$\frac{dE}{dx} = \frac{dE}{dx} \Big|_{brems} + \frac{dE}{dx} \Big|_{ion}. \quad (4.5)$$

Ionization takes place if an impinging charged particle knocks along its path electrons out of the material atoms. This energy loss process is explained by the so called Bethe-Bloch formula [71].

$$-\frac{dE}{dx} \Big|_{ion} = K z^2 \frac{Z}{A} \frac{1}{\beta^2} \left[\frac{1}{2} \ln \left(\frac{2m_e c^2 \beta^2 \gamma^2 T_{max}}{I^2} \right) - \beta^2 - \frac{\delta(\beta\gamma)}{2} \right], \quad (4.6)$$

where

$$\begin{aligned}
 K &= 4\pi N_A r_e^2 m_e c^2 \\
 \beta &= \frac{v}{c} \\
 \gamma &= \frac{1}{\sqrt{1-\beta^2}} \\
 T_{max} &= \frac{2m_e c^2 \beta^2 \gamma^2}{1 + 2\gamma \frac{m_e}{m_0} + \left(\frac{m_e}{m_0}\right)^2} .
 \end{aligned}$$

All variables of the Bethe Bloch formula are defined in Table 4 and Figure 33 shows the energy loss of charged particles for different materials. Charged particles having an energy where the energy loss has its minimum are called minimum ionizing particles (MIPs) being used as a reference.

Variable	Definition
z	charge of incoming particle
Z	atomic number of material
A	atomic weight of material
m_e	rest mass of electron
m_0	rest mass of incoming particle
c	speed of light
T_{max}	maximum energy transfer
I	excitation potential of atoms in the material
N_A	Avogadros number
r_e	classical electron radius
δ	density correction
α	fine structure constant

Table 4: Variables for Bethe Bloch formula.

The ionization process is only relevant for impinging electrons having a kinetic energy in the order of 10^6 eV. For energies above 10^8 eV Bremsstrahlung becomes more important. The energy loss of electrons for bremsstrahlung is given by:

$$\left. \frac{dE}{dx} \right|_{brems} = \frac{E}{X_0} \tag{4.7}$$

$$= 4\alpha N_a \frac{Z^2}{A} r_e^2 E \ln \frac{183}{Z^{1/3}} , \tag{4.8}$$

where E is the energy of the electron and X_0 the radiation length being the mean distance where the electron loses $1/e$ of its energy. All other variables are given in Table 4. The radiation length is proportional A and $1/Z^2$ of the material.

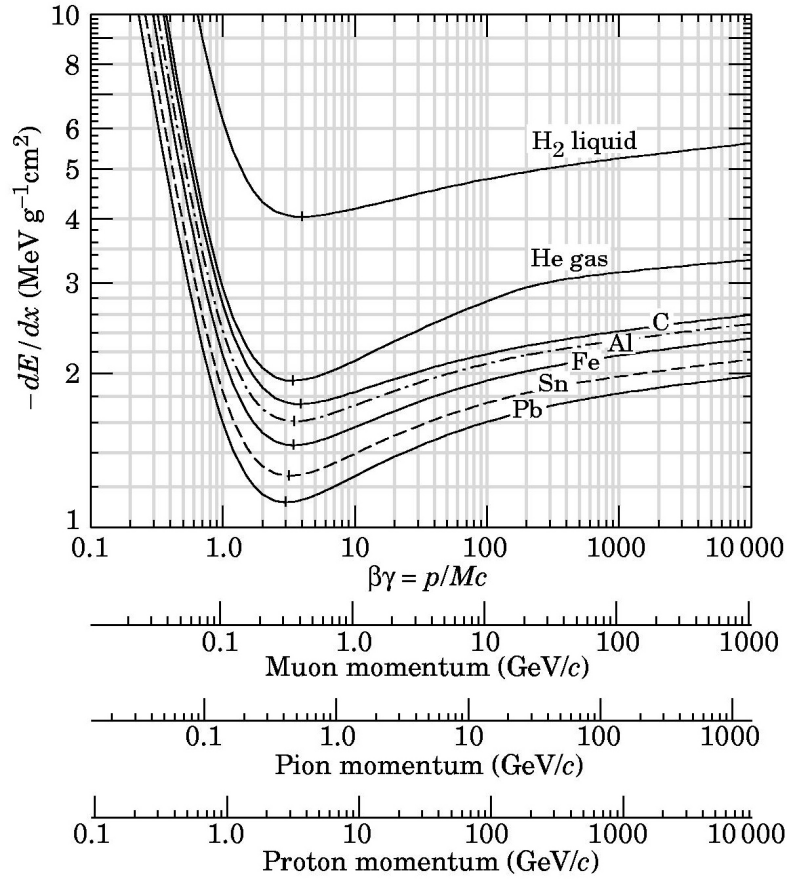


Figure 33: Energy loss of muons, pions and protons for hydrogen, gaseous helium, carbon, aluminium, iron, tin and lead.

Figure 34 shows as an example the energy loss of electrons including bremsstrahlung and ionization in diamond with a density ρ of 3.52 g/cm^3 . At lower energies the energy loss is due to ionization/excitation. At higher electron energies Bremsstrahlung becomes more important. The minimum energy loss equivalent to a MIP is at $E = 1.58 \text{ MeV}$. It has to be pointed out that relativistic particles have an energy loss being slightly higher than the energy loss for the MIP energy. However, the deposited energy in the sensor material depends on the thickness of the sensor and is normally smaller than the lost energy. So called δ -electrons generated by an impinging particle can leave the material without depositing its complete energy in the material block. If the sensor is sufficiently thick the δ -electrons deposit their energies in the material. The energy loss per collision is a statistical process and a fluctuation around the mean value appears. The distribution of the energy loss is described by the straggling function [72].

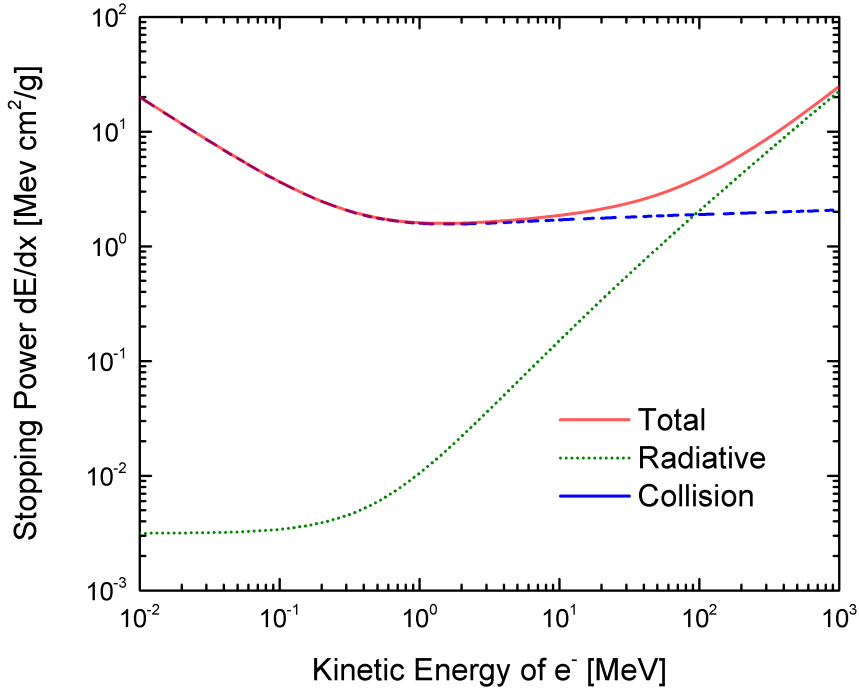


Figure 34: Energy loss of electrons in diamond with a supposed density of 3.53 g/cm^3 . The data is taken from the ESTAR database on www.nist.gov.

A Gaussian distribution is expected for very thick sensors since the deposited energy and lost energy are almost the same. More δ -electrons can leave the material if the sensor is thin and the probability of a large deposited energy need to take into account. Therefore, a tail towards high deposited energies appears in the distribution usually described by a Landau distribution [73, 74]. In practice, the energy loss distribution is well described by a Landau-Gauss convolution where the Gaussian represents the electronic noise of the system fluctuating around the mean value of the energy deposition [71, 75]. The Landau distribution is shown in Figure 35 with the following approximation:

$$L(\lambda) = \frac{1}{2\pi} \cdot \exp\left[-\frac{1}{2}(\lambda + e^{-\lambda})\right], \quad (4.9)$$

where λ is the deviation of the actual energy loss ΔE from the most probable energy loss ΔE^W of a particle crossing a sensor of the thickness x and is defined as:

$$\lambda = \frac{\Delta E - \Delta E^W}{\xi}, \quad (4.10)$$

with

$$\xi = Kz^2 \frac{Z}{A} \frac{1}{\beta^2}. \quad (4.11)$$

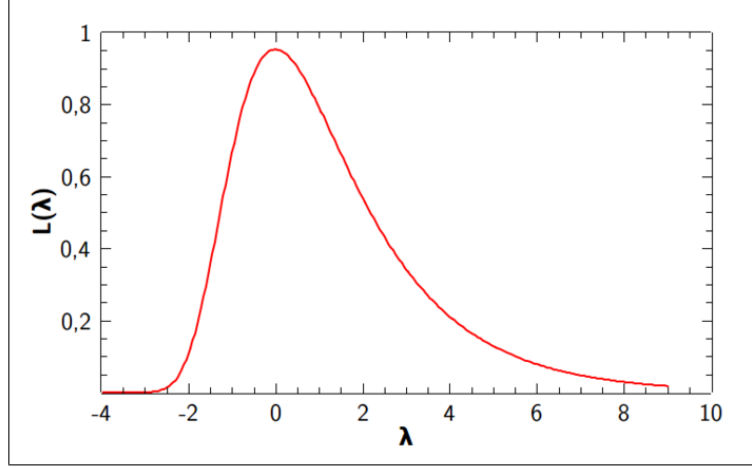


Figure 35: Landau distribution as a function of the deviation from the most probable energy loss λ centred around 0.

The used variables for ξ are already defined in Table 4.

The number of generated electron-hole pairs $N_{e/h}$ is now estimated by using the energy loss of electrons with MIP energy $\left. \frac{dE}{dx} \right|_{MIP}$ of 1.58 MeV:

$$N_{e/h} = \frac{\rho}{\varepsilon_{e/h}} \cdot \left. \frac{dE}{dx} \right|_{MIP}, \quad (4.12)$$

where ρ is the mass density. The energy needed to create an electron-hole pair is given by $\varepsilon_{e/h}$ and depends strongly on the sensor quality. In the literature the obtained $\varepsilon_{e/h}$ differs from 17 eV [76] to 12.84 eV [77]. The value of 17 eV, with a relative uncertainty of 16%, is slightly larger in comparison to other measurements but consistent with the presented results here. A number of electron-hole pairs of 36 e/h per μm is generally used [78].

If a charged particle like an electron crosses the sensor it creates electron-hole pairs that are separated due to an applied electrical field. The charge collection efficiency (CCE) is defined by using the charge measured as a signal on the electrode when a particle crosses the sensor that is influenced by the charge carrier drift and the charge carriers are expected to be induced due to ionization:

$$CCE = \frac{Q_{coll}}{Q_{ind}} \quad (4.13)$$

$$= \frac{Q_{coll}}{36 \frac{e/h}{\mu\text{m}} \cdot d}, \quad (4.14)$$

where Q_{coll} is the collected charge and Q_{ind} the induced charge. The induced charge is as previously

mentioned given by the generated number of electron-hole pairs per μm and the sensor thickness d . The so called charge collection distance (CCD) is also often used and given by

$$CCD = CCE \cdot d. \quad (4.15)$$

It represents the averaged drift length of the charge carriers and cannot be higher than the sensor thickness itself.

4.3.1 Charge Carrier Drift

A sensor current is instantaneously induced on a readout electrode when a previously created charge carrier starts to move under the influence of an electrical field applied between two electrodes. One electrode is biased and on the other one the signal current is read out. Integrating this signal current allows to measure a charge collection. This is quantitative described by Ramo's theorem and its introduction to a so-called Weighting Potential even for sensors having any number of readout electrodes as for the two pad sCVD sensors [79].

The following description of the charge carrier drift and its induced current is based on Reference [80].

Now assuming a mobile charge q in between any number of grounded electrodes. q creates a small equipotential sphere with the potential V_q . V is then the potential of the electrostatic field between the conductors with $V = 0$ at the conductors itself and it follows that $\nabla^2 V = 0$. Applying Gaussian law yields to:

$$\int_{\substack{\text{sphere's} \\ \text{surface}}} \frac{\partial V}{\partial n} ds = 4\pi q. \quad (4.16)$$

Then the charge is removed and one conductor A is raised to unit potential V_1 again with $\nabla^2 V_1 = 0$. The potential where the charge was, is now V_{q1} and with Greens Theorem follows:

$$\int_{\substack{\text{volume} \\ \text{between} \\ \text{boundaries}}} (V_1 \nabla^2 V - V \nabla^2 V_1) dv = - \int_{\substack{\text{boundary} \\ \text{surfaces}}} \left(V_1 \frac{\partial V}{\partial n} - V \frac{\partial V_1}{\partial n} \right). \quad (4.17)$$

The left integral is 0 due to the previously set conditions. The right part of Equation (4.17) is then split in three integrals over the surface of all conductors except A , the surface of A and the surface of the sphere. Applying that A has a unit potential and all others are set to 0, Equation (4.17) becomes:

$$0 = - \int_{\text{surface } A} \frac{\partial V}{\partial n} ds - V_{q1} \int_{\substack{\text{sphere} \\ \text{surface}}} \frac{\partial V}{\partial n} ds + \underbrace{V_q \int_{\substack{\text{sphere} \\ \text{surface}}} \frac{\partial V_1}{\partial n} ds}_{=0, \text{ since the charge is removed}} \quad (4.18)$$

$$= 4\pi Q_A - 4\pi q V_{q1}, \quad (4.19)$$

where Q_A is the charge on the readout electrode A with $Q_A = qV_{q1}$.

Taking now a charge q that moves along y (from the bottom to the top between the electrodes), an instantaneous current on the electrode A is induced:

$$\begin{aligned} i_A &= \frac{dQ_A}{dt} \\ &= q \frac{dV_{q1}}{dt} \\ &= q \left(\frac{\partial V_{q1}}{\partial y} \frac{dy}{dt} \right). \end{aligned} \quad (4.20)$$

Including the charge velocity $v_y = dy/dt$ leading to

$$\begin{aligned} i_A &= qv_y \frac{\partial V_{q1}}{\partial y} \\ &\equiv qv_y \frac{\partial \Phi}{\partial y}, \end{aligned} \quad (4.21)$$

where Φ is the weighting potential that describes the coupling of a charge at any position to the readout electrode A . Formula (4.21) can be expressed as a weighting field as well by:

$$i_A = -q \vec{v} \cdot \vec{E}_Q. \quad (4.22)$$

If a charge travels on any path s from position 1 to position 2 then the induced charged on the readout electrode A is determined by the weighting potential with

$$\begin{aligned} \Delta Q_A &= q (V_{q1}(2) - V_{q1}(1)) \\ &\equiv q (\Phi_A(2) - \Phi_k(1)). \end{aligned} \quad (4.23)$$

Summarizing, weighting potential and weighting field are obtained by setting a readout electrode to unit potential and all other electrodes to zero potential and a net induced charge on the readout electrode is estimated by Equation (4.23). Note that the weighting field is not the same as the electrical field since the weighting field depends only on the sensor geometry and determines how a charge couples to a certain readout electrode. In contrast the electrical field determines the trajectory and velocity of a charge carrier. Only in the case of a two electrode configuration the electrical field and weighting field are the same.

The induced charge on a readout electrode depends only on the weighting potential and can be understood as in the following example.

Consider an electron-hole pair q_n and q_p created under a readout electrode at a position y_0 inside the diamond sensor bulk. Both charge carriers travel perpendicular to the electrodes whereas q_n moves to the n-electrode at the position y_n and q_p to the p-electrode at the position y_p . The induced charge on the readout electrode k is determined by Equation (4.23):

$$Q_k = q_p [\Phi_{Q_k}(y_p) - \Phi_{Q_k}(y_0)] + q_n [\Phi_{Q_k}(y_n) - \Phi_{Q_k}(y_0)] , \quad (4.24)$$

with the hole charge of $q_p = e$ and the electron charge of $q_n = -e$ that leads to

$$Q_k = e [\Phi_{Q_k}(y_p) - \Phi_{Q_k}(y_0)] - e [\Phi_{Q_k}(y_n) - \Phi_{Q_k}(y_0)] , \quad (4.25)$$

If the signal is now only measured on the p-electrode then the induced charge is simplified to

$$Q_k = e [\Phi_{Q_k}(y_p) - \Phi_{Q_k}(y_0)] . \quad (4.26)$$

The condition used for weighting potential leads to $\Phi_{Q_k}(y_p) = 1$ and $\Phi_{Q_k}(y_n) = 0$ resulting in $Q_k = e$. The weighting potential at the p- and n-electrode of the neighbouring pad is zero $\Phi_{Q_{k+1}}(y_p) = 0$ and $\Phi_{Q_{k+1}}(y_n) = 0$ resulting in $Q_{k+1} = 0$. It follows that the induced charge on the readout pad is zero if a charge carrier does not terminate under the readout pad. The reason is the instantaneous currents that depends on the weighting field as given in Equation 4.21.

4.3.2 Signal Generation in the Presence of Defects

The induced charge on an electrode as explained in the end of the previous subsection applies only if the charge carrier is generated at one electrode, travels all the way through the sensor and terminates at the other electrode. However, in the case the charge carrier is trapped on its way, the lifetime and the resulting induced charge on the readout electrode need to be take into account. Such traps are caused by lattice defects being described in detail by Reference [81]. The most important defects are:

- a carbon vacancy
- self-interstitial
- foreign substitutional atom
- foreign interstitial atom

being illustrated in Figure 36. Depending on the type of defect, additional energy levels E_t with a corresponding cross section are created. If the energy level is inside the band gap, a trapping may happen. The Fermi distribution determines for each trap level at a specific temperature T the occupation state given for a material having a Fermi level of E_f

$$F(E_t) = \frac{1}{1 + e^{\frac{E_t - E_f}{kT}}} , \quad (4.27)$$

where k is the Boltzmann constant. All trap levels with $E_t - E_f$ of a few eV at room temperature are not occupied since $kT \ll E_t - E_f$.

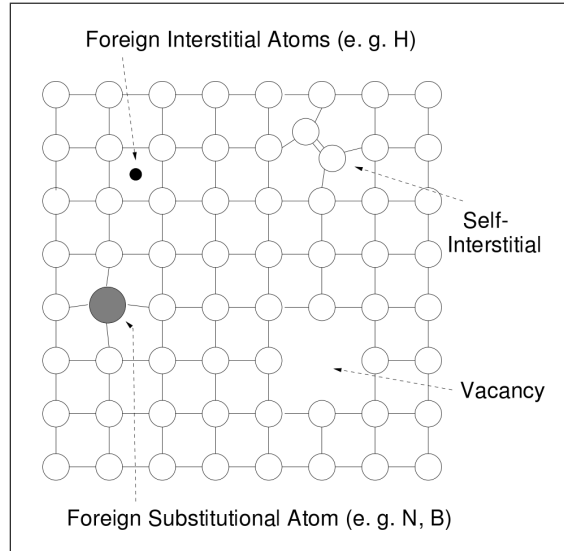


Figure 36: Illustration of point defects in diamond (taken from Reference [81]).

However, such traps can be filled with charge carriers generated by ionization. In general, the defects act in three different ways depending on the energy level they are located, (a) trapping, (b) recombination and (c) generation of charge carriers.

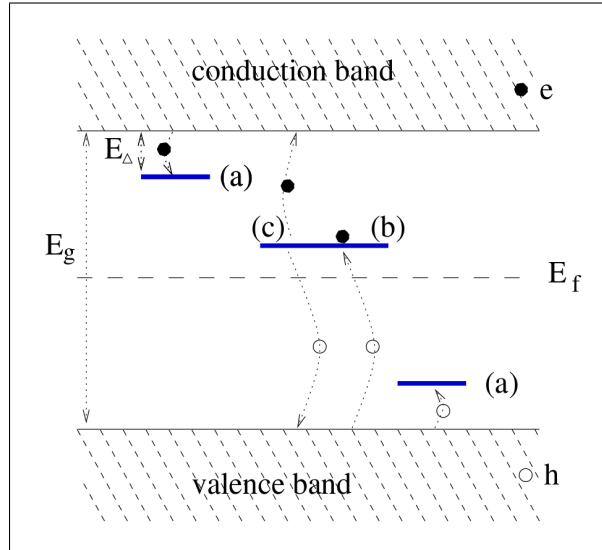


Figure 37: Illustration of defect mechanism leading to (a) trapping, (b) recombination and (c) generation of charge carriers (taken from Reference [82]).

Traps capture free charge carrier from the valence or conduction band and the trapping rate r_t per unit volume is defined by the trap density not being occupied n_t , the density of free charge carriers n_c , the cross section of the trap σ_t and the thermal velocity of charge carriers v_{th} :

$$r_t = n_t n_c \sigma_t v_{th} . \tag{4.28}$$

The trapped charge can now either recombine with a charge carrier of opposite sign or is thermally emitted again. The recombination rate r_r per unit volume is

$$r_r = n_r n_c \sigma_r v_{th} , \quad (4.29)$$

where n_r is the density of occupied traps and σ_r the cross section of capturing a charge carrier of opposite sign. In the case of thermally emission, the emission rate r_e depends on the energy the trap level is located E_Δ and is defined by

$$r_e = s n_r e^{-\frac{E_\Delta}{kT}} , \quad (4.30)$$

with s being the escape factor typically in the order of 10^{12} - 10^{14} s^{-1} . It may happen that the trapped electron is excited to the conduction band and the empty trap is filled again with an electron from the valence band creating a free electron-hole pair. This creates an erratic dark current. However, erratic currents are not fully understood yet since they appear above a certain electrical field strength and after a certain time being different from sensor to sensor.

For the analysis done in this thesis, the trapping process plays a key role. Depending on the trap level, the emission rate is low for deep traps or high for shallow traps. Typically, deep traps having a release time of hours or even days and shallow traps of seconds [83]. Long time trapped charge does not contribute to the signal, since the charge induced to the readout electrode becomes less. In addition, trapped charge causes so called polarization. If an ionizing particle crosses a sensor with an external applied field, it creates electron-hole pairs travelling to the corresponding electrode. This leads to a high density of electrons near the positive electrode and a high density near holes at the negative electrode. However, the trapping process is proportional to the charge carrier density and therefore most of the charge carriers are trapped close to one of the electrode causing an electrical field counteracting to the external field. The sensor is therefore polarized. Since the applied high voltage is set to a given value, the integral over the electrical field is constant during this process. This is only realized by compensating the reduced field strength in the centre of the sensor bulk by increasing the electrical field strength at the electrodes. In the case of sufficiently high polarization, the electrical field strength in the centre of the sensor is low and recombination appears that leads to a reduced CCE as well as a reduction of the effective drift length of a charge carrier.

The trapping and recombination reduces the life-time τ of the charge carriers being defined by

$$\tau = \frac{n_c}{r_t + r_r} \quad (4.31)$$

$$= \frac{1}{v_{th} (\sigma_t n_t + \sigma_r n_r)} . \quad (4.32)$$

This life-time is then used to calculate the charge induced on the readout electrode Q_k . First of all, the initial amount of charge Q_0 is reduced by trapping and is written as a function of time

$$Q(t) = e^{-t/\tau} . \quad (4.33)$$

Using the charge drift velocity of $v = \mu E$, where μ is the drift mobility and E the effective electrical field, the time of travelling a distance of x can be estimated with

$$t = \frac{x}{v} \quad (4.34)$$

$$= \frac{x}{\mu E} . \quad (4.35)$$

The remaining charge is then

$$Q(x) = Q_0 e^{-x/L} , \quad (4.36)$$

with $L = \mu E \tau$ being the average drift length. The total induced charge on the electrode Q_k of a sensor with the thickness d is expressed by:

$$dQ_k = Q(x) \frac{dx}{d} \quad (4.37)$$

$$\rightarrow Q_k = \frac{1}{d} \int_0^d Q_0 e^{-x/L} dx \quad (4.38)$$

$$= Q_0 \frac{L}{d} \left(1 - e^{-d/L} \right) . \quad (4.39)$$

In order to account for electron and holes being created at x_0 , Equation 4.39 becomes

$$Q_k = Q_0 \frac{L_e}{d} \left(1 - e^{-(d-x_0)/L_e} \right) + Q_0 \frac{L_h}{d} \left(1 - e^{-x_0/L_h} \right) , \quad (4.40)$$

where the electron and hole drift length L_e and L_h depend on the hole and electron mobility $\mu_{e/h}$ and life-time $\tau_{e/h}$ being different respectively [80].

If the traps are already filled with charge, the density of traps decreases and the life-time of charge carriers increases. This effect is called pumping and is normally done with irradiating the sensor with electrons from a ^{90}Sr source.

The trapping effect is especially pronounced in irradiated sCVD sensors due to a high defect density. However, a non-irradiated sCVD sensor even can show trapping and small polarization effects due to a non-perfect crystal structure.

4.4 Characterization of Diamond Sensors

sCVD sensors of about $5 \times 5 \text{ mm}^2$ and $500 \mu\text{m}$ thickness are produced by Element 6 [84]. Each sensor is characterized by performing different measurements as the optical inspection, leakage current, signal stability and CCE. Only sensors that achieve certain criteria are used for the

BCM1F upgrade.

After receiving the unmetallized sensor, it is optically inspected to determine the overall thickness. Then the sensor is sent to the Princeton University or the GSI for metallization. Afterwards the metallized sensor is again optically inspected to characterize the metallization and electrical measurements are performed as leakage current, signal stability and CCE.

4.4.1 Optical Inspection

Optical measurements of each sensor are done before and after the metallization in order to quantify first of all the sensor dimensions and the metallization area. In addition, mechanical damage of the surface or the metallization is recorded. This inspection is done with a laser microscope using a white light and a laser light source as shown in Figure 38 [85].



Figure 38: Laser Microscope for the optical inspection.

It creates a high resolution colour image and measures at the same time the surface roughness as well as the thickness for transparent materials. The focused laser light scans through the layers of the material and the microscope blocks out-of-focus laser light [86]. It reaches an accuracy of $5.2 \mu\text{m}$ for a sample with an expected thickness of around $500 \mu\text{m}$. A high precision measurement for the sensor thickness is required since the CCE is estimated by using the thickness information. The measurement with the laser provides a three dimensional picture of the sensor as shown in Figure 39. The received geometry of the sensor is displayed.

This sensor has a size of $4.48 \times 4.48 \text{ mm}^2$. However, a detailed analysis of the thickness measurement is needed since the laser microscope assumes to perform the measurement in air with an refractive index of 1. The analysis of the optical measurement is done by a software provided by the producer of the microscope and illustrated in Figure 40.

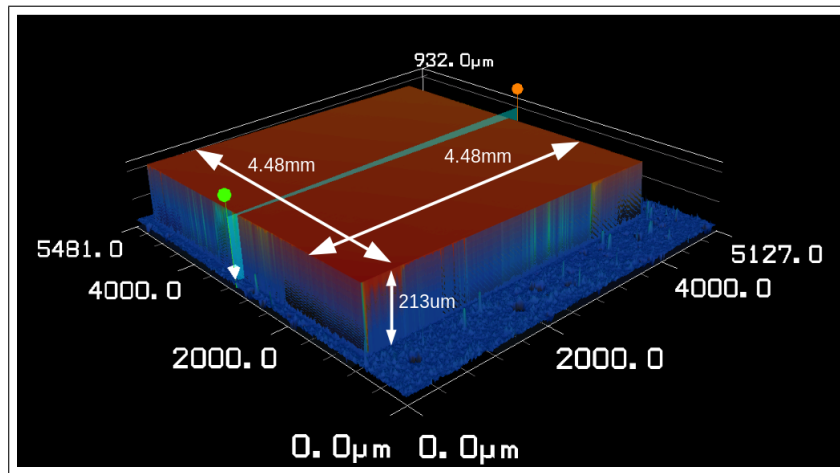


Figure 39: Three dimensional picture of sensor scanned with laser microscope. The geometry of the sensor is highlighted.

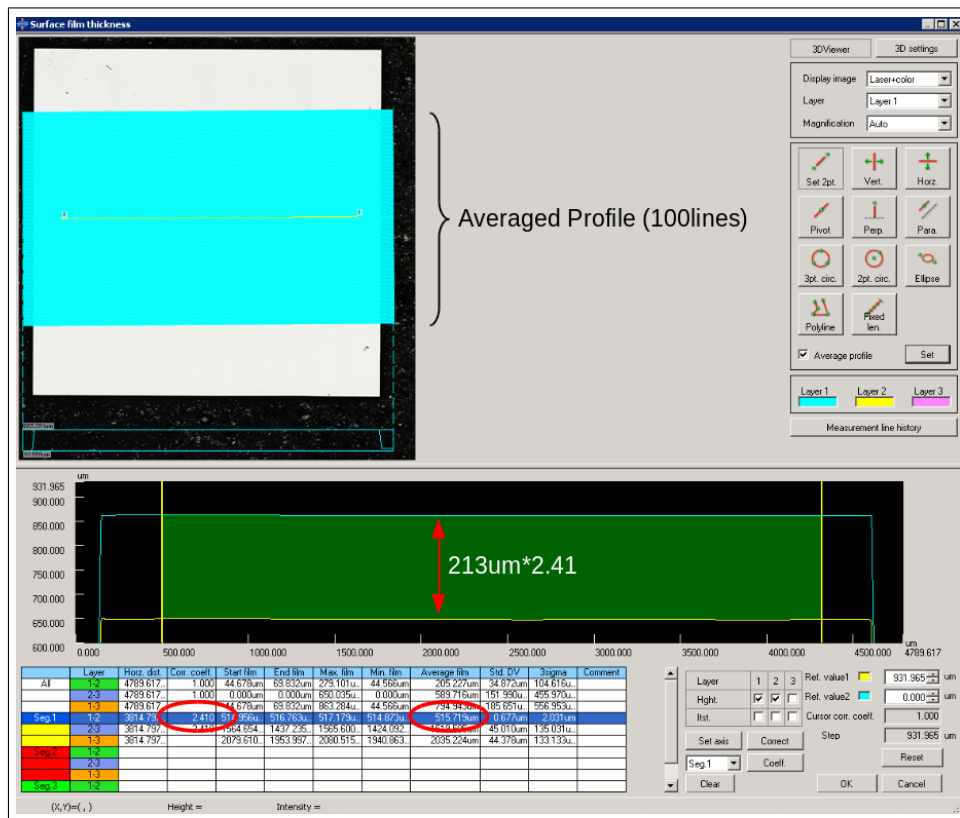


Figure 40: Screenshot of the analysis program of the optical measurement. An image of the sensor is display for choosing the position of the profile measurement and the number of averaged lines. The chart displays the results. A reflection at 647 μm and 861 μm is visible resulting in a thickness of 213 μm. Including the refractive index of 2.41 yields 515 μm sensor thickness displayed in the table below.

Two laser light reflections of diamond are observed, the top and bottom surface. The obtained sensor thickness for the illustrated sensor is 213 μm being less than the expected 500 μm. After

implementing the refractive index of diamond of 2.41 a thickness of $515\ \mu$ is obtained. This measurement is done for both sides of the sensors for checking the thickness values and to record any possible discrepancy. All in all, the thickness of 58 sensors were measured and the distribution of this value is given in Figure 41.

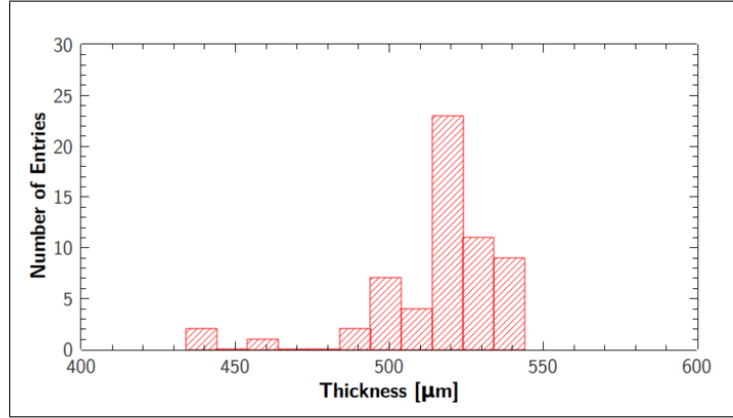
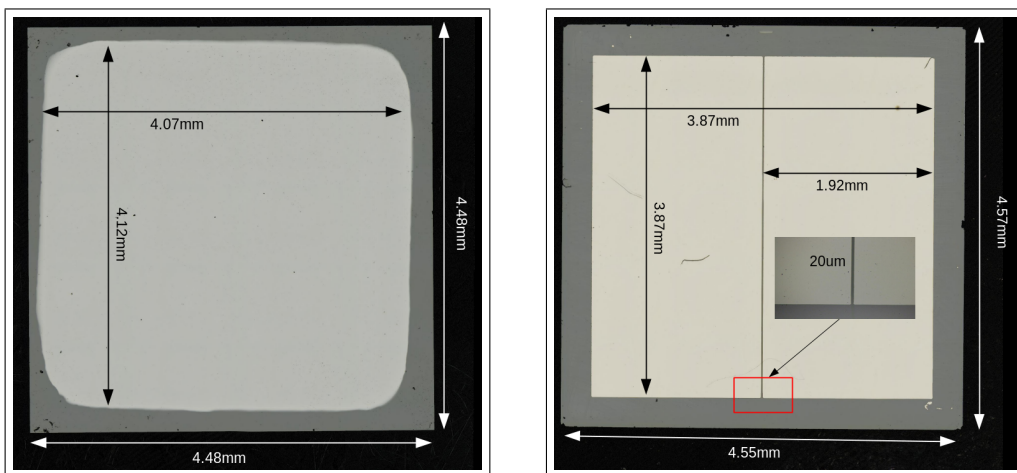


Figure 41: Distribution of the thickness for 59 measured sensors.

When the sensors are metallized another optical inspection is done to verify the metallization area as shown in Figure 42. The two different pad patterns and metallization types are displayed. A one pad metallization done in Princeton University with a W/Ti alloy is illustrated in Figure 42(a). The size of this sensor is $4.48 \times 4.48\ \text{mm}^2$ and the metallization area is roughly $4 \times 4\ \text{mm}^2$ with round edges. Figure 42(b) shows a sensor with a two pad metallization done in the GSI with Cr/Au layers. This sensor has a size of $4.57 \times 4.57\ \text{mm}^2$ and each metallization pad is $3.87 \times 1.92\ \text{mm}^2$ with a gap between both pads of $20\ \mu\text{m}$. The two pad metallization is as well available with the Princeton metallization having the same dimensions.



(a) Picture of a sensor with a one pad metallization done in Princeton University.

(b) Picture of a sensor with a two pad metallization done at the GSI.

Figure 42: Optical inspection of metallized sensors with a one (Figure 42(a)a) and two (Figure 42(b)b) pad metallization. The displayed geometry shows the sensor and metallization dimension as well as the gap between the two metallization areas for the two pad sensor.

4.4.2 Leakage Current

The leakage current measurement is an essential electrical characterization of a sensor. Diamond sensors are insulators and therefore only a very small leakage current at room temperature is expected. However, impurities or crystal defects can deform the energy bands inducing a larger leakage current. This measurement is a first indication if a sensor is suitable for a later detector operation.

In order to measure the leakage current, each sensor is placed in a plastic frame and connected via bonds and wires to the readout electronics as shown in Figure 43(a). In the case of a two pad metallization both pads are interconnected to measure the overall leakage current. In order to define a polarity each sensor is marked on one side of the metallization area. Applying a negative voltage on the marked side is defined as a negative bias voltage. A positive applied voltage defines therefore the positive bias voltage.

A power supply with the capability of setting a bias voltage of 1 kV and a picoammeter with a fluctuation of 20 fA for a current range of 2 nA are used as illustrated in Figure 43(b) [87, 88]. The sensor is located within a shielding box under nitrogen atmosphere while the measurements is performed to avoid pick up noise and surface currents due to moisture.

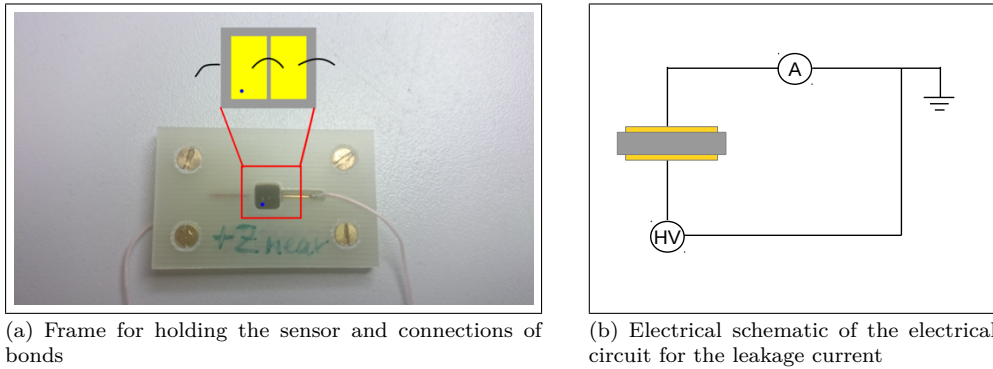
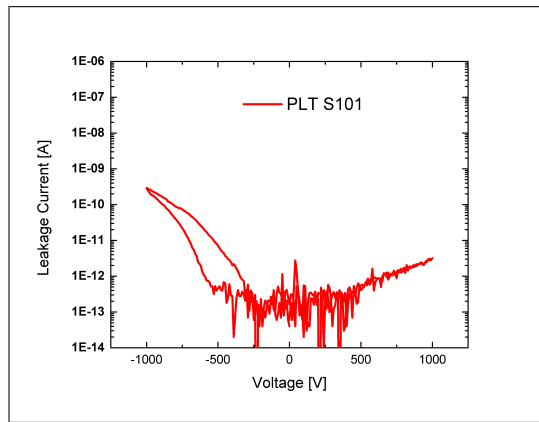
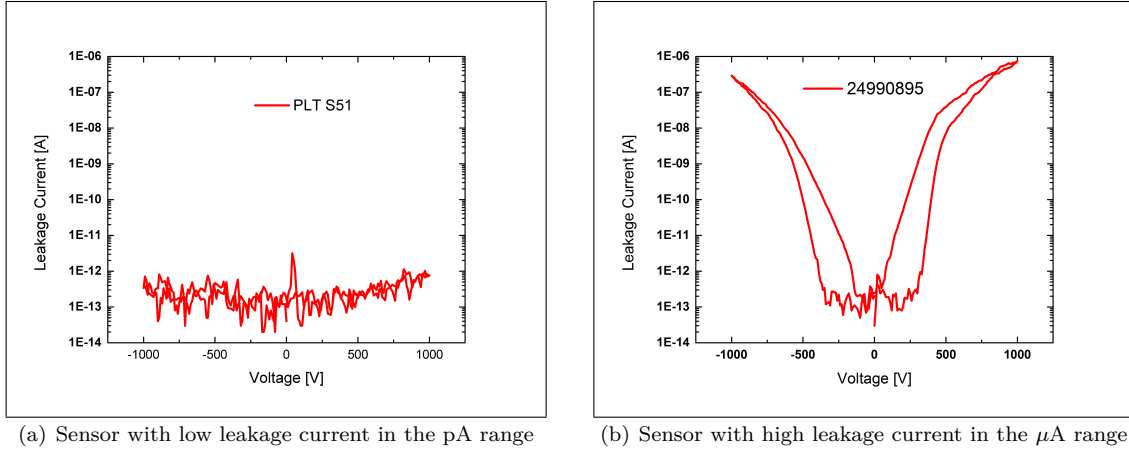


Figure 43: Schematic of the leakage current measurement.

Three measurements of three different sensors are given in Figure 44. The sensor in Figure 44(a) shows a leakage current below 1 pA up to 1 kV bias voltage. The small fluctuations are due to the noise of the electronic setup. Such a results fulfils the expectations of a sCVD sensor. However, Figure 44(b) shows in contrast a sensor measurements with a leakage current up to $1 \mu\text{A}$ for both polarities. This sensor is assumed of not having sufficient quality and a later detector use is excluded. Figure 44(c) illustrates a third case where for the negative polarity the leakage current approaches at 1 kV 300 pA and for the positive polarity up to 3 pA. Sensors with this behaviour are still accepted for a detector operation but preferred with the negative polarity. The different behaviour for the negative and positive polarity is believed to be caused by inhomogeneously distributed defects or a Schottky contact on one sensor side [69].

A first criterion for the selection of sensors for the detector operation arise from this measurements. The sensors must have a leakage current below 100 pA for at least one polarity up to a bias voltage of 1 kV. This criterion is set to ensure that leakage current or erratic current does not have any influence during further characterization measurements.



(c) Sensor with low leakage current for the negative polarity and a high leakage current for the positive polarity.

Figure 44: Leakage current as a function of bias voltage for three sensors having a low and large leakage current.

4.4.3 Signal Stability

The setup for the leakage current measurement also allows to measure the signal stability by placing a ^{90}Sr source on top of the sensor as illustrated in Figure 45. This generates a signal current in the sensor that is observed at a bias voltage of -500 V and $+500\text{ V}$ for 5 h. The bias voltage between $\pm 500\text{ V}$ is set to 0 V for 0.5 h for recovery time in the case the sensor showed polarization or any other internal field effects. A signal current of around 1.5 nA is expected for the given setup and its geometry.

The results of three sensors are shown in Figure 46. A stable signal current with the expected height for both polarities of one sensor is given in Figure 46(a). Some fluctuations in the middle of the signal current at positive polarity is visible but nevertheless this is still assumed as a stable signal current.

In contrast, Figure 46(b) shows the results of a sensor where both polarities are not having the expected performance. First, the signal current is constant and showing the expected signal height for 2.5 h for the positive polarity. Then a jump is visible and the signal current keeps constant at a value by one order of magnitude larger. Such observation were previously made only in

pCVD sensors as given in Reference [89] and quoted as erratic currents appearing suddenly. It is believed that the internal electrical field inside the diamond sensor bulk breaks down as explained in Reference [37]. It illustrates that the crystal structure of this specific sensor is not an ideal single crystal.

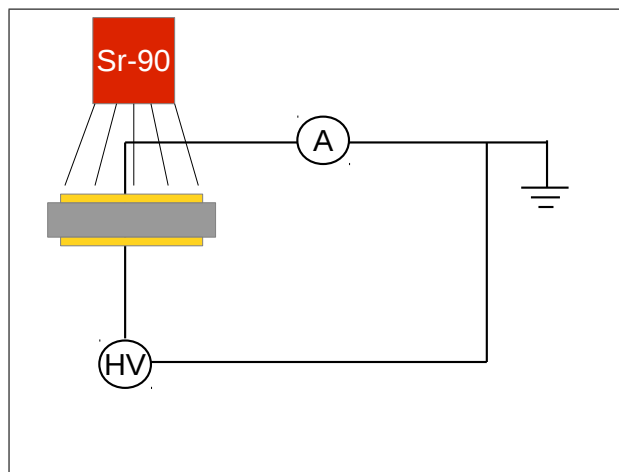
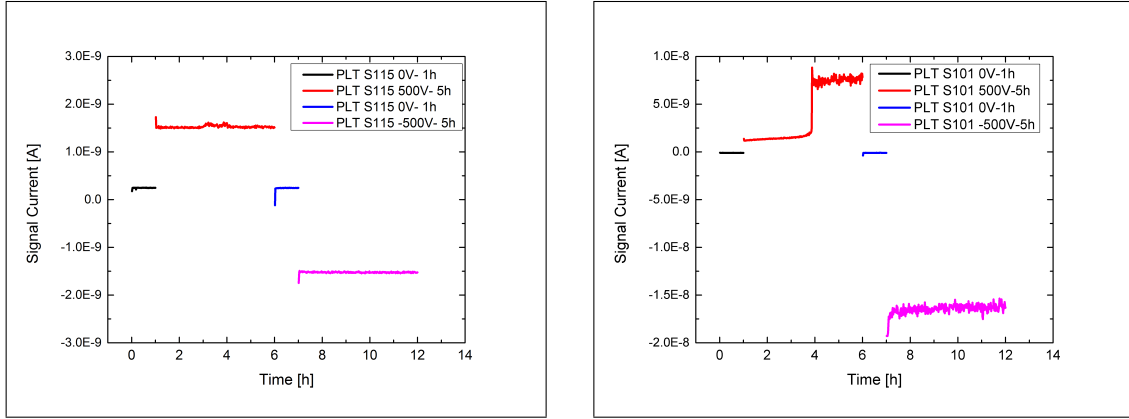


Figure 45: Schematic of the setup for the measurement of the signal stability.

In addition, the signal current of the negative polarity is around one magnitude higher than expected and increasing with time. The leakage current measurement of the same sensor (PLT S101) from Figure 44(c) shows as well an increased leakage current for the negative polarity. This sensor is not considered to be installed in the detector.

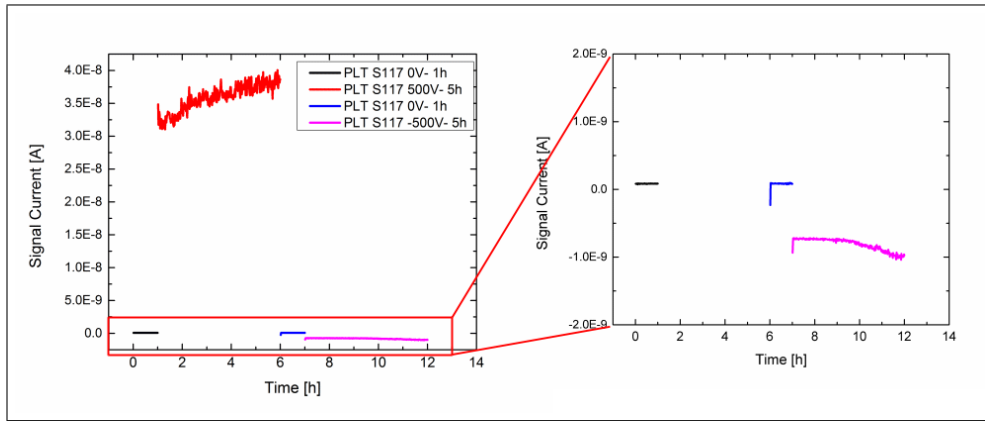
Figure 46(c) represent a sensor having a steadily increasing signal current for the positive polarity due to a high leakage current. The negative polarity has in contrast a slight increase of the signal current going up to 1 nA. Since this increase is still below the expected signal current of 1.5 nA, this polarity is quoted as having an acceptable signal current with a reduced signal height. Such sensors are considered for later operation but only for one polarity being the negative one in this case.

From these measurements it is concluded that a measured high leakage current caused also an unstable or increased signal current and is a criterium for exclusion. Therefore, a selection criterium for sensors is obtained. Sensors must have a stable signal current over the measured time duration of around 2 nA for at least one polarity. Small fluctuation of the signal current up to the set limit are still acceptable.



(a) Sensor with a stable signal current for both polarities

(b) Sensor with unstable signal current for the positive polarity and a high signal current for the negative polarity



(c) Sensor with unstable signal current for the positive polarity and a stable signal current for the negative polarity

Figure 46: Sensor signal as a function of time measured for two sensors having a stable and unstable signal current.

4.4.4 Charge Collection Efficiency

The information about the charge carrier drift length, given by the CCE leads to a measure of the operation performance of each sensor with connected readout electronics. A CCE measurement is performed with the so-called beta-setup box as shown in Figure 47(a). The sensor is placed on the golden high voltage table and a needle connects the sensor metallization to the amplifier. A ^{90}Sr source is located under the high voltage table and electrons are collimated through a little hole of the table and directed to the sensor. The box has also a cover to flood it with dry nitrogen to keep surface currents low. The working principle of this setup is illustrated in Figure 47(b). A bias voltage is connected to one side of the sensor metallization creating an electrical field in the sensor bulk.

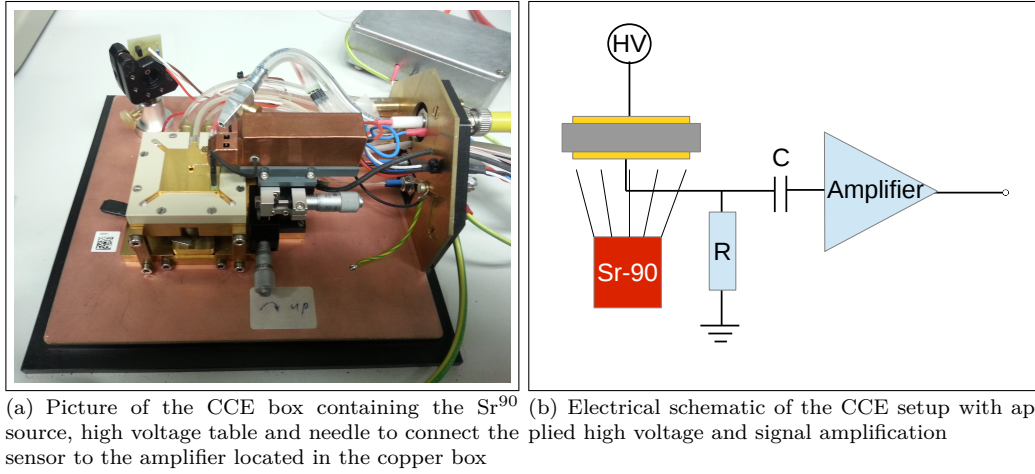


Figure 47: Scheme of the CCE setup.

Electrons from the ⁹⁰Sr source passing through the sensor generating electron-hole pairs being separated by the external electrical field and generating a signal as explained in Chapter 4.3. This signal is read out via a grounded needle and amplified with a charge sensitive amplifier. The charge sensitive amplifier allows a charge calibration by using a test capacitance C_T at the amplifier input and measuring the signal response Q_{cal} of a voltage step ΔV fed into the test capacitance¹¹ with

$$Q_{cal} = C_T \cdot \Delta V . \quad (4.41)$$

Then a shaper with 100 ns shaping time is connected. The amplified and shaped signals is copied by a Fan In-Fan Out (FIFO) module [90]. Both signals are fed into an integrating Analog-to-Digital Converter (ADC)¹² but one copy is delayed by around 400 ns. However, the input signal to the ADC is only measured when the ADC gate is activated. A gate is built by using photomultiplier signals from two scintillators. These scintillators are placed above the sensor on the cover of the box. Only electrons from the ⁹⁰Sr penetrating the sensor and both scintillators will trigger an ADC readout. In addition, the energy deposition in both scintillators must exceed 0.4 MeV. Only then the photomultiplier signal is above the threshold of the Low-Threshold Discriminator (LTD) [92]. Afterwards both LTD signals are fed into a coincidence unit where the logic AND is built. The AND triggers then the Dual Timer allowing to create a rectangular signal with an adjustable delay time and pulse width [93]. This signal is then used as the ADC gate. The arrival time and width of the gate is chosen such that the complete sensor signal is measured with the ADC. The delayed sensor signals being fed into another ADC channel is out of the arrival time of the gate and is used to estimate the noise of the whole readout chain also referred to as pedestal. The complete readout chain and signal with the gate is illustrated in Figure 48.

¹¹A detailed description of a calibration measurement is given in Chapter 6.2

¹²The signal charge is first converted to a voltage by the ADC and then it charges up an integrator capacitance during a fixed amount of time [91]. The ADC measures via a reference voltage the discharge time resulting in a measurement value with arbitrary unit called ADC counts.

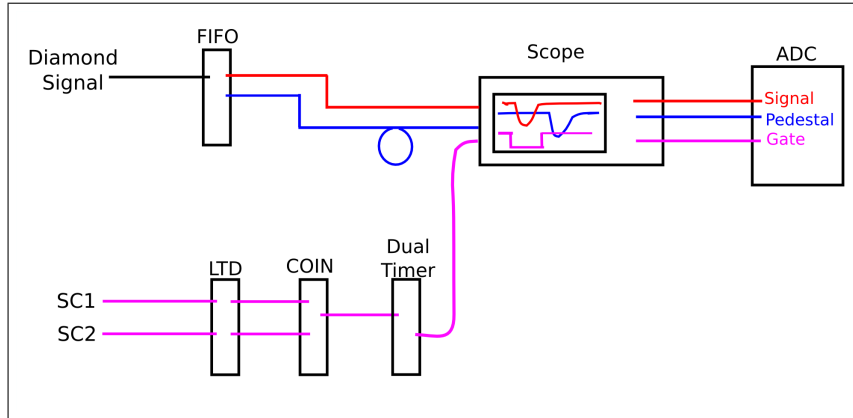


Figure 48: Scheme of signal treatment in the setup for the CCE measurement.

Two ADC spectra for several 10000 incident electrons of the same sensor but with different bias voltages is shown in Figure 49. A pedestal at around 500 ADC counts is visible being fitted with a Gaussian. The pedestal value defines the baseline of the readout chain and the pedestal width the noise of the readout chain. Performing a fit with a Gaussian the mean value μ gives the offset of the readout chain and its standard deviation σ , a measure of the electronic noise are obtained. The signal has its most probable value at about 900 ADC counts and is fitted by a convolution of a Landau distribution with a Gaussian as described in Chapter 4.3. Three parameters are taken to analyse the signal in more detail. The most probable value of the Landau distribution (*MPV*) defines the most probable energy deposition and therefore the signal size. It is different to the mean energy deposition being at higher ADC counts. Both standard deviations of the Landau $\sigma(Landau)$ and Gauss $\sigma(Gauss)$ are as well taken. $\sigma(Landau)$ is defined by the fourth of the full width at half maximum of the Landau distribution, $FWHM = 4\sigma(Landau)$. The standard deviation of the convoluted Gaussian $\sigma(Gauss)$ is comparable to σ of the pedestal.

Figure 49(a) shows the ADC spectrum at a bias voltage of 60 V where the leakage current is in the pA range (see Figure 44(b)). This is as well visible in σ of the pedestal and $\sigma(Gauss)$ of the fit of the Landau distribution convoluted with a Gaussian being relatively small $\sigma = 21$ ADC counts and $\sigma(Gauss) = 38$ ADC counts (see Table 5).

Figure 49(b) shows in contrast an ADC spectrum taken at a bias voltage of 600 V where a large leakage current is observed. Both σ of the pedestal and $\sigma(Gauss)$ of the Landau distribution convoluted with a Gaussian being $\sigma = 109$ ADC counts and $\sigma(Gauss) = 116$ ADC counts are large in comparison to the previously mentioned ones. This observation is due to baseline fluctuations caused by the erratic currents.

However, $\sigma(Landau)$ is constant for both bias voltages being 20 ADC counts that is expected since the deposited energy distribution is not influenced by the leakage current.

If an ADC spectrum as given on Figure 49(b) is observed, the measurement is stopped.

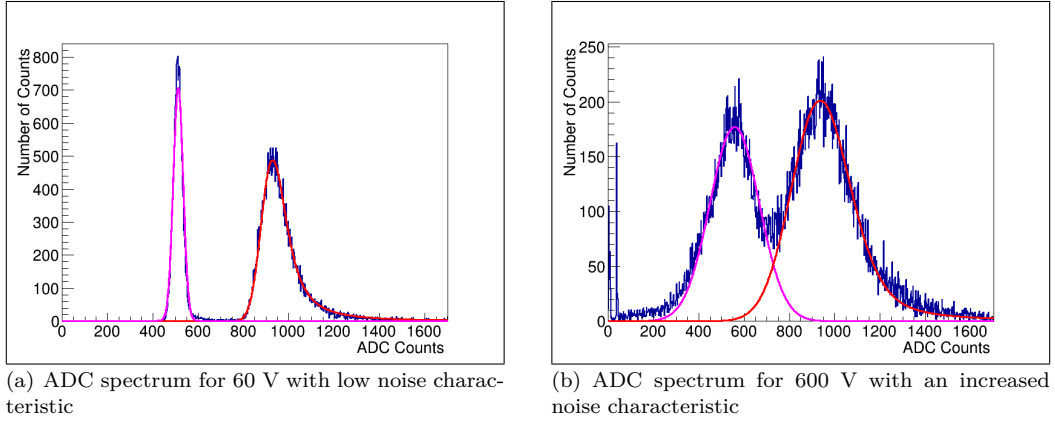


Figure 49: Pedestal and signal distribution for two bias voltages. The pink curve is a Gaussian fit of the pedestal and the red one a Gauss-Landau convolution fit of the signal. In the left distribution the pedestal width is 21 ADC counts and in the right one 110 ADC counts.

Bias Voltage [V]	Pedestal [ADC Counts]	Signal [ADC Counts]
60	$\mu = 513.26 \pm 0.16$ $\sigma = 21.77 \pm 0.11$	$MPV = 913.43 \pm 2.65$ $\sigma (Landau) = 20.54 \pm 3.26$ $\sigma (Gauss) = 38.66 \pm 7.61$
600	$\mu = 557.82 \pm 2.87$ $\sigma = 109.05 \pm 3.09$	$MPV = 902.29 \pm 3.64$ $\sigma (Landau) = 19.67 \pm 3.73$ $\sigma (Gauss) = 116.69 \pm 4.88$

Table 5: Fit parameters of pedestal and signal distribution of Figure 49 measured for 60 V and 600 V.

The signal size is obtained by subtracting μ of the pedestal from the MPV of the signal and the CCE follows:

$$CCE = \frac{[MPV (Signal) - \mu (Pedestal)] \cdot Q_{cal}}{36 \frac{e/h}{\mu m} \cdot d}, \quad (4.42)$$

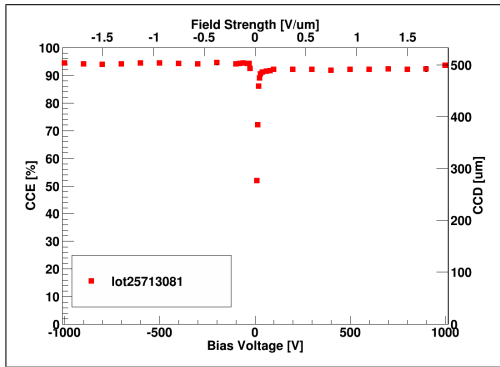
where Q_{cal} is the calibration factor to convert ADC counts to charge and d the sensor thickness determined by the optical measurement.

The CCE as a function of the bias voltage of three different sensors are given in Figure 50. It is increasing until it reaches a saturation voltage. Below the saturation voltage the electrical field is not sufficiently high and a fraction of electron-hole pairs recombines not contributing to the signal. Above the saturation voltage all generated electron-hole pairs are separated and contributing to the signal. Figure 50(a) shows a sensor with small leakage current and a low saturation voltage of 80 V for both polarities. The CCE is measured up to ± 1 kV and the maximum CCE is 95 % for the negative and 92 % for the positive bias voltage. This difference in the CCE might be again due to a dependence of the electrical field on the direction. Nevertheless, this sensor is chosen to be used for the BCM1F.

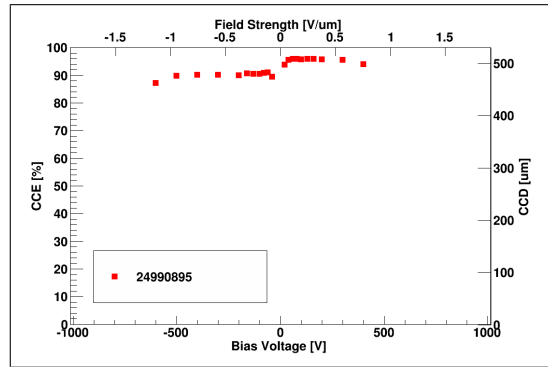
Figure 50(b) shows the CCE measurement of the sensor used to produce Figure 49. Again the saturation voltage is low (below 40 V) but the CCE is only measured up to -600 V and +400 V

due to baseline fluctuations and increased leakage current for higher voltages. However, the CCE reaches a maximum of 90% for the negative and 95% for the positive polarity. An decrease of the CCE is visible at the highest possible bias voltage for both polarities. This might be due to the erratic currents leading to collapse of the internal electrical field causing more recombinations of electron-hole pairs. Sensors with such behaviour for both polarities are not considered for the detector installation.

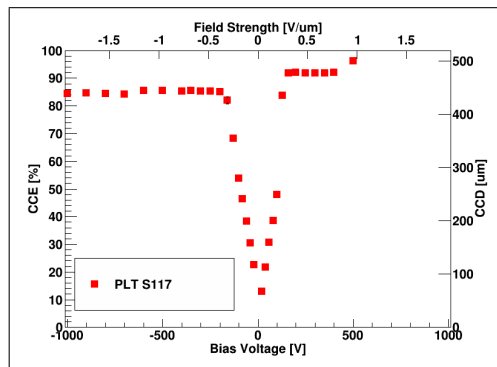
The third sensor in Figure 50(c) shows a saturation above 160 V for both polarities but it reaches only a maximum of 85% for the negative polarity. This observation is in agreement with Figure 46(c) where the signal current for the certain polarity is lower than expected. A reduced CCE is explained by dislocation in the crystal leading to prompt recombination or trapping (see Chapter 4.3.2). This is however not an exclusion criterion if the signal current is stable for this polarity. A higher CCE of 92% is observed for the positive polarity but with a high leakage current above +600 V. The different CCE values for negative and positive polarities CCE is often observed for pCVD sensors as illustrated in Reference [69] and pointing to a non-homogeneous grown sCVD sensor. Even though the sensor has a reduced CCE for the negative polarity it can still be used for the detector operation since the ADC spectra were as shown in Figure 49(a). An operation with a positive polarity for this sensor is however excluded.



(a) CCE of a sensor with a low leakage current.



(b) CCE of a sensor with a high leakage current.



(c) CCE of a sensor with an asymmetric behaviour

Figure 50: CCE as a function of bias voltage for two sensors having a low and high leakage current.

Summarizing, sensors must have at least one polarity with low leakage current and ADC spectra as shown in Figure 49(a) resulting in a stable CCE measurement up to 1 kV are considered for the BCM1F installation.

4.5 Characterization Results of NonIrradiated Diamond Sensors

All in all 58 sensors with a two pad metallization are fully characterized to obtain an overall knowledge about the electrical behaviour of each sensor and to select the sensors with the best performance to be used for BCM1F. Four different production batches of sensors were available:

- batch 0228 with 7 sensors
- batch 0390 with 23 sensors
- batch PLT with 22 sensors
- batch SC0 with 6 sensors

For each sensor first the leakage current is measured as a function of the bias voltage and second the signal current stability is checked. Afterwards the CCE measurement is performed. The results of all sensors are listed in Table 6 for the maximum measured leakage current for both polarities, the classification of signal stability at ± 500 V and the maximum CCE value for where σ (*Gauss*) is stable.

An overview of the measurements of the leakage current of all four batches is given in Figure 51. The number of sensors having a leakage current below a certain value at 1 kV for at least one polarity or both polarities is shown. Sensors having a leakage current below 100 pA at 1 kV for at least one polarity meet the selection criteria given in Chapter 4.4.2.

It is visible that batch 0228 has only one sensor matching this criterion for only one polarity. All other sensors and polarities have a large leakage current even up to $1 \mu\text{A}$.

The above given criterion is matched by 20 sensors of batch 0390, 17 sensors of batch PLT and 5 sensors of batch SC0 resulting in a total of 42 sensors. However, most of the sensors show a leakage current higher than 100 pA at one polarity of 1 kV. This is so far not understood. Only 8 sensors of batch 0390, 7 sensors of batch PLT and 4 sensors of batch SC0 have a leakage current below 100 pA for both polarities resulting in a total number of 19 sensors.

Batch	Sensor Name	Leakage Current [A]		Signal Stability [A]		Charge Collection Efficiency [%] (max. bias voltage)	
		negative polarity	positive polarity	negative polarity	positive polarity	negative polarity	positive polarity
0228	23537021	1E-09	1E-08	acceptable	increasing	92 (800V)	89 (700V)
0228	23851341	1E-06	1E-07	increasing	increasing	- (0V)	90 (600V)
0228	23851342	1E-08	1E-10	increasing	acceptable	90 (700V)	94 (1kV)
0228	23851343	1E-09	1E-06	increasing	increasing	80 (600V)	- (0V)
0228	23851353	1E-07	1E-06	increasing	increasing	90 (500V)	87 (400V)
0228	24662652	1E-06	1E-06	increasing	increasing	98 (250V)	95 (700V)
0228	24763371	1E-06	1E-10	increasing	acceptable	92 (100V)	90 (900V)
0390	24939221	1E-12	1E-07	perfect	increasing	95 (1kV)	95 (1kV)
0390	24939222	1E-11	1E-11	acceptable	acceptable	90 (1kV)	98 (1kV)
0390	24939223	1E-08	1E-10	increasing	perfect	95 (1kV)	95 (1kV)
0390	24939224	1E-10	1E-09	perfect	increasing	95 (1kV)	95 (1kV)
0390	24939225	1E-10	1E-11	acceptable	perfect	92 (1kV)	90 (1kV)
0390	24968755	1E-08	1E-11	increasing	perfect	95 (500V)	98 (1kV)
0390	24968763	1E-11	1E-09	perfect	increasing	98 (1kV)	98 (1kV)
0390	24968764	1E-08	1E-11	increasing	acceptable	90 (600V)	92 (900V)
0390	24968775	1E-10	1E-09	acceptable	perfect	95 (1kV)	85 (1kV)
0390	24968785	1E-06	1E-06	increasing	increasing	90 (500V)	95 (400V)
0390	24990884	1E-10	1E-09	perfect	increasing	80 (1kV)	95 (1kV)
0390	24990885	1E-07	1E-07	increasing	increasing	95 (400V)	95 (500V)
0390	24990891	1E-11	1E-11	increasing	perfect	90 (1kV)	90 (1kV)
0390	24990892	1E-08	1E-11	increasing	perfect	95 (400V)	95 (1kV)
0390	24990893	1E-11	1E-09	perfect	increasing	95 (1kV)	90 (400V)
0390	25713092	1E-10	1E-12	increasing	increasing	90 (600V)	85 (900V)
0390	25713095	1E-11	1E-11	perfect	perfect	95 (1kV)	95 (1kV)
0390	25713096	1E-11	1E-09	acceptable	perfect	90 (1kV)	87 (800V)
0390	25713081	1E-12	1E-12	perfect	increasing	95 (1kV)	92 (1kV)
0390	25713083	1E-11	1E-11	perfect	increasing	95 (1kV)	95 (700V)
0390	25713084	1E-11	1E-11	increasing	acceptable	95 (1kV)	95 (1kV)
0390	25713085	1E-12	1E-12	acceptable	perfect	95 (1kV)	90 (1kV)
0390	25713086	1E-11	1E-11	perfect	acceptable	90 (1kV)	90 (1kV)
PLT	S134	1E-09	1E-08	increasing	increasing	95 (500V)	95 (400V)
PLT	S121	1E-11	1E-08	perfect	acceptable	95 (1kV)	95 (600V)
PLT	S119	1E-12	1E-12	perfect	increasing	95 (1kV)	85 (1kV)
PLT	S117	1E-11	1E-07	perfect	increasing	85 (1kV)	92 (500V)
PLT	S115	1E-12	1E-12	perfect	perfect	88 (1kV)	95 (1kV)
PLT	S107	1E-07	1E-12	increasing	perfect	95 (600V)	90 (1kV)
PLT	S101	1E-09	1E-11	acceptable	increasing	95 (60V)	90 (1kV)
PLT	S111	1E-10	1E-10	acceptable	increasing	85 (1kV)	85 (1kV)
PLT	S98	1E-12	1E-06	acceptable	increasing	93 (250V)	95 (1kV)
PLT	S85	1E-09	1E-08	increasing	acceptable	95 (500V)	90 (500V)
PLT	S82	1E-11	1E-09	perfect	increasing	90 (1kV)	92 (400V)
PLT	S80	1E-12	1E-11	increasing	perfect	95 (1kV)	95 (500V)
PLT	S73	1E-11	1E-11	perfect	perfect	95 (500V)	80 (1kV)
PLT	S69	1E-11	1E-11	perfect	acceptable	95 (1kV)	95 (600V)
PLT	S67	1E-12	1E-06	increasing	increasing	75 (60V)	70 (400V)
PLT	S65	1E-12	1E-12	acceptable	acceptable	95 (1kV)	88 (1kV)
PLT	S63	1E-09	1E-09	increasing	increasing	92 (700V)	85 (1kV)
PLT	S55	1E-10	1E-08	perfect	perfect	90 (1kV)	95 (600V)
PLT	S53	1E-07	1E-10	acceptable	increasing	75 (800V)	90 (1kV)
PLT	S51	1E-12	1E-12	perfect	perfect	92 (1kV)	92 (1kV)
PLT	S16	1E-08	1E-06	increasing	increasing	95 (600V)	95 (500V)
SC0	1001	1E-10	1E-11	increasing	increasing	95 (1kV)	90 (1kV)
SC0	1030	1E-12	1E-10	perfect	increasing	90 (1kV)	90 (800V)
SC0	1735	1E-10	1E-10	increasing	increasing	85 (1kV)	95 (900V)
SC0	1761	1E-10	1E-10	increasing	increasing	95 (500V)	95 (500V)
SC0	1215	1E-11	1E-06	increasing	increasing	85 (100V)	90 (400V)
SC0	1683	1E-08	1E-06	increasing	increasing	60 (100)	87 (160)

Table 6: Summary of the sensor characterization

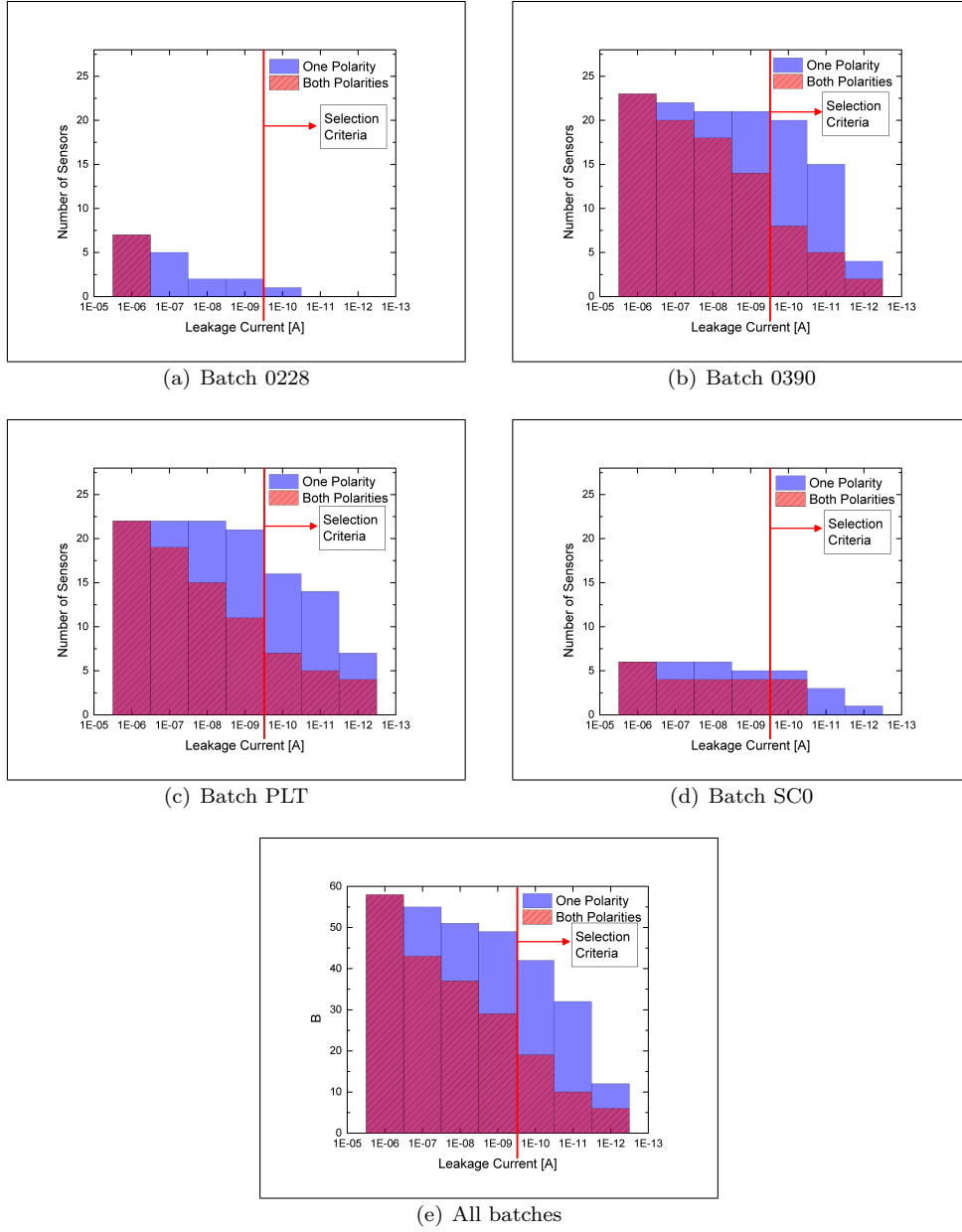


Figure 51: Sensor quality of all batches classified by the number of sensors having a leakage current below a certain value for at least one polarity (blue) or both polarities (red).

Figure 52 illustrates the quality of the sensors by looking at the signal stability at ± 500 V for at least one polarity and both polarities. Only sensors with a perfect or acceptable signal current for at least one polarity fulfil the selection criteria as mentioned in Chapter 4.4.3.

Again only two sensors of batch 0228 show a stable signal current only for one polarity being quoted as acceptable. The rest of the sensors have a steadily increase of the signal current or an erratic behaviour. A similar behaviour is observed for the sensors of batch SC0.

16 sensors of batch 0390 and 13 sensors of batch PLT show a perfect signal current for at least one polarity but only 3 of the PLT batch and none of the 0390 batch for both polarities. All in all, 40 sensors with at least one acceptable signal current behaviour fulfil the selection criteria but only

15 of them for both polarities with 7 sensors from batch 0390 and 8 sensors of batch PLT. Again most of the sensors have a stable signal current for one polarity only but an increased leakage or erratic current for the other polarity.

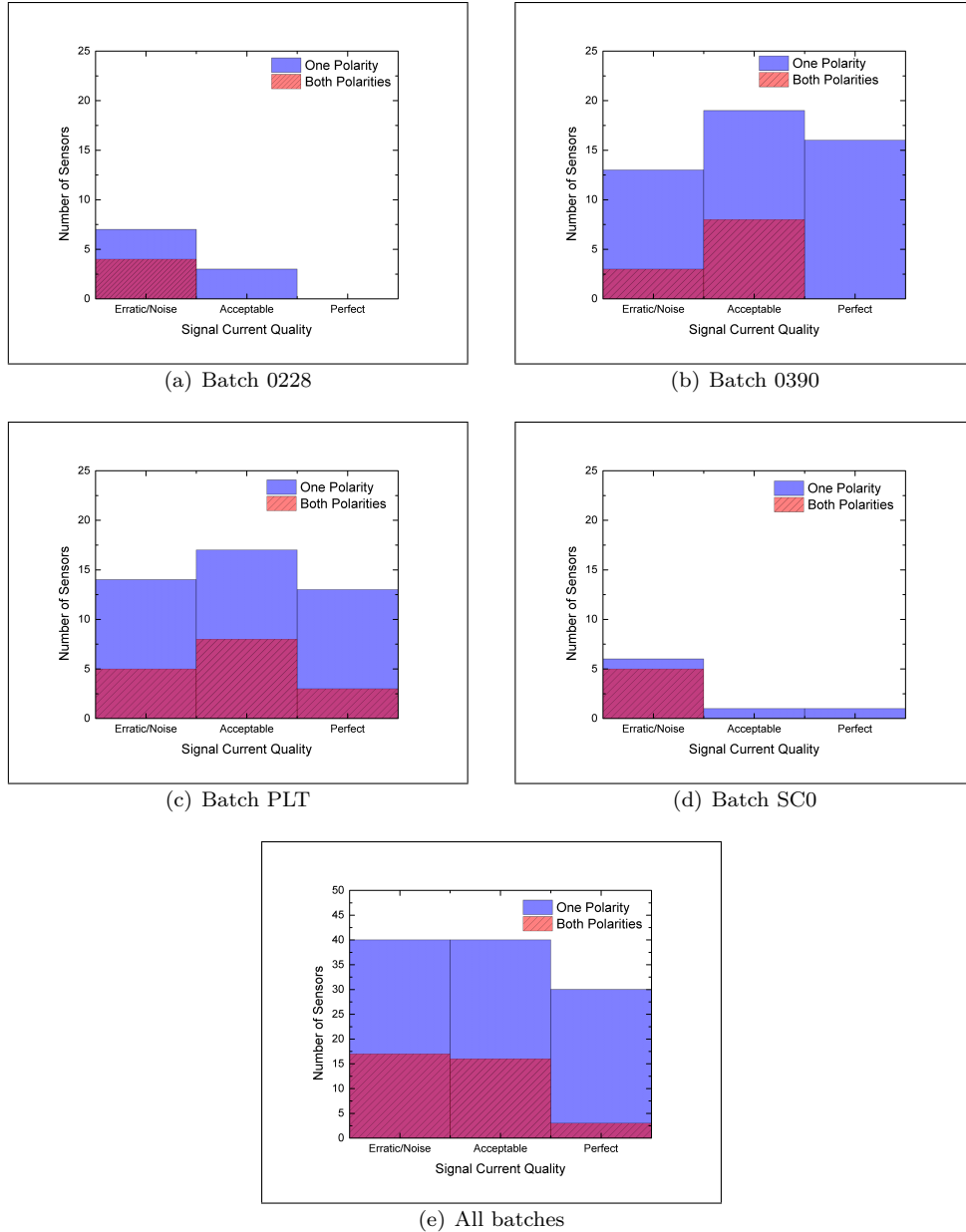


Figure 52: Sensor quality for all batches classified by the number of sensors showing a perfect, acceptable and erratic/noise signal current.

A similar picture of the sensor quality is given by the CCE results shown in Figure 53. The sensors are classified by the maximum possible bias voltage applied to the sensors without showing an increased leakage current with a large σ (*Gauss*) for at least one or both polarities. The last bin of each plot represents the number of sensors holding a bias voltage of 1 kV and meet therefore the selection criterion.

Again batch 0228 has only one sensor holding 1 kV for one polarity being the same sensor as in the previous measurements with a leakage current below 100 pA and an acceptable signal current stability (see sensor 23851342 in Table 6). Summarizing, there is only one sensor of batch 0228 matching all three selection criteria of the characterization measurements. All other sensors of this batch have an increased leakage current behaviour resulting in a broadening of the pedestal peak in the ADC spectrum.

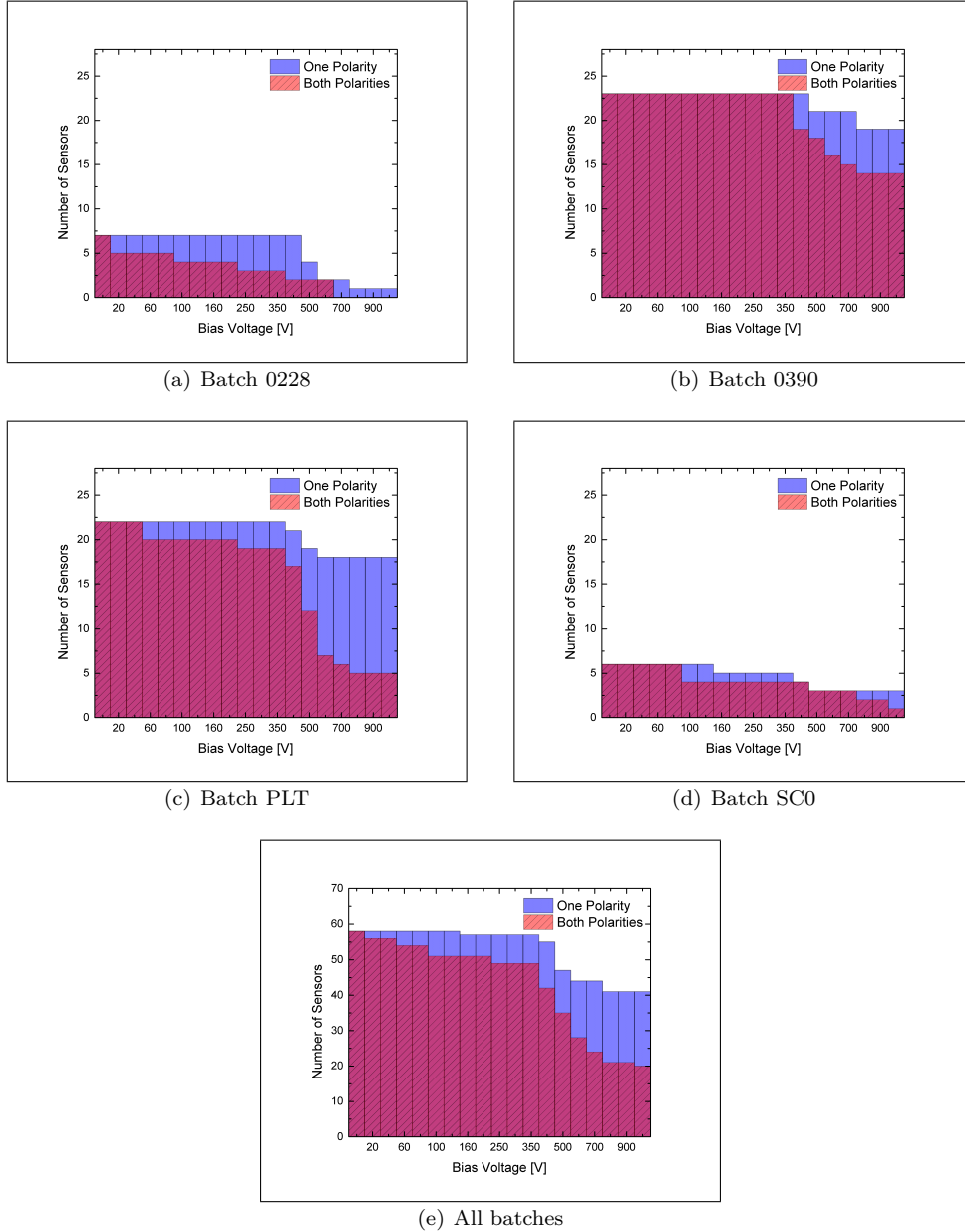


Figure 53: Sensor quality classified by the number of sensors holding a certain bias voltage used to perform the CCE measurement.

19 sensors of batch 0390 meet the selection criterion and even 14 out of them for both polarities. Batch PLT contains 18 sensor matching the selection criterion but only 5 with both polarities.

Again, most of the sensor show a stable CCE measurement up 1 kV only for one polarity as shown in Figure 50(c). Three sensors of the SC0 batch hold 1 kV for at least one polarity but none of them for both polarities.

All in all, 41 sensor show a stable CCE measurement up to 1 kV for one polarity and 20 of them for both polarities.

Table 7 summarises the quality characterization and lists the number of sensor fulfilling the selection criteria with the classification of one polarity or both polarities. Batch 0228 and batch SC0 contain one sensor that meet all three criteria. 17 sensor of batch 0390 and 14 sensors of batch PLT can be potentially used. However, only 5 of batch 0390 meet all three selection criteria for both polarities and only 4 for the PLT batch. This results in a total number of 33 sensors meeting all three selection criteria but only 9 of them for both polarities. These 9 sensors are of course preferred for the detector installation but a total number of sensors of 24 is needed (see Chapter 3.1). Therefore, sensors matching the three selection criteria for only one polarity need to be installed but with a potentially higher risk of a malfunctioning of these sensors.

Sensor Batch	0228	0390	PLT	SC0_299	all
Number of Sensors	7	23	22	6	58
One Polarity	1	17	14	1	33
Both Polarities	0	5	4	0	9

Table 7: Summary of sensor meeting all three selection criteria for one and both polarities.

4.6 Characterization of Metallization

Few sensors not matching the above selection criteria are metallized first with the Princeton W/Ti metallization and then with the GSI Cr/Au metallization in order investigate a possible impact of the metallization type on the leakage current behaviour. Figure 54 shows the leakage current for the W/Ti and Cr/Au metallization measured with two sensors named 23537021 and 23821342 of batch 0228.

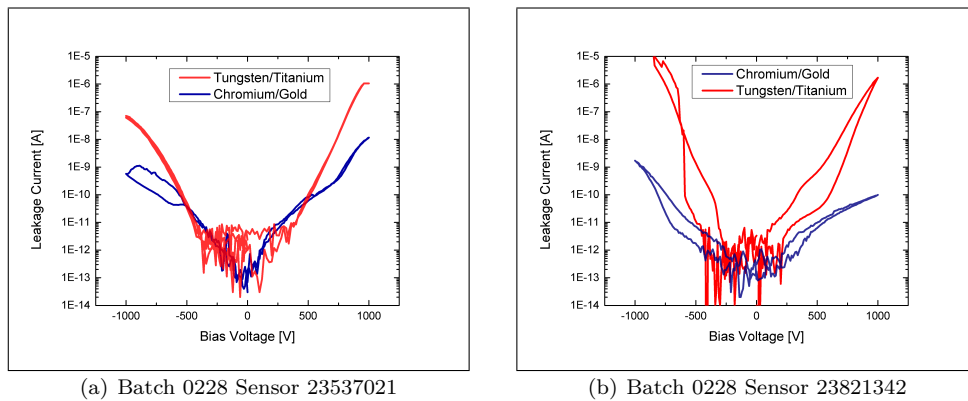
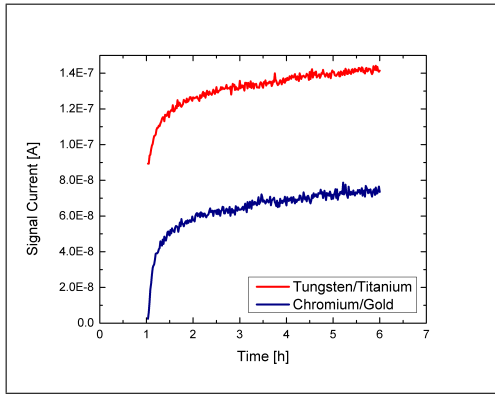


Figure 54: Comparison of leakage current for W/Ti (red) and Cr/Au (blue) metallization for sensor 23537021 and 23821342.

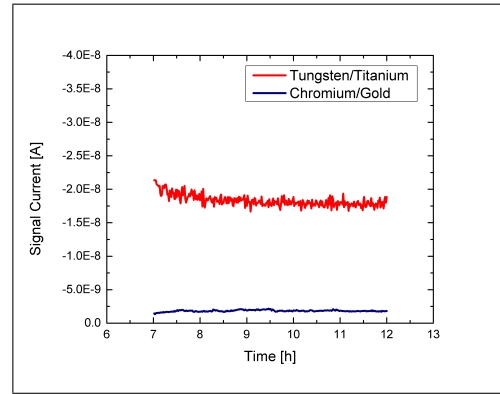
The leakage current of 23537021 in Figure 54(a) with the Cr/Au metallization is two magnitudes smaller than with the W/Ti metallization. Similar results are obtained for the sensor 23821342

given in Figure 54(b) where the leakage current of the Cr/Au metallization is even four magnitudes smaller than the W/Ti one. It is believed that the reason for this observation is the titanium forming a carbide leading to an increase of an already existing leakage current due to the lowering of the Schottky barrier [94]. Nevertheless, the measured leakage current is above 100 pA for all four cases pointing also to a material defect.

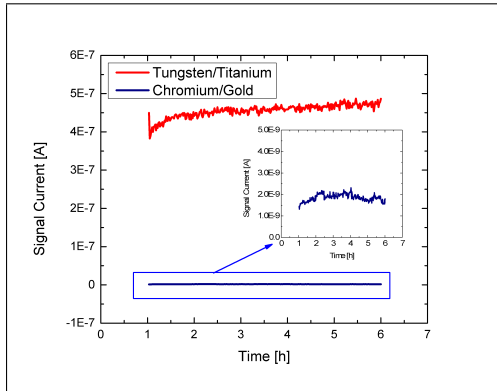
In addition, the signal stability at ± 500 V for both sensors and metallizations is measured and shown in Figure 55. The signal current at +500 V for the sensor 23537021 shows the same increase for both metallizations (see Figure 55(a)). The signal height is lower for the Cr/Au metallization but still above the set selection criterion. A similar observation is done for the signal current at -500 V (Figure 55(b)) with a signal height of the Cr/Au metallization fulfilling now the selection criterion. The signal height of the W/Ti metallization is one magnitude higher and does not meet the selection criteria.



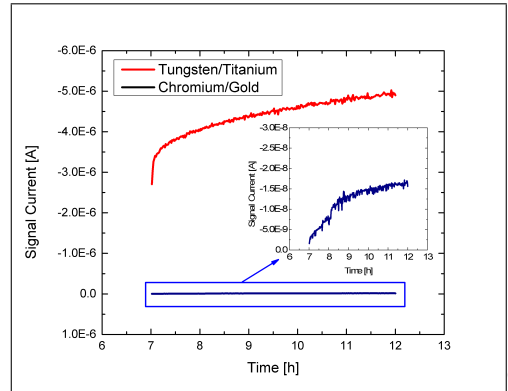
(a) Batch 0228 Sensor 23537021 with +500 V bias voltage



(b) Batch 0228 Sensor 23537021 with -500 V bias voltage



(c) Batch 0228 Sensor 23821342 with +500 V bias voltage



(d) Batch 0228 Sensor 23821342 with -500 V bias voltage

Figure 55: Signal stability at ± 500 V for W/Ti (red) and Cr/Au (blue) metallizations measured for sensor 23537021 (55(a) and 55(b)) and 23821342 (55(c) and 55(d)). 55(c) and 55(d) contain a zoom of the signal stability for the Cr/Au metallization.

This effect is even more pronounced for the sensor 23851342. The signal current for the Cr/Au metallization at +500 V match the selection criteria and its height is even 2 magnitudes smaller than for the W/Ti metallization (see Figure 55(c)). A similar behaviour is given for -500 V (see Figure 55(d)) but both metallizations are outside the set criteria. The increased signal height for

the W/Ti metallization corresponds to the leakage current being as well larger.

The comparison of the leakage current and signal stability of the W/Ti and Cr/Au metallization show an improvement of the performance with the Cr/Au metallization. It has to be pointed out that the overall signal characteristic is the same for both metallizations best seen in Figure 55(a). This points to a material defect producing a non stable signal current with a large leakage current. In addition, a comparison of the metallization pattern is done where a sensor is first metallized with two pads and then remetallized with one pad. This is done to exclude a failure during the metallization process with two pads.

Two sensors of batch 0390, 24968764 and 24939222, are randomly chosen for this test. Figure 56(a) shows the leakage current for sensor 24968764 being in the pA range for the one pad sensor at both bias voltages. However, the two pad metallization shows an increased leakage current being three magnitudes higher for the negative and one magnitude for the positive polarity.

The leakage current for the two pad metallization of sensor 24939222 is in contrast around 100 pA and three magnitudes smaller at negative bias voltage than for the one pad metallization as given in Figure 56(b). A leakage current below 100 pA at positive bias voltage is observed for the one and two pad metallization.

In general an improvement of the leakage current is not observed by using the one or two pad metallization.

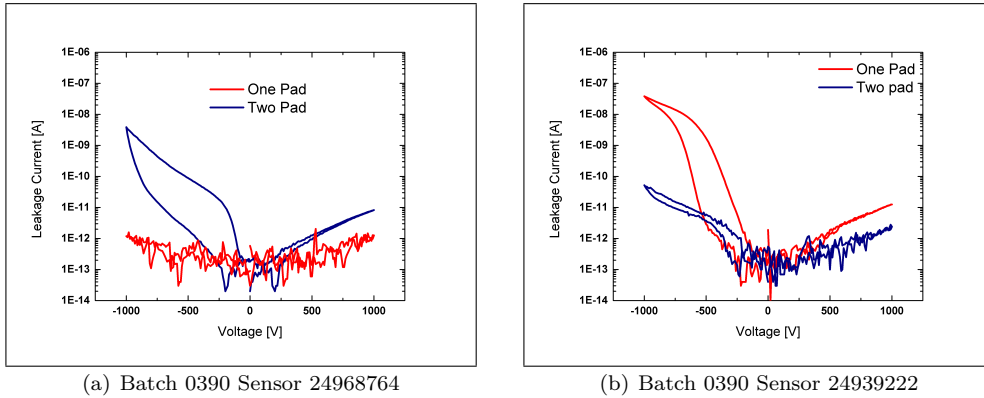
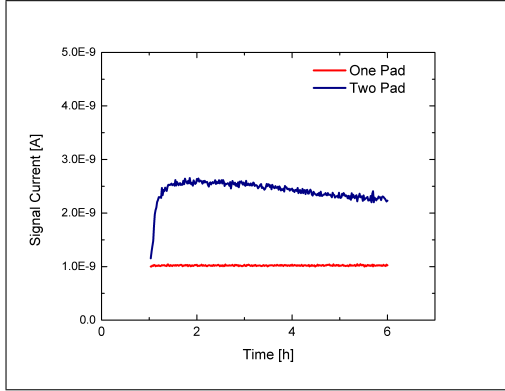


Figure 56: Comparison of leakage current for one (red) and two (blue) pad metallization for sensor 24990891 and 24939222. In both cases the W/Ti metallization is used.

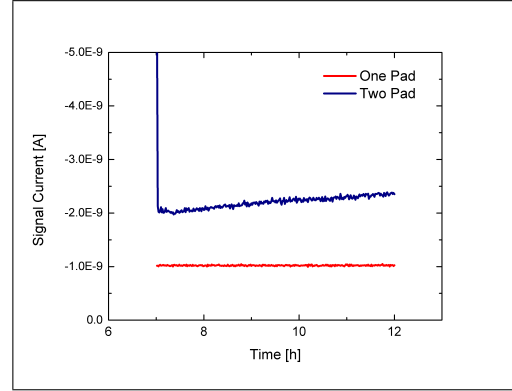
Figure 57 shows the sensor signal as a function of time for sensor 24968764 and 24939222 at ± 500 V. The signal current of sensor 24968764 meets the selection criterion at both polarities for the one pad metallization (see Figure 57(a) and Figure 57(b)). However, an increased signal height is observed for the two pad metallization for both polarities. The signal current is stable but does not meet the selection criterion. This sensor also showed a higher leakage current for the two pad metallization.

In contrast, the signal current as a function of time for sensor 24939222 and the two pad metallization meet again the selection criteria for both bias voltages (see Figure 57(c) and Figure 57(d)). However, the one pad metallization meets the selection criterion only at positive bias voltage. A signal current far above the expectation is observed for the negative polarity being one magnitude higher than for the two pad metallization. The leakage current measurement has also shown large values for the negative polarity.

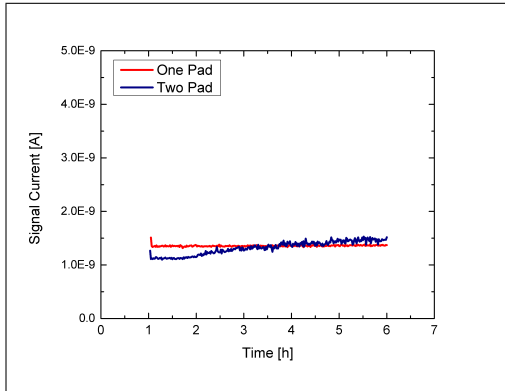
Summarizing, the signal current as a function of time is in one case improved and in the other case worsened by using the one or two pad metallization. No conclusion can be drawn.



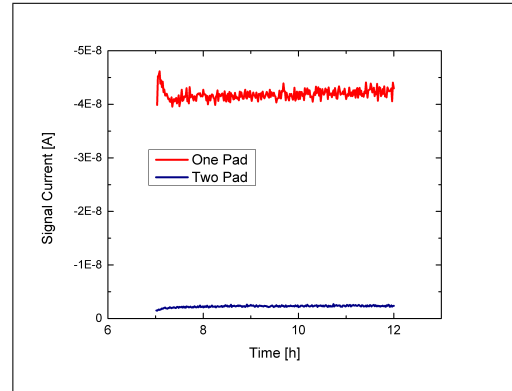
(a) Batch 0390 Sensor 24968764 with +500 V bias voltage



(b) Batch 0390 Sensor 24968764 with -500 V bias voltage



(c) Batch 0390 Sensor 24939222 with +500 V bias voltage



(d) Batch 0390 Sensor 24939222 with -500 V bias voltage

Figure 57: Signal current as a function of time at ± 500 V for one and two pad metallization measured for sensor 24968764 (57(a) and 57(b)) and 24939222 (57(c) and 57(d)). The W/Ti metallization is used in all measurements.

5 Test-Beam of the Upgraded Beam Conditions Monitor

In order to test the complete front-end chain of BCM1F, a prototype consisting of sensor, front-end ASIC and opto-hybrid was tested at the DESY II test-beam area using an electron beam. The chapter will explain the test-beam area and the components used.

5.1 Test-Beam Area

DESY II is an electron/positron ring accelerator with a circumference of 292.8 m and a revolution frequency of 1 MHz. The acceleration takes place in a sinusoidal mode with a radio frequency of 500 MHz and a repetition frequency of 12.5 Hz. One electron/positron bunch has a length of 30 ps. The functionality of the test-beam area is shown in Figure 58. After the acceleration of the electrons or positrons, a carbon fibre is moved near to the beam. Electrons of the beam halo generate Beamstrahlung. A fraction of the Bremstrahlung photons convert in a metal layer to electrons and positrons [95].

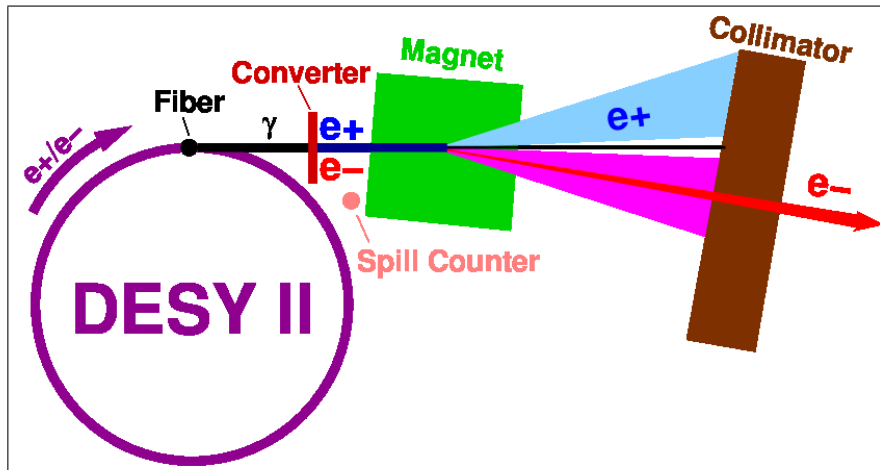


Figure 58: Schematic layout of the test-beam area.

The electrons and positrons are horizontally spread out with a dipole magnet. A collimator forms then the extracted beam. The energy of the electrons can be chosen from 1 GeV to 6 GeV by adjusting the magnetic field of the dipole. The energy loss of electrons within this energy range is within approximately 10% equal to a MIP.

The energy for the BCM1F test-beam was set to 5 GeV. The rate was 100 Hz and the beam size $8 \times 8 \text{ mm}^2$.

The test-beam facility provides already a pixel beam telescope, called EUDET telescope, for the track reconstruction. It consists of two arms with 3 planes each that are positioned along the beam axis. Additionally, the complete table, where the planes are fixed, can be moved by a mechanical screw driver in order to guarantee that all 6 planes are centered to the beam axis. In between of the two telescope arms is a X-Y table located where the device-under-test (DUT), the BCM1F prototype, is mounted. Its position relative to the beam axis can be changed. Two scintillators are located upstream and downstream of the first and last telescope plane to trigger on particles passing the telescope. A picture of the setup schematic including the telescope planes, scintillators

and DUT is shown in Figure 59.

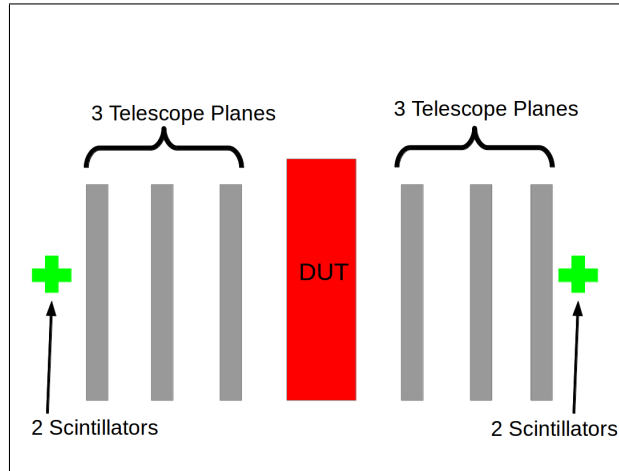


Figure 59: Scheme of the test-beam setup including the 6 telescope planes, 2 scintillators at each end and the device-under-test.

The data taking was done with several devices and computers. First of all the signals of the four scintillators are sent to a Trigger Logic Unit (TLU) that generates a logic “AND” of all four input signals and a trigger number [96]. Both informations are distributed to the telescope and DUT readout crate in order to trigger the readout and to save the data files including the trigger number. While the TLU transfers the information, it asserts a busy signal and new incoming triggers are blocked. Figure 60 shows the complete trigger and signal processing used for the test-beam.

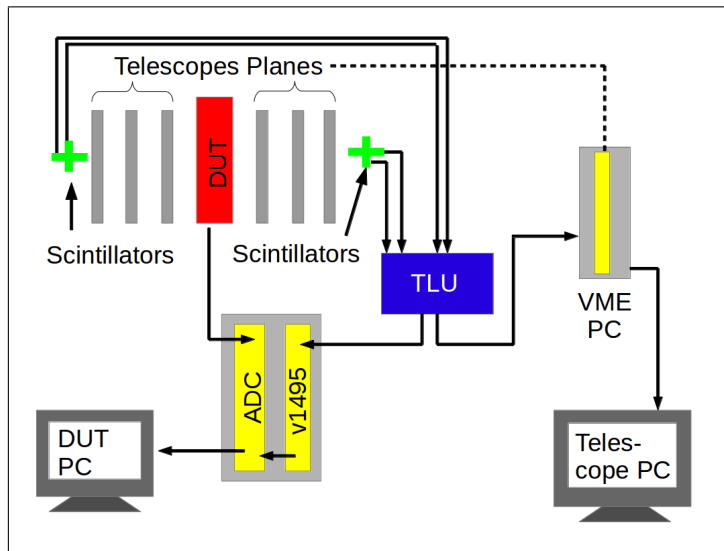


Figure 60: Scheme of trigger, telescope and DUT signal processing including the two readout crates and computers for the telescope and the DUT.

The 6 telescope planes are read out with VME cards and processed with on-board FPGAs. Data of the telescope planes are then transmitted to a Motorola VME computer, located in the telescope readout crate, where the data and trigger number is combined. Then the information is sent to a Telescope computer via Ethernet connection and a raw data file is saved containing information

from all sensors and the corresponding trigger number [97].

The DUT is also connected to a readout crate where the two back-end modules are located. First, the crate holds a CAEN v1495 trigger-logic-unit that receives the trigger signal and trigger number from the TLU. Second, a CAEN v1721 ADC is triggered by the v1495 trigger logic and used to digitize the signal from the sensor. A DUT computer reads out the ADC and v1495 trigger logic at the same time in order to save the information of the DUT and the corresponding trigger number. A picture of all devices used in the test-beam area is given in Figure 61.

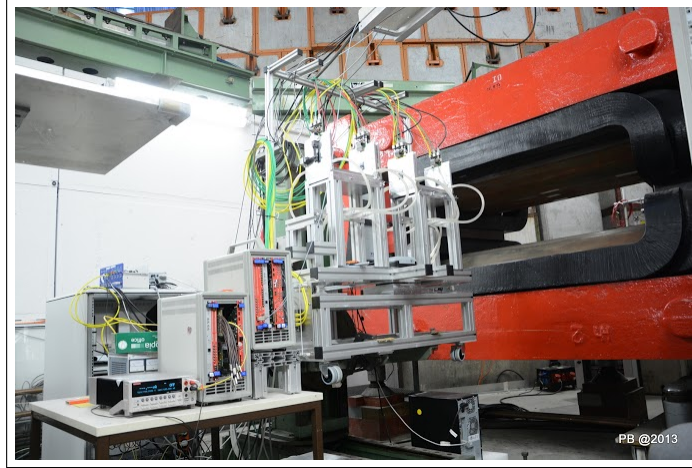


Figure 61: Picture of test-beam area including the telescope planes and the back-end electronic for signal readout.

5.2 The Pixel Beam Telescope

The telescope used is an EUDET telescope designed to enhance the test-beam infrastructure particular for detector research and development. It can be moved in Z-direction in order to change the distance between telescope planes.

The 6 telescope planes are equipped with MIMOSA-26¹³ sensors that perform online data sparsification and have a signal-to-noise ratio for MIPs of 20-40 [98]. Each sensor has nearly 0.7 millions of pixels, subdivided in 1152 columns and 576 rows, resulting in an active area of $21 \times 10.6 \text{ mm}^2$ [99]. The size of a pixel is $18.4 \times 18.4 \mu\text{m}^2$ and a track position reconstruction of $2 \mu\text{m}$ is reached using the pixel cluster.

The complete sensor is read out in a column-parallel mode with a pixel readout frequency of 80 MHz. A so called “EUDET Data Reduction Board” (EUDRB) was used to read out the MIMOSA sensor [100]. These boards are controlled by FPGAs and perform a correlated double sampling¹⁴, pedestal subtraction and zero suppression¹⁵. All in all 6 EUDRBs are needed to read-out all MIMOSA sensors. The data of each EUDRB is transferred to a VME computer via VME bus. The MIMOSA-26 data is purely binary and saved in a raw format together with the trigger number.

¹³Minimum Ionizing MOS Active Pixel Sensor.

¹⁴The application avoids double counting of signals as explained in [98].

¹⁵A data reduction is achieved by removing pixels with no (zero) signals.

5.3 Setup of the Device Under Test

The DUT was in a shielding box placed between the two telescope arms as shown in Figure 62.

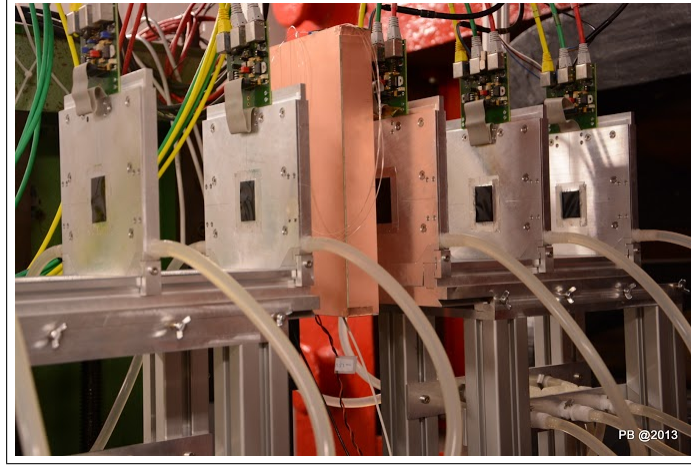
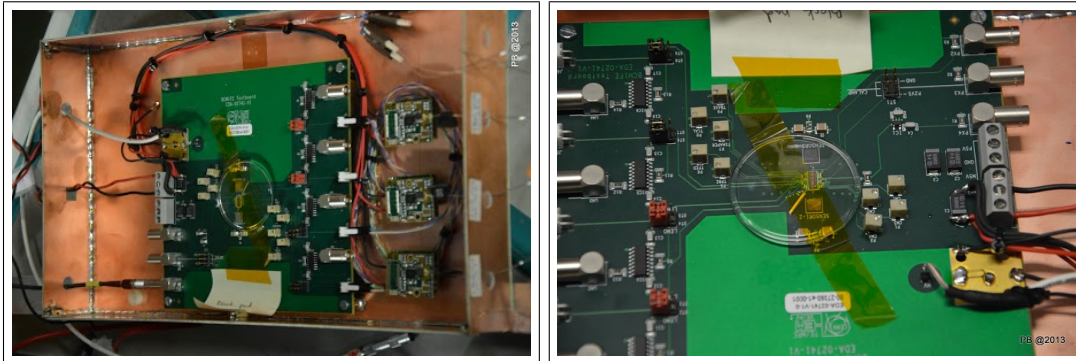


Figure 62: The DUT box, containing the BCM1F prototype, placed between the two telescope arms.

The BCM1F prototype was fabricated to quantify its performance with the new dedicated front-end ASIC and the readout of signals from a two pad sensors. The complete prototype is shown in Figure 63. It holds two sCVD sensors and the upgraded front-end ASIC for signal amplification. In addition, three opto-hybrids are connected to the differential signal output of the ASIC for transmitting the sensor signal to the back-end via an optical fibre.



(a) Front-end parts of the BCM1F prototype including diamond sensors, front-end ASIC and opto-hybrid. (b) Diamond sensors glued on the PCB under a plastic magnifier to protect the bonds to the ASIC.

Figure 63: Pictures of the BCM1F prototype used for the test-beam.

One sensor with a single pad metallization is mounted on the PCB as a reference sensor and a second sensor with a double pad metallization is mounted for testing the upgraded readout chain with two channels per sensor. The front-end ASIC holds four input channels. The pad of the one pad sensor and each of two pad sensor are connected via bonds to one input channel of the front-end ASIC. One input channel is left open to use it later for calibration. The front-end ASIC converts the sensor signal into an output voltage by a gain factor of 50 mV/fC . More details on the ASIC and opto-hybrids are given in Chapter 3.1 and 3.2. Each amplified signal is transmitted to

one of the three opto-hybrids. Figure 64 shows the four front-end ASIC output connectors and the three opto-hybrids with their corresponding optical fibres. The optical fibres are merged together in a 12-fiber ribbon cable that is connected to the standard analog optical receiver used by the CMS tracker allowing the conversion from optical signals to electrical signals. All three electrical signals are fed into the sampling ADC v1721, the same as used for the BCM1F signal processing as explained in Chapter 3.3. The readout of the ADC is triggered by the trigger signal coming from the v1495 unit. Data of the ADC is transmitted to the DUT computer where it is saved together with the trigger number in a root format [101].

The complete readout chain of the BCM1F prototype is done in the same way as designed for BCM1F to be installed in CMS.

Table 8 lists the diamond sensor pads with their corresponding front-end ASIC channel as well as the opto-hybrid number and ADC channel number. The ADC channel number is used to label the read out pads of the diamond sensors in the test-beam analysis.

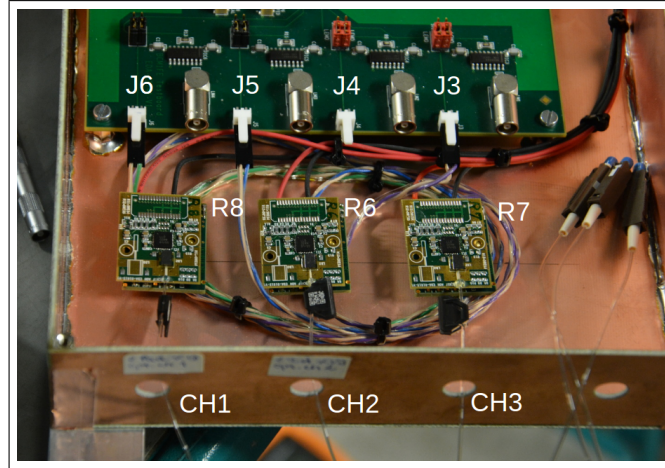


Figure 64: Each sensor pad is connected to the ASIC having a differential outputs labeled with J6, J5 and J3. The differential signal of each ASIC is fed into an opto-hybrid labeled with R8, R6 and R7. The optical signals from each sensor pad are called CH1, CH2 and CH3 corresponding to the ASIC and opto-hybrid. The optical fibres are fed through the holes of the DUT box.

Diamond Sensor	Channel Number of Front-End ASIC	Channel Number of Opto-Hybrid	Channel Number of ADC
One Pad	J3	R7	CH3
Free	J4	none	none
Two Pad Upper	J5	R6	CH2
Two Pad Lower	J6	R8	CH1

Table 8: Front-end ASIC, opto-hybrid and ADC channel numbers used for the DUT test-beam board.

5.4 Test-Beam Offline Analysis

The offline data analysis is based on combining for each trigger the telescope track information with the ADC file and its signal shape information. In order to identify the sensor signal to

the corresponding telescope track, the trigger number is used. Each trigger coming from the scintillators increases the trigger number consecutively in each ADC and telescope file. If two tracks passing simultaneously, the complete event is ignored. An unique correspondence between ADC signal and reconstructed telescope track is therefore given.

5.4.1 Track Reconstruction

The telescope analysis software contains six processors that are executed one after the other as listed:

1. Converter
2. Clustering
3. Filter
4. Hitmaker
5. Alignment
6. Fitter

All processors are developed within the EUDET pixel telescope data-acquisition software (EUDAQ) described in Reference [102]. First of all the telescope raw data files are converted into lcio¹⁶ format with the **Converter**.

The calculation of the track impact position in each sensor plane starts by searching hit pixels that are grouped into clusters. This step is done by the **Clustering** processor. A special algorithm is used in order to identify a cluster. First, for all hit pixel the number N of neighboring hit pixel is determined but ignoring the diagonal neighbors. Second, the hit pixels from one group are sorted by the number N of neighbors whereas the seed candidate is the pixel with the greatest N . The diagonal neighbors are counted in the case seed candidates have equal N and the seed candidate with a larger number of diagonal neighbors is preferred. After finding the seed candidate, all hit pixels in a fixed 3×3 frame around the seed candidate are grouped as a cluster. The information of hit pixels in a cluster is stored. If for 200 triggered events the same pixels are fired in 15% of the events these pixels are marked as noisy.

In addition, it is possible to reject certain clusters by setting criteria at a **Filter**. Such a criterion can for example remove all clusters that do not have a total charge of a certain value [103]. However, the filter processor is disabled by default and is not used in this offline analysis.

The purpose of the **Hitmaker** processor is to calculate the cluster center by using the pixel signal weighted average position with the center of gravity method¹⁷. After finding the center of the cluster in pixel units (column and row numbers), the conversion to a space point needs to be done by using a so called “Gear” file. This file contains the geometrical information of each sensor plane and pixels in x-, y- and z-direction. X- and y-coordinates can be extracted from the information about the sensor geometry that is given by the EUDET telescope itself (see Chapter 5.2) as illustrated in Figure 65.

¹⁶The lcio format is originating from the linear collider community since another main objectives of the EUDET telescope project is the development of a common software framework together with the experiments at the International Linear Collider

¹⁷The spacepoint is calculated as the average from the coordinate of adjacent pixels, weighted with the signal size.

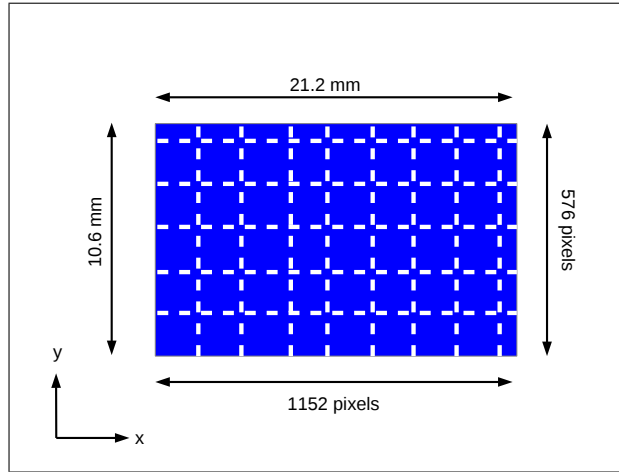


Figure 65: Geometry of Mimosa-26 sensors and numbers of pixels in x- and y- direction.

The z-coordinate depends on the actual setup and is defined by the user who places the telescope planes. Figure 66 shows the setting used for the BCM1F test-beam containing the z-coordinates. The position of the DUT between the two telescope arms defines the zero point on the z-axis whereas the right telescope arm is at negative z values.

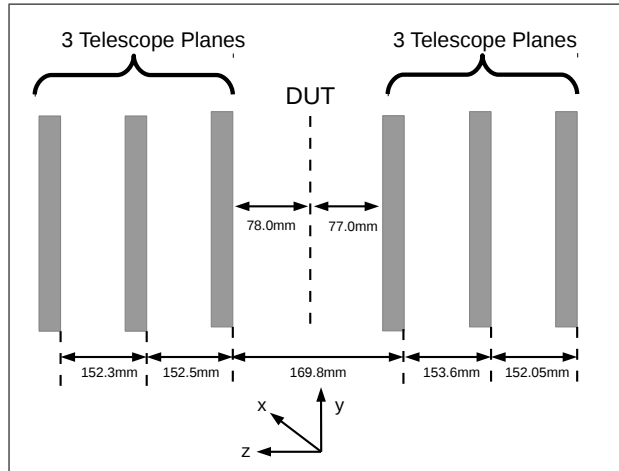


Figure 66: Beam telescope geometry for the alignment run. The DUT was removed from the setup.

In order to correct the space points for shifts in x-, y- or z-direction and rotations Θ_x , Θ_y or Θ_z around these axes, an alignment is required and so called “alignment constants” need to be determined and applied to the space points. The alignment constant is determined by processing the **Converter**, **Clustering**, **Filter**, **Hitmaker** and **Alignment** on an alignment data file. For all other files the **Alignment** processor is not required since **Hitmaker** takes the calculated alignment constants from the pre-processed alignment file.

The alignment data file is obtained by moving the DUT out of the beam and taking data only with all 6 telescope planes as shown in Figure 66. The track reconstruction is then performed by using an analytical track-finding approach as described in Reference [104]. The algorithm takes into account the multiple scattering of particles in the detector material and is based on the following assumptions:

- all telescope planes are parallel to each other
- the incoming beam is perpendicular to the telescope planes
- the incoming beam has a small angular spread
- particle energy losses in the telescope planes are negligible
- thickness of material layers are small compared to the distance between the planes

The tracks are reconstructed by minimising a χ^2 function and can be considered separately for the horizontal and vertical plane. The contribution in the y-axis on plane i to χ^2 is given by:

$$\Delta\chi_i^2 = \left(\frac{y_i - p_i}{\sigma_i}\right)^2 + \left(\frac{\Theta_i - \Theta_{i-1}}{\Delta\Theta_i}\right)^2, \quad (5.1)$$

where p_i is the determined track position and y_i the measured particle position in each plane i . The determined track position for one out of the six telescope planes is received by a linear combination of the remaining five telescope planes. The mean value of the difference of the determined and measured track position peaks in the ideal case at zero. The variance of its distribution is called the residual and corresponds to the precision of the track reconstruction. The angles Θ_{i-1} and Θ_i are the angles between the direction perpendicular to the telescope planes and the track direction as illustrated in Figure 67. The quantity $\Delta\Theta_i$ is the expected width of the scattering angle distribution and defined by the ‘‘Gear’’ file. σ_i is the resolution of the position measurement. A detailed explanation of the track fitting is given in Reference [104].

The determined track positions are then used to obtain the alignment constants being a shift in the x- or y-axis applied to minimize the χ^2 function for all telescope planes. The alignment constants are taken by **Fitter**.

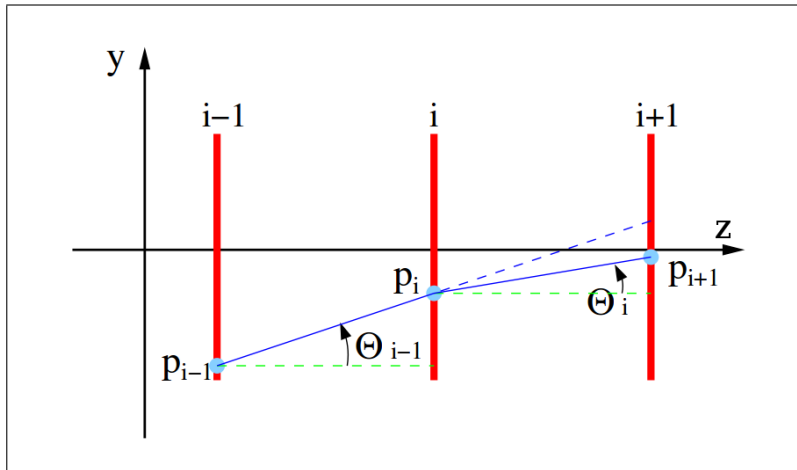


Figure 67: Illustration of variables used for the track reconstruction algorithm.

The **Fitter** fits the track position in each telescope plane when the DUT is installed with the same algorithm as the **Alignment** processor. However, the **Fitter** takes only three planes, the left or the right telescope arm, for the track determination.

A C++ program takes the fitted space points of the telescope planes and fits a straight trajectory

for the left and right arm as illustrated in Figure 68. The crossing point of both trajectories is then defined as the impact position of the beam particle on the DUT.

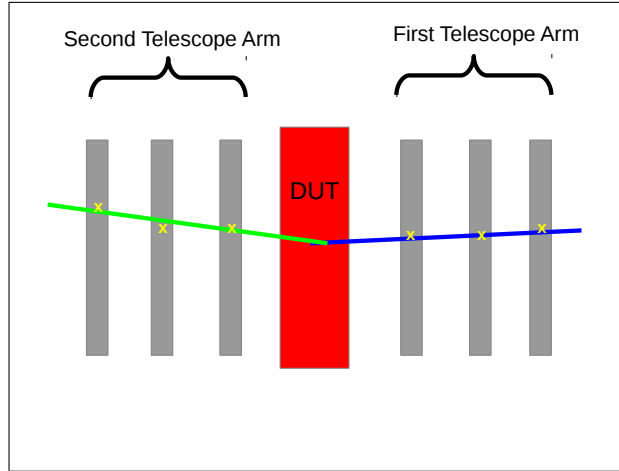


Figure 68: Telescope tracks of the first (blue) and second (green) telescope arm are fitted by a linear particle trajectory. The crossing point of both at the DUT corresponds to the particle impact position.

5.4.2 Data Structure and Statistics

The previously mentioned C++ program from the telescope extracts the following information from the telescope files that are required to perform the full test-beam analysis:

- trigger number
- telescope event number
- impact position on the DUT on the x- and y-axes
- angle between the two fitted particle tracks on the x- and y-axes,

whereas the trigger number is generated by the TLU and enumerating all incoming triggers. The telescope event number is increased by each reconstructed particle track in the fitter.

In order to ensure a unique correspondence between signal in the DUT and particle impact position, the C++ program rejects all telescope events with the same trigger number in the case more than one exists. These are events triggering one readout but producing more than one fitted particle track in one of the telescope arms and are caused by more than one simultaneously crossing particles. Then it is guaranteed that the signal produced in the DUT is caused only by one beam particle. Figure 69 shows the number of reconstructed particle tracks from the alignment run for 113242 triggers. Only 10% of the triggered telescope data is rejected due to multiple track reconstruction. At the end a root file is generated with the above listed informations.

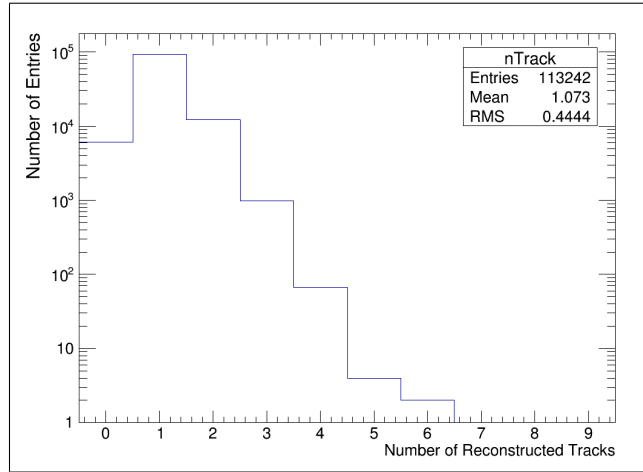


Figure 69: Number of reconstructed tracks for all triggered telescope events.

The ADC data is already saved in a root format and contains the following information:

- trigger number
- ADC event number
- sampled DUT signal,

whereas the trigger number and ADC event number are consecutively increased with each incoming trigger. ADC events that are traced back to two fitted particle tracks are rejected as well. A sampled DUT signal is illustrated in Figure 70.

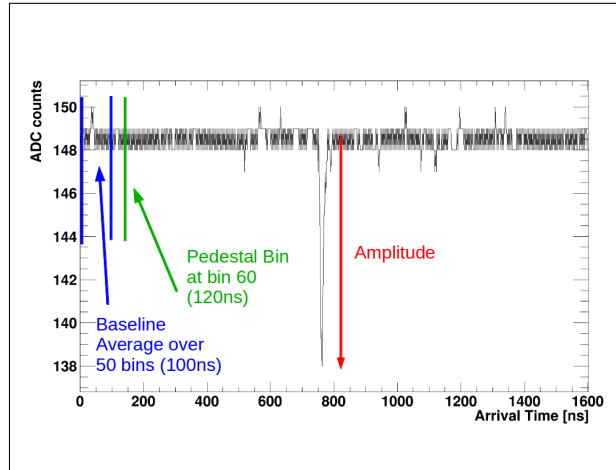


Figure 70: Sampled DUT signal as a function of time. The baseline is calculated by taking the very first 50 bins (100 ns) and the signal amplitude is extracted for the test-beam analysis.

The ADC analysis calculates first the baseline by averaging the first N_B ADC samples:

$$Baseline = \frac{\sum_{i=0}^{i=N_B} S_i}{N_B} \quad (5.2)$$

where S_i are the ADC samples used for the calculation of the baseline. N_B is set to 50 bins. The value of bin number 60, corresponding to a time of 120 ns, is called S_P and used to calculate the pedestal value. It is defined by

$$Pedestal = S_P - Baseline . \quad (5.3)$$

The pedestal position is chosen such that no signal is expected at this time. A pedestal value is obtained from each DUT signal resulting in a pedestal distribution. The variance of the pedestal distribution, $\sigma_{Pedestal}$, is defined by

$$\sigma_{Pedestal} = \sqrt{\frac{1}{N_P} \sum_{N_P} (Pedestal - \mu_P)^2} \quad (5.4)$$

$$(5.5)$$

where μ_P is the average value of the pedestal, N_P the number of DUT signals where the pedestal is obtained:

$$\mu_P = \frac{1}{N_P} \sum_{N_P} Pedestal . \quad (5.6)$$

The signal size is also taken from the ADC file by looking for the minimum ADC value over the whole ADC samples and defined by:

$$Signal\ Amplitude = Minimum\ ADC\ Value - Baseline . \quad (5.7)$$

The signal amplitude is used in the test-beam analysis to extract the relevant quantities discussed in Chapter 6.

Figure 71 shows the distribution of the particle impact positions on the first telescope in x- and y-direction. A flat beam particle density distribution is observed in the ranges from -6 mm to 4 mm in x-direction and from -4 mm to 3 mm in y-direction resulting in an area of 70 mm². This is slightly larger than the expected beam size of 64 mm². The sharp cuts at the edges of the distributions are due to the limits of the active telescope area of 21 × 10.6 mm².

Since the diamond metallization area is around 4 × 4 mm², only 20 % of the triggers are expected to contain a track hitting the sensitive sensor area. Another 10 % of these triggers are rejected due to multiple track reconstruction. Therefore, around 18 % of the triggers taken can be used for the test-beam analysis and the number of triggers was chosen such that the later analysis has a statistical precision better than 5 %. For this reason the number of triggers taken for the measurement of the charge collection efficiency as a function of the bias voltage was 150 k resulting in around 25 k particle crossings in the sensor. In addition, a high statistics trigger run with 4 million triggers was taken to analyse the sensor response as a function of the particle impact position on the diamond sensor with a minimum spatial resolution of 0.01 mm² and an expected statistical uncertainty of about 5 %.

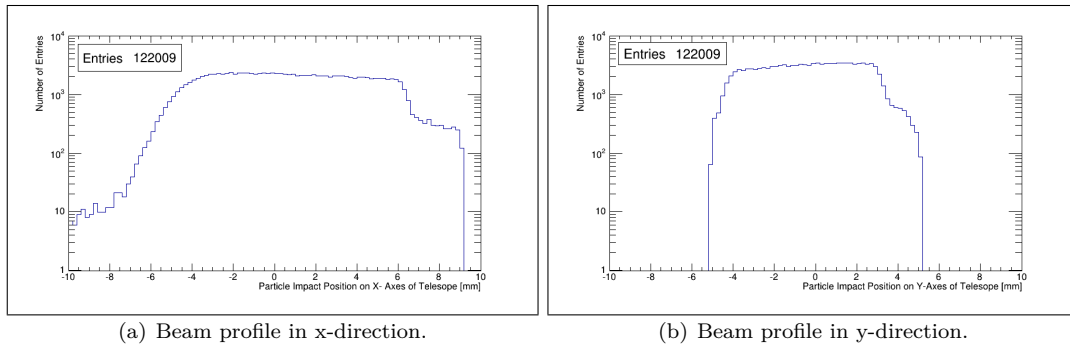


Figure 71: Distribution of the impact position of the beam particles in the first telescope plane (a) in the x-direction and (b) in the y-direction.

6 Results from the Test-Beam

Two different sCVD sensors were selected for installation at the DUT PCB on the basis of results from the characterization measurements in the laboratory as given in Section 4.4. One sensor was chosen with only one quadratic pad and the other one with two rectangular pads of equal size (see Figure 42). Four types of measurements were done to determine the amplifier performance and to characterize the sCVD sensor in detail:

- signal response as function of time
- CCE as a function of the bias voltage
- signal-to-noise ratio as a function of the bias voltage
- CCE as a function of the beam particle impact position.

Measurements of the signal shape allow the verification of the peaking time and FWHM of the amplifier output signal. The CCE as a function of bias voltage is compared to the laboratory measurements and ensures the proper functionality of the whole front-end part. In addition, the signal-to-noise ratio (S/N) is measured to characterize the analog readout. A CCE scan for different particle impact positions provides informations about the homogeneity of the signal response of the sensors and the signal sharing between the two readout channels of the two pad sensor.

6.1 Laboratory Measurements of Diamond Sensor Used for the DUT

Before placing the sensor on the DUT PCB, electrical characterizations in the laboratory of both sensors were done. Measurements of the leakage current as a function of the bias voltage and the CCE as a function of bias voltage were performed. Measurement results of the chosen diamond sensors are shown in Figure 72 for the one pad sensor and in Figure 73 for the two pad sensor.

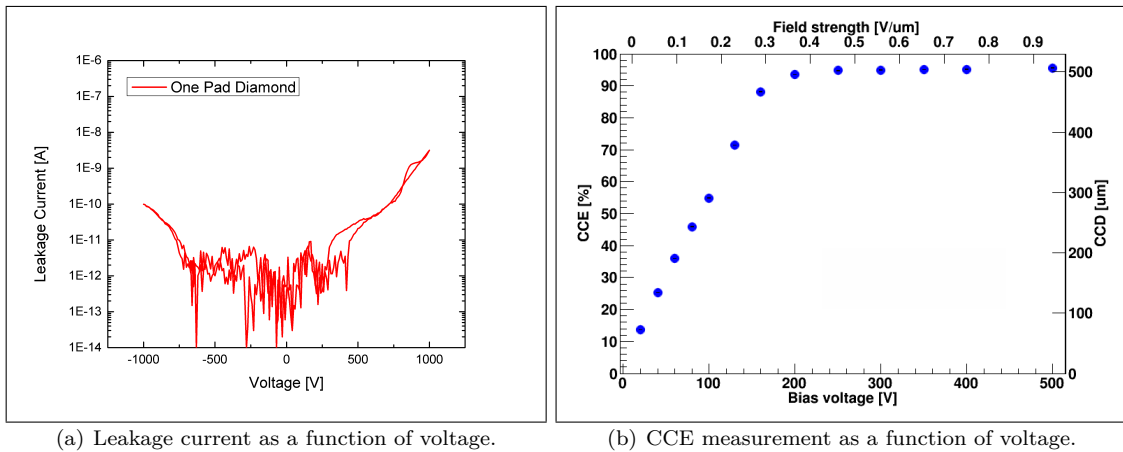


Figure 72: The leakage current and the CCE as a function of the bias voltage for the one pad sensor.

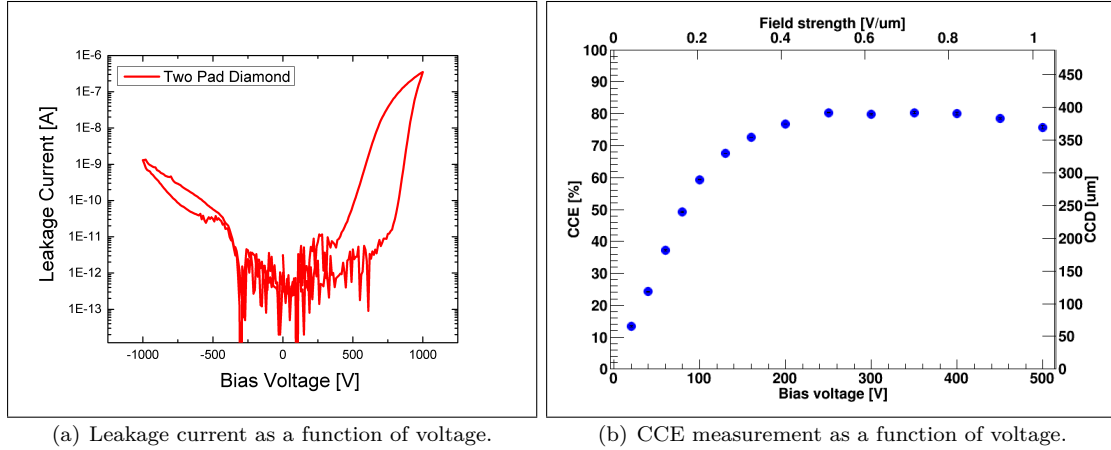


Figure 73: The leakage current and the CCE as a function of the bias voltage for the two pad sensor.

The one pad sensor shows a leakage current in the pA range for a negative polarity up to -1 kV and for the positive polarity up to nA at 1 kV. Therefore, a negative polarity was chosen for the CCE measurement. The CCE saturates at 150 V with a full charge collection efficiency of 95 %. A higher leakage current is observed for the two pad sensor reaching nA for a negative bias voltage of -1 kV and even a μA for 1 kV at the positive polarity. Therefore, the negative polarity was chosen for the CCE measurements. In order to perform the CCE measurement in the laboratory, both pads were connected with a bond and treated as a single pad. Results of the CCE measurement with negative polarity show a CCE saturation above 200 V and a CCE value of 80 %. This sensor was chosen from the at the time available five sensors with a two pad metallization being the one with the lowest leakage current and the best signal current stability.

The readout scheme of the sensor is shown in Figure 74. The bias voltage is applied on one side of the sensor and the front-end ASIC to the other side being grounded. Since the front-end ASIC is optimized for negative sensor signals, a negative bias voltage is applied to the sensors. Both selected sensors are glued on the PCB with the orientation determined from the leakage current measurement.

6.2 Calibration of the Setup

The front-end ASIC converts the induced sensor charge Q_{Signal} into an output voltage V_{Out} that is measured with an ADC and represented by the signal amplitude A with $Q_{Signal} \sim A$. A calibration factor k is needed to transform the ADC signal amplitude A into a measured charge:

$$Q_{Signal} = k \cdot A . \quad (6.1)$$

The CCE determined in the test-beam analysis is then extracted as described in Chapter 4.4.4 with the following formula:

$$CCE = \frac{Q_{Signal}}{Q_{Expected}} \quad (6.2)$$

$$CCE [\%] = \frac{A [ADC Ch] \cdot k [e/ADC Ch]}{36 [e/\mu m] \cdot d [\mu m]} \cdot 100, \quad (6.3)$$

where d is the sensor thickness. The calibration factor k in Formula 6.3 is determined by a separate calibration measurement. A calibration pulse ΔV_{Cal} is fed into the three used front-end ASIC channel by a capacitance C_x as shown in Figure 74. The signal is amplified in each channel, sent to the corresponding optical hybrid and digitized in the ADC.

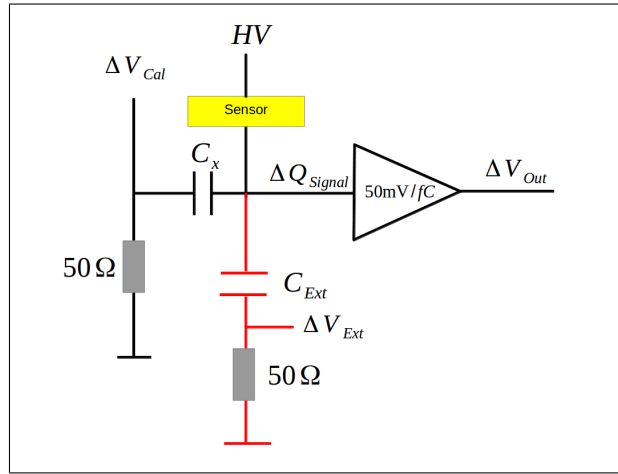


Figure 74: Schematic of the electronic circuit for the sCVD sensor calibration and measurements.

This can be done for different heights of the calibration pulse ΔV_{Cal} . Their corresponding digitized signal amplitude is shown in Figure 75 where the calibration factor is taken from the slope of the linear fit. However, the calibration factor k is in the unit of $ADC Channels/mV$ instead of $ADC Channels/e$ that is required for the CCE value.

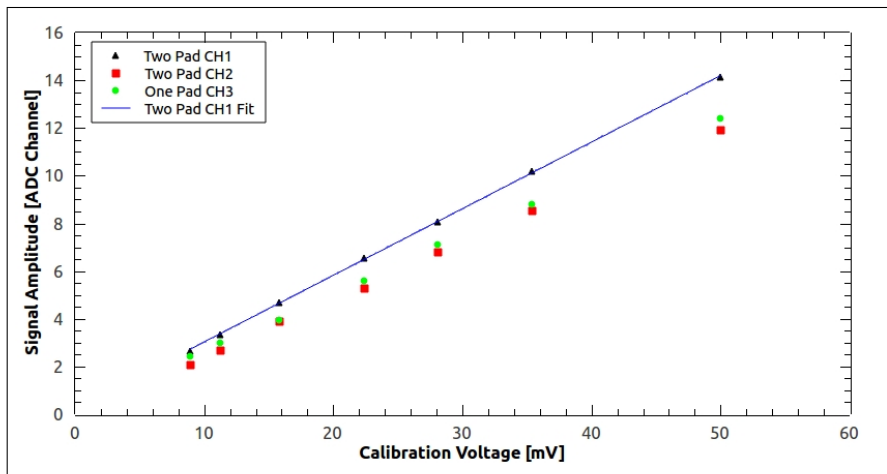


Figure 75: Signal amplitude measured with the ADC as a function of calibration pulse size ΔV_{Cal} . The calibration factor is illustrated by the slope of the linear fit as done for the two pad sensor CH1.

A conversion into a charge is done by using $Q_{Cal} = C_x \cdot \Delta V_{Cal}$ using the internal calibration capacitance C_x . C_x was determined in an additional measurement by connecting a capacitance C_{ext} of 1 pF with an uncertainty of $\Delta C_{ext} \leq 1\%$ to the fourth free input channel of the front-end ASIC as illustrated with the red electronic circuit schematic in Figure 74.

Table 9 lists the resulting calibration factor k for all three test-beam channels. The differences in the calibration factors are caused by the differences of the performance of the used opto-hybrids and the different input capacitances caused by the one and two pad metallization. Additionally, the thickness of both sensors is listed that is needed to calculate the CCE with Formula 6.3.

Diamond Sensor	ADC Channel Number	Sensor Thickness [μm]	Calibration Factor k [e/ADC counts]
One Pad	CH3	530	1795.7
Two Pad	CH2	488	2004.9
Two Pad	CH1	488	1692.8

Table 9: Calibration factor k and sensor thickness of each sensor pad connected to the front-end ASIC.

6.3 Signal Shape and Impact Position

One of the first test-beam measurements was to record sensor signals with the ADC originating from one electron crossing one of the three pads. It allows a first check that the readout chain is working as expected and that a clear sensor signal can be observed.

Figure 76 shows a signal coming from the one pad sensor biased with 500 V and measured with the sampling ADC.

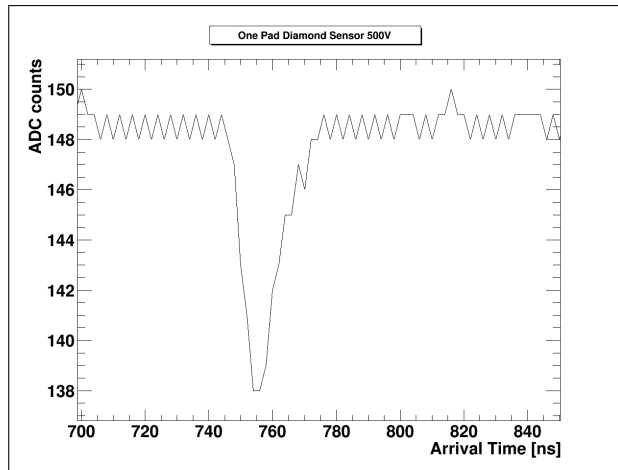


Figure 76: Signal shape of the one pad sensor as a function of time measured during the test-beam. The signal corresponds to one crossing electron.

The baseline is at around 148.5 ADC counts and the sensor signal starts to rise at an arrival time of around 740 ns with respect to the trigger. A FWHM of less than 10 ns is observed that corresponds to the specification of the front-end ASIC given in Chapter 3.2. The signal amplitude is about 10.5 ADC counts corresponding to 98% CCE using the calibration factor from Table 9 and Formula 6.3 with a sensor thickness of 530 μm .

Similar results are received from the two pad sensor as shown in Figure 77. A bias voltage of

500 V was used as for the two pad sensor. The baseline is at around 145 ADC counts for CH1 and 149.5 ADC counts for CH2. Since the baseline is defined by the optical receiver, it is different for each channel. A signal amplitude of 8 ADC counts for CH1 is observed that corresponds to 80 % of CCE. CH2 shows a signal amplitude of 7.5 ADC counts corresponding to 80 % CCE. Again the FWHM for CH1 and CH2 is less than 10 ns.

All three channels show a clear signal with low electronic noise. This measurement of the signal shapes verifies the specifications of the upgraded front-end ASIC given in Chapter 3.1.

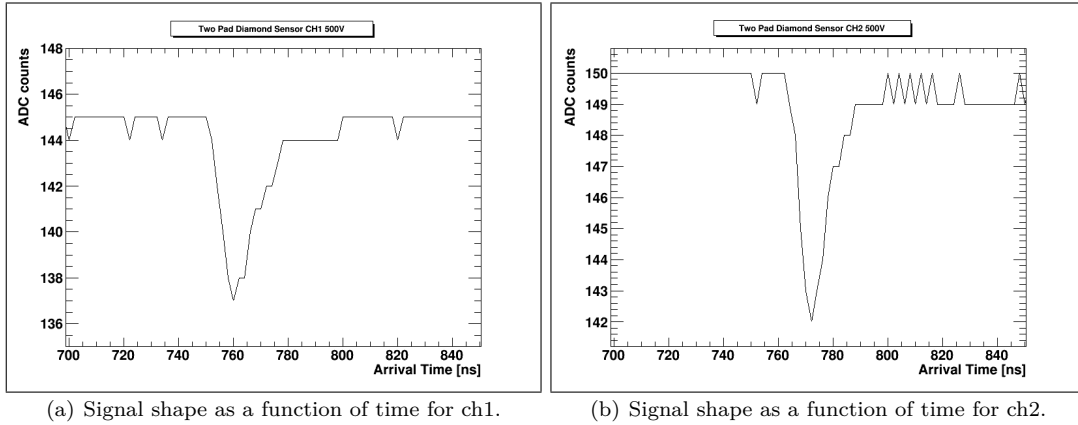


Figure 77: Signal shapes of the two pad sensor as a function of time measured in the test-beam. The signal corresponds to one crossing electron.

In the following analysis only events with signals in the one pad sensor larger than 90 % CCE are used. For these events the distribution of the particle impact position at the sensor is shown in Figure 78(a). In the middle of the sensor a circle of smaller particle density is visible. The PCB has a metallic ring with a hole under the sensor center connecting the bias voltage to the sensor metallization. The multiple scattering angle at the metallic ring is larger and since events with a larger scattering angle are rejected for this analysis the ring is mapped on the sensor. The sensor size of $4.6 \times 4.6 \text{ mm}^2$ (x-coordinates from -4.2 mm to 0.4 mm and y-coordinates from -3.2 mm to 1.4 mm) is clearly visible in the histogram. Agreement with the measurements of the optical inspection is achieved as illustrated in Figure 78(b). The optical inspection shows a sensor size of $4.6 \times 4.6 \text{ mm}^2$ and a metallization area of around $4 \times 4 \text{ mm}^2$ with a metallization of Cr/Au for the bond contact. A small bond on the right of the metallization is also present that connects the pad with the front-end ASIC. Scratches on the metallization surface are visible due to the frequent use of this sensor for different measurements before it was installed into the test-beam box.

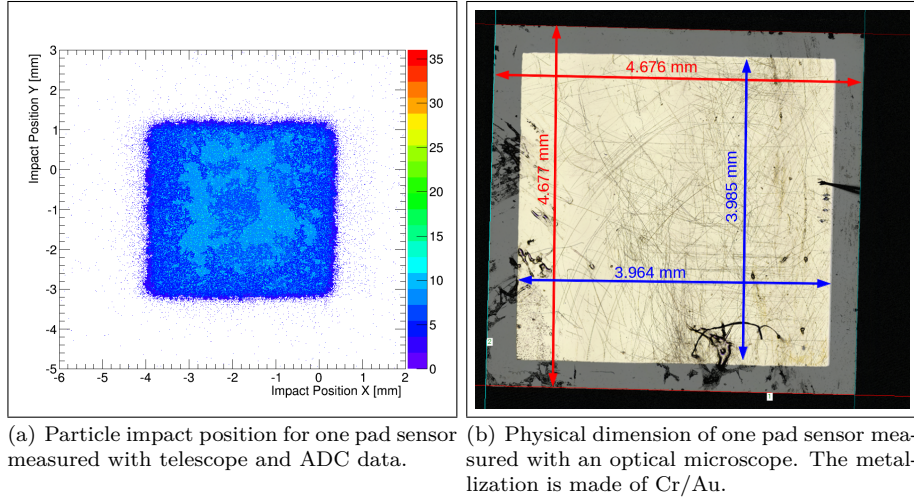


Figure 78: Geometry of one pad sensor measured with test-beam data and optical microscope.

The same measurement is done for the two pad sensor, separately for CH1 and CH2, but only for signals having more than 75 % CCE. After receiving a 2D histograms of CH1 and CH2, both histograms are merged together. Figure 79(a) shows the results of this analysis. A sensor size of $4.6 \times 4.6 \text{ mm}^2$ (x-coordinates from -3.2 mm to 1.4 mm and y-coordinates from -3.4 mm to 1.2 mm) is observed. Again a projection of the metallic ring and the hole at the PCB under the sensor is visible. In addition, the gap between the two metallizations at the y-coordinate -1 mm with a width of a around 0.2 mm visible. However, the optical measurement in Figure 79(b) shows a distance between the metallizations of $5 \mu\text{m}$. An explanation of this observation is given in Chapter 6.6. The lower pad represents the readout of CH1.

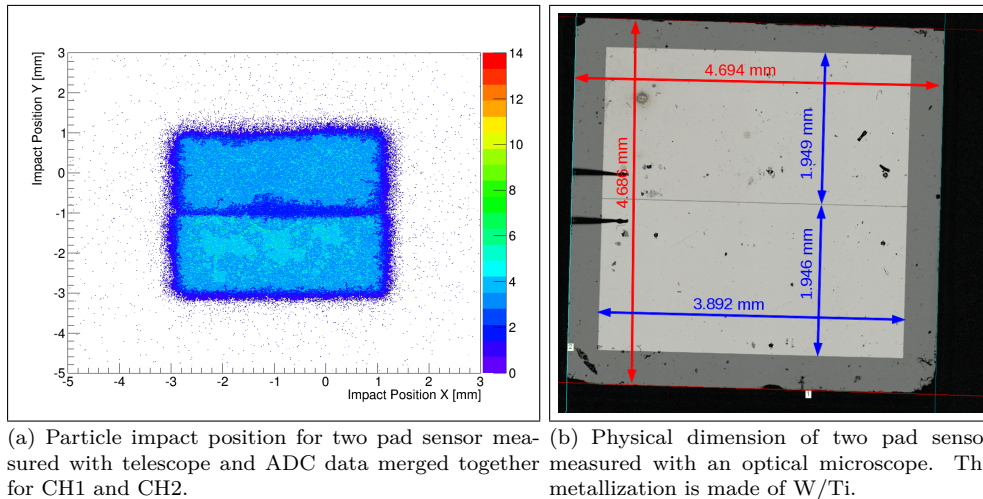


Figure 79: Geometry of two pad sensor measured with test-beam data and optical microscope.

The light blue area covers a range from -3 mm to -1 mm on the y-axis and from -2.8 mm to 1.2 mm on the x-axis. The upper pad is CH2 with a light blue area from -1 mm to 1 mm on the y-axis and again from -2.8 mm to 1.2 mm on the x-axis. The light blue area with a higher particle density

corresponds to the metallization area as visible in Figure 79(b) and determined to be $2 \times 3.9 \text{ mm}^2$. The complete sensor size is estimated to be $4.6 \times 4.6 \text{ mm}^2$ and the metallization area for one pad $3.9 \times 1.9 \text{ mm}^2$. Two bonds are visible on the left side of each metallization pad for reading out both channels independently.

6.4 Charge Collection Efficiency as a Function of Bias Voltage

A spectrum of signal amplitudes is used to calculate the CCE for different bias voltages. All signal amplitudes are plotted in a histogram originating from particles having impact point within the metallization area taken from Figure 78(a). An amplitude spectrum for the one pad sensor with a bias voltage of 500 V is shown in Figure 80. It shows a Landau-like distribution as given in Chapter 4.3. A pedestal is not visible since only triggers of beam particles crossing the sensor are selected for these histograms. A fit with a Landau distribution convoluted with a Gaussian is performed. The MPV of the Landau contribution is taken for the CCE calculation. It is at around 11 ADC counts for a bias voltage of 500 V that corresponds to 98 % CCE.

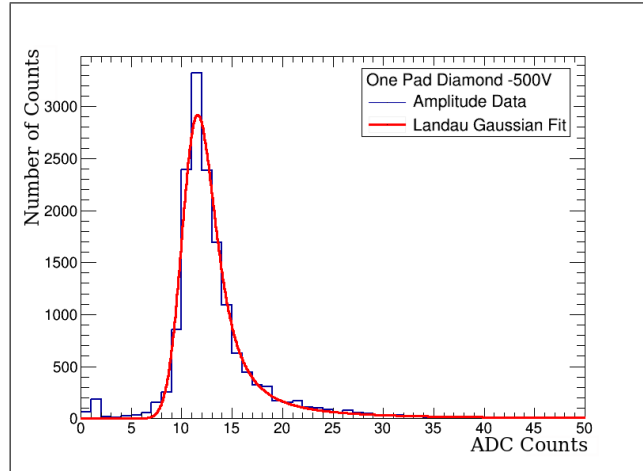


Figure 80: Amplitude spectrum for the one pad sensor measured with a negative bias voltage of 500 V.

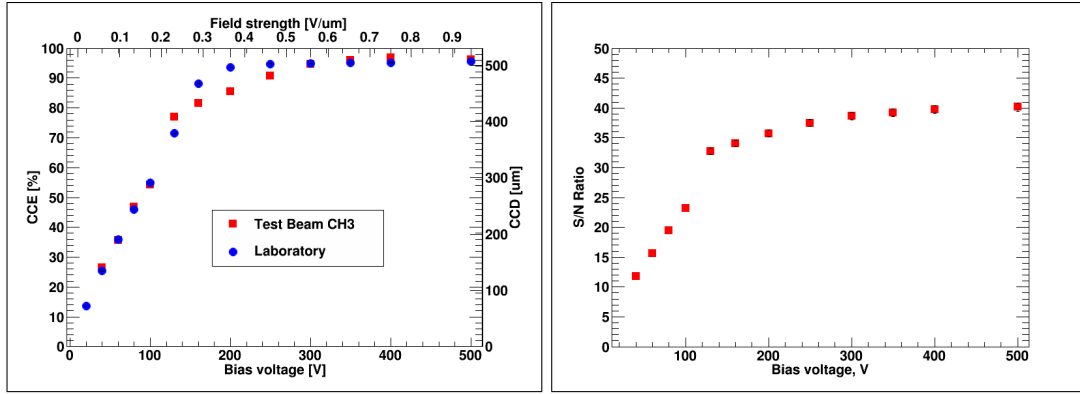
The CCE as a function of bias voltage is shown in Figure 83(a). It shows the CCE measured at the test-beam together with the measurement from the laboratory. The test-beam results match the laboratory results up to 100 V. A step at 130 V is visible in the test-beam measurement. Just before this measurement the beam was switched off for machine development for around half a day. During that time the bias voltage was also switched off in order to perform a calibration run and was ramped up to 130 V again when the beam was back. During the interruption apparently the conditions in the sensor changed. Above 300 V the measurement in the test-beam match again the one measured in the laboratory.

A S/N ratio is calculated as

$$S/N = \frac{\text{Signal Amplitude}}{\sigma_{\text{Pedestal}}}, \quad (6.4)$$

where the signal amplitude depends on the bias voltage. Figure 81(b) shows the S/N that is around

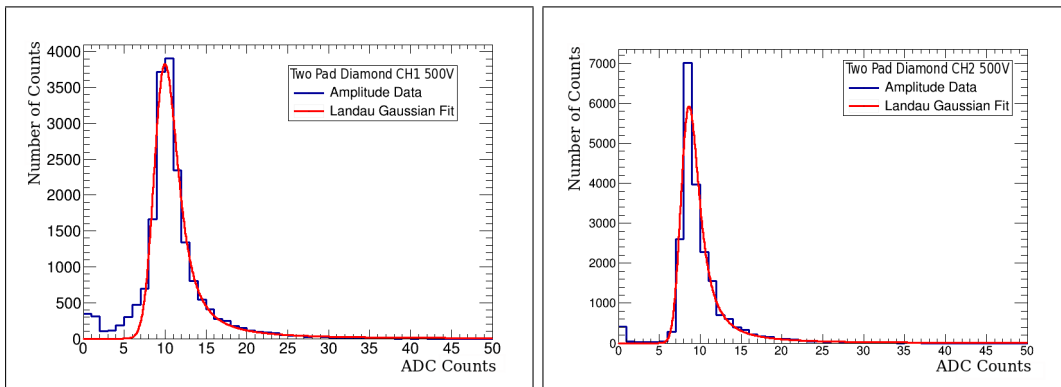
40 above 250 V where the saturation of the CCE starts. The step at 130 V is again visible resulting from the absence of the beam. The S/N ratio as a function of the bias voltage has as expected a similar shape as the CCE as a function of bias voltage.



(a) CCE of the one pad sensor as a function of bias voltage. (b) S/N of the one pad sensor as a function of bias voltage.

Figure 81: CCE Scan and S/N as a function of bias voltage of the one pad sensor measured during the test-beam.

The same measurement is also done for the two pad sensor for both readout channels separately. An amplitude spectrum for both channels was taken only from beam particles crossing within the metallization area of the sensor. Figure 82(a) and Figure 82(b) show the amplitude spectra for CH1 and CH2 at a bias voltage of 500 V respectively. The spectrum is again fitted with a Landau distribution convoluted with a Gaussian. The MPV of CH1 is at 9.5 ADC counts corresponding to 90 % CCE. The fitted amplitude spectrum of CH2 has its MPV at 8.5 ADC counts that corresponds to 93 % CCE.



(a) Amplitude spectrum of two pad sensor from ch1. (b) Amplitude spectrum of two pad sensor from ch2.

Figure 82: Amplitude spectra for the two pad sensor as a function of bias voltage measured with a negative bias voltage of 500 V.

Figure 83(a) shows the CCE as a function of the bias voltage for CH1 and CH2 in comparison to the laboratory measurement. Firstly, the CCE values measured in the laboratory are lower than the CCE values taken from the test-beam analysis for CH1 and CH2. Secondly, CH1 and CH2 do

not have the same CCE values as expected. CH1 has an increase of CCE up to 200 V and reaches a saturation of 92 %. A smaller CCE is observed for CH2 that is increasing up to 200 V and has a maximum of 87 % CCE. The S/N follows the CCE curve and is around 30 above 200 V. A smaller S/N ratio of the two pad sensor compared to the one pad sensor is due to the reduced CCE as illustrated in Figure 73.

In order to understand the discrepancy between laboratory and test-beam measurement and the difference of CCE values for CH1 and CH2, a more detailed CCE analysis is done.

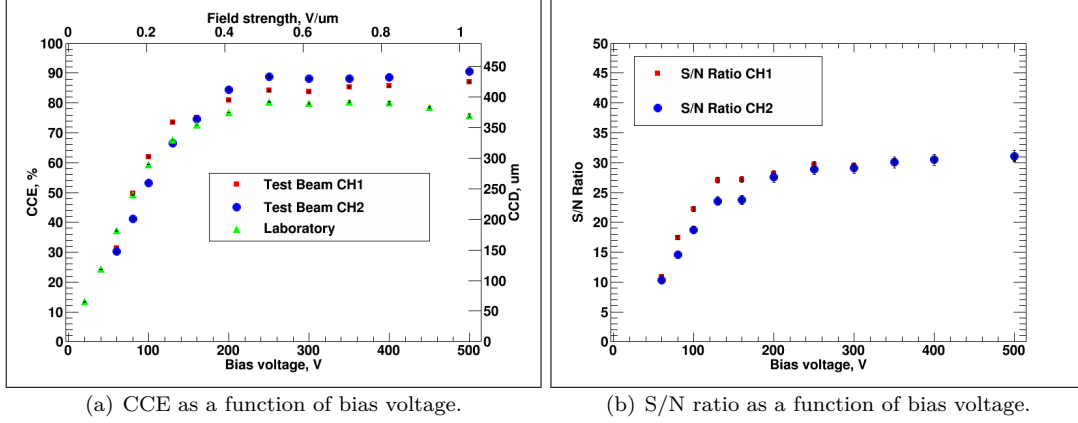


Figure 83: CCE and S/N ratio as a function of the bias voltage for the two pad sensor sensor measured during the test-beam.

The CCE measurement for each bias voltage is done by taking three data files with 100.000 triggers and each data file is taken over a time periode of around 1.500 s. This allows an analysis of the time dependence of the CCE values of CH1 and CH2 at a certain bias voltage. Table 10 lists the CCE values for a bias voltage of 130 V for CH1 and CH2 for the three data files taken at 0 s, 1.426 s and 3.956 s. A decrease of up to 4 % of the CCE as a function of time for both channels is observed. In addition, the absolute difference between the CCE of CH1 and CH2 is also decreasing. The same effect is observed for a bias voltage of 300 V as listed in Table 11 and at 500 V listed in Table 12. However, the decrease is not as strong for higher bias voltages. Again the absolute difference between both channels is as well decreasing for 300 V and 500 V.

The strong time dependence for a smaller bias voltage is explained by trapping. The drift velocity of a charge carrier depends on the applied electric field:

$$v(E) = v_{sat} \frac{E/E_c}{\left(1 + (E/E_c)^\beta\right)^{1/\beta}}, \quad (6.5)$$

where v_{sat} is the saturation drift velocity and E_c and β are fit parameters [105]. The values of v_{sat} , E_c and β are determined in Reference [106]. The effective drift mobility is obtained by the first derivative of Equation 6.5:

$$\mu(E) = \frac{\mu_0}{\left(1 + (E/E_c)^\beta\right)^{1/\beta}}, \quad (6.6)$$

where μ_0 is the zero field mobility. The drift length of a charge carrier is proportional to its mobility in the presence of material defects as given in Chapter 4.3.2. Therefore, the drift length of a charge carrier is smaller at lower bias voltages and trapping becomes more likely. In addition, the higher CCE values for the test beam are as well explained by trapping. The number of trapped charge depends on the rate of impinging particles. Reference [107] shows that the CCE decreases faster with a higher particle rate. The higher amount of produced electron hole pairs per time interval leads to a faster trapping and filling of traps. A crossing particle rate during the test beam is in the order of 32 electrons/s/cm² and in the laboratory in the order of 400.000 electrons/s/cm². In the laboratory all available traps are immediately filled causing a prompt counteracting electrical field due to the 12.500 times higher particle rate.

Time [s]	CCE CH1 [%]	CCE CH2 [%]	$ CCE\ CH1 - CCE\ CH2 $ [%]
0	81,4055	71,2570	10,1485
1.426	79,4851	69,7540	9,7311
3.956	77,425	68,7794	8,6456

Table 10: Decrease of CCE for CH1 and CH2 of two pad sensor measured at 130 V

Time [s]	CCE CH1 [%]	CCE CH2 [%]	$ CCE\ CH1 - CCE\ CH2 $ [%]
0	87,6967	93,3877	5,6910
1.404	86,9258	92,5683	5,6424
2.865	87,0761	92,4576	5,3815

Table 11: Decrease of CCE for CH1 and CH2 of two pad sensor measured at 300 V

Time [s]	CCE CH1 [%]	CCE CH2 [%]	$ CCE\ CH1 - CCE\ CH2 $ [%]
0	87,6967	93,3877	5,6910
1.351	86,9258	92,5683	5,6424
2.865	87,0761	92,4576	5,3815

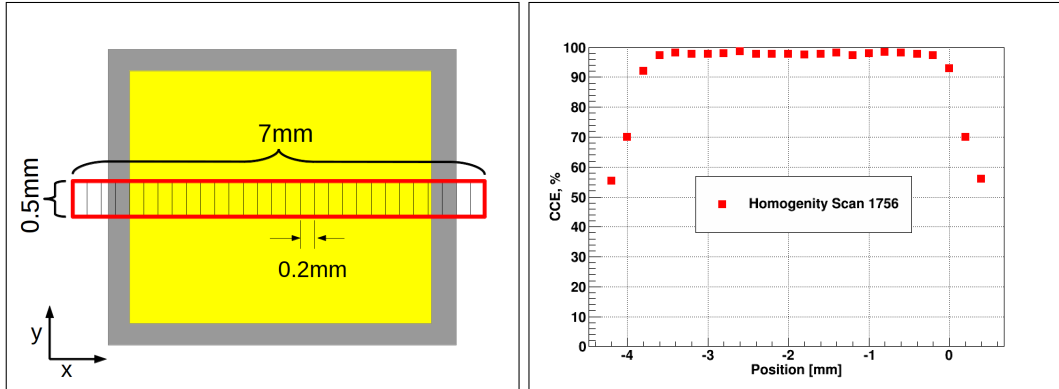
Table 12: Decrease of CCE for CH1 and CH2 of two pad sensor measured at 500 V

6.5 Charge Collection Efficiency as a Function of Beam Particle Impact Point on the Sensor

The CCE as a function of the beam particle impact position is studied at a bias voltage of 500 V for the one pad sensor and 350 V for the two pad sensor. This way the homogeneity of the signal response of the sCVD sensor is obtained and edge effects become visible.

In order to perform the analysis, an area of particle impact points is defined. All signals, originating from the crossed particle within a 7 mm long and 0.5 mm wide strip are used in this analysis. The strip was divided in 0.5 mm×0.2 mm pixels as shown in Figure 84(a) in order to measure the signal amplitude as a function of the x position. The strip length is larger than the physical sCVD sensor dimension to analyse the signal response at the sensor edge. A signal amplitude spectrum is taken and a CCE value is determined for each pixel. The result is given in Figure 84(b). A uniform CCE is measured from -3.6 mm to -0.8 mm with a value of 98 %. This is in agreement with the previous CCE measurement as a function of bias voltage (see Figure 81) at a bias voltage of 500 V.

A drop of the CCE is observed around the metallization edge. Note that the metallization area is around $3.9 \times 3.9 \text{ mm}^2$ and its position is determined to be from -3.8 mm to 0.0 mm on the x-axis but a drop of 98 % to 92 % of CCE is already visible from -3.6 mm and -0.2 mm . This edge effect is explained by the non-uniform electrical field already starting under the metallization as shown by simulations in Chapter 6.6. Outside of the metallization a drop of the CCE is expected again due to the non-homogeneous electrical field that leads to distorted signals and a reduced CCE as mentioned in [106, 108].



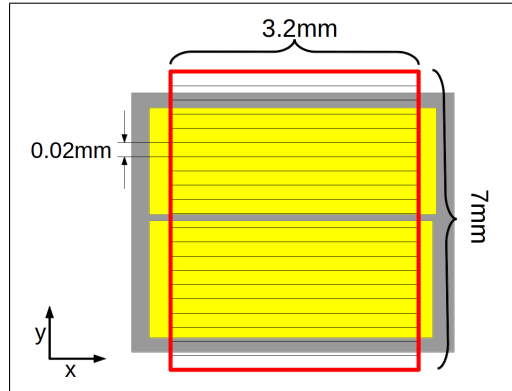
(a) A strip of 7 mm length, divided in $0.2 \text{ mm} \times 0.5 \text{ mm}$ large pixels, is used to perform the homogeneity analysis along the x-axis. (b) CCE as a function of pixel position showing a drop of CCE is visible at the edges of the metallization.

Figure 84: Study of the signal response as a function of the particle impact position for the one pad sensor.

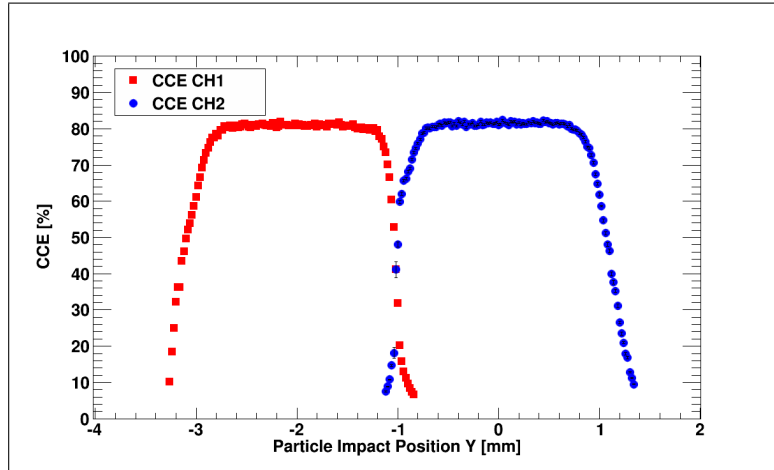
The settings for the analysis of the signal response as a function of the impact position for the two pad sensor are slightly different since the main goal of this measurement is to identify signal sharing between the two metallization pads. Therefore, an area of $3.2 \text{ mm} \times 7 \text{ mm}$ is chosen as shown in Figure 85(a). The area is then divided in $20 \mu\text{m}$ wide strips along the y-axis and their signal response is measured for CH1 and CH2. Each strip is only 3.2 mm long and therefore smaller than the metallization in order to obtain the full CCE by excluding edge effects. The results of both channels are given in Figure 85(b). A CCE plateau for both channels is visible with a maximum CCE value of 80 % with a bias voltage of 350 V. This CCE value is in agreement with the laboratory measurements as shown in Figure 73 since the measurement is performed for 24 h and a saturation of the CCE is reached.

Again the CCE drops around the boarder of the metallization at -2.8 mm and 0.8 mm and the metallization in y-direction is located from -3 mm and 1 mm . This observation is in agreement with the edge effects of the one pad sensor.

An additional drop of CCE is observed around the gap between the metallization pads that is extended over $400 \mu\text{m}$. However, the gap has a size of $5 \mu\text{m}$ and a drop of CCE is not expected over such a wide range for a perfect sCVD sensor. This effect is due to a CCE of 80 % only. A detailed explanation and simulation is given in Chapter 6.6.



(a) An area of $3.2 \times 7 \text{ mm}^2$ is divided in 0.02 mm wide strips to analyze the sensor signal response as a function of the y-coordinate.



(b) CCE as a function of the strip position on the y-axes for CH1 and CH2. A drop of CCE is visible at the edge of the metallization and at the metallization gap over a range of $400 \mu\text{m}$.

Figure 85: Response homogeneity study of the two pad sensor.

6.6 Simulations of Test-Beam Studies

In order to better understand the test-beam results simulations are performed. All simulations used for the test-beam study are done with a program called Superfish [109]. The program was developed in the Accelerator Group of Los Alamos and calculates a static electrical field in 2-D by feeding in the geometry and electrical settings of a sensor geometry. Afterwards a file is obtained with the 2-D coordinates x and y and the corresponding electrical field E_x and E_y , the square of the absolute value of the electrical field $|E|$ and the potential V . The electrical field is used to obtain the drift path of the generated charge carriers and the weighting potential for a certain electrode.

6.6.1 Simulation of Electrical Field at the Metallization Boarder

The electrical field defines the drift path of a charge carriers. In the case of a parallel plate geometry where both pads having the same length the electrical field lines are vertical to the metallization as illustrated in Figure 86. Therefore, it is expected that E_x is zero under the metallization area

and charge carriers travel perpendicular to the metallization.

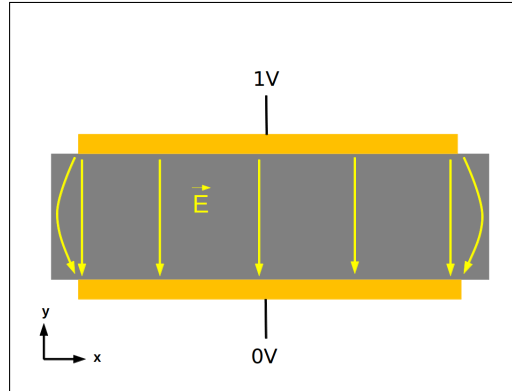
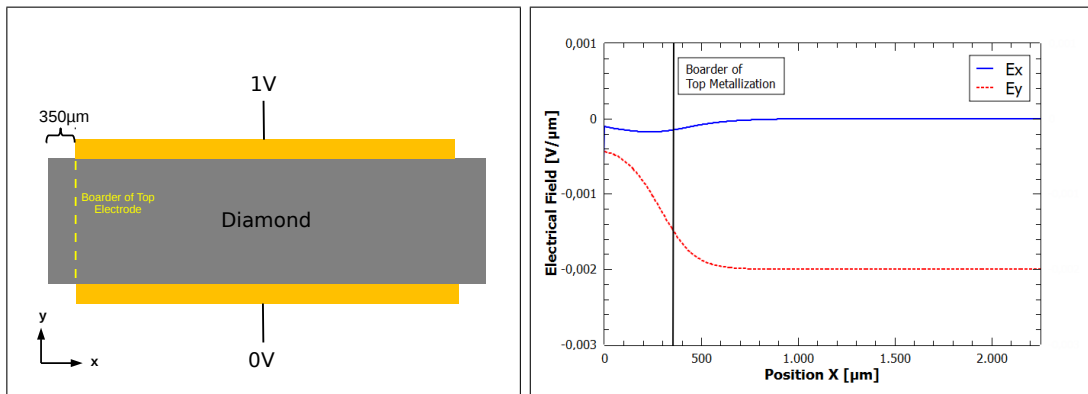


Figure 86: Illustration for the electrical field lines for parallel plate geometry. The field lines are vertical under and bended outside of the metallization pads.

In order to receive the strength of E_x and E_y in the middle of the sensor a Superfish simulation is performed with the settings shown in Figure 87(a). Both metallization pads have the same length and the distance between sensor boarder and the top and bottom metallization boarder is set to $350\ \mu\text{m}$, the same as determined with the optical microscope. The upper metallization pad is set to unit potential and the lower to zero potential.

Figure 87(b) shows the E_x and E_y components at a sensor depth of $250\ \mu\text{m}$ as a function of the x-coordinate. It is visible that E_x is almost zero under the metallization area and a charge carrier generated under the metallization moves perpendicular to the metallization under the influence of E_y . A small increase of E_y under the metallization pad at the boarder is visible, approaching then zero at the sensor boarder.



(a) Illustration of Superfish settings. The left sensor boarder corresponds to $x=0$. (b) Electrical field strength at the middle of the sensor as a function of the x-coordinate.

Figure 87: Superfish simulations for a parallel plate geometry with top and bottom pad having the same size.

Outside of the metallization the electrical field lines are bended and E_x is not zero and charge carriers are deflected by the influence of E_x . In addition, the E_y component shows a strong increase outside of the metallization area. Therefore, all charge carriers generated outside of the

metallization area have a longer traveling time resulting in distorted signals. This results in a measurable but reduced CCE outside of the metallization area. This Superfish simulation is used as a reference for a comparison with the test-beam setup. The sensor is glued on metal electrodes of the PCB. However, the metal electrode has a larger area than the metallization area of the sensors. The resulting bottom metallization is therefore larger than the top metallization pad as illustrated in Figure 88(a). This results in a difference of E_x and E_y as given in Figure 88(b). The E_y shows a similar decrease at the edge of top metallization pad as in the previous case where both metallization pads have the same size. In contrast, E_x decreases already under the area of the top metallization pad at the boarder resulting in a deflection of the charge carriers under the metallization. This deflection can cause a reduced CCE due to longer travelling time of the charge carrier or part of the generated charge carriers may not terminate at the readout pad and is lost. Outside of the top metallization pad a strong increase of E_x and E_y is visible resulting in a reduced CCE as already mentioned before.

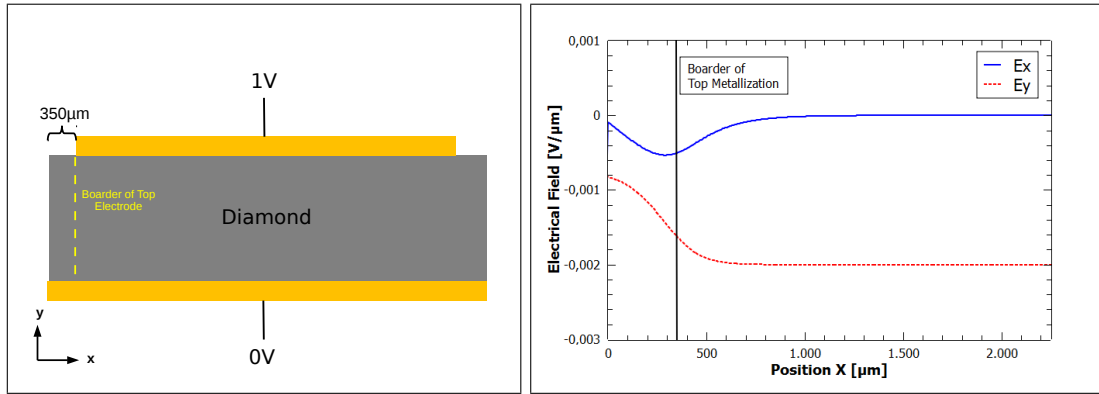


Figure 88: Superfish simulations for a parallel plate geometry with a longer bottom pad.

Summing up, edge effects of the CCE at the boarder of the metallization are explained by the electrical field deformation.

6.6.2 Simulation of Signal Sharing for Particles Crossing Near the Metallization Gap

In order to understand the signal sharing between the two readout pads, the weighting field of Chapter 4.3.1 is used.

Figure 89 illustrates the weighting field for a multiple pad configuration where the right upper pad is the readout pad. The weighting field and potential is obtained by setting the readout pad to unit potential and the other pads to zero.

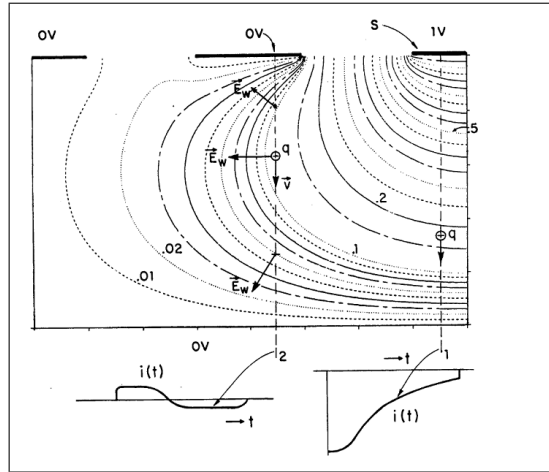


Figure 89: Illustration of the weighting field with the induced instantaneous current for a multiple pad configuration. Picture is taken from [80].

In the first case of Figure 89 a charge carrier is generated under the readout pad. Its instantaneous current has the same polarity at any time on its traveling way due to the weighting field that points always in the same direction. Therefore, the induced charge on the readout pad is a non-zero value. In the second case the charge carrier is generated under the neighbouring pad. However, the weighting field changes sign while the charge is moving perpendicular to the neighbouring pad. Therefore, the instantaneous induced current on the readout pad changes the polarity and its integral is zero. The induced charge on the readout pad for the second case is zero. This is as well explained by Equation 4.21.

In the case of the two pad sensor, used in the test-beam, two readout pads are available. The gap between the metallizations, in the order of $5\ \mu\text{m}$, is small compared to the thickness of $488\ \mu\text{m}$. Additionally, each pad is assumed to be infinitely long since the simulation are focused on the weighting potential around the gap between the metallizations. Therefore, a homogeneous electrical field is assumed where the x-component of the electrical field E_x is zero at any position and a free charge carrier travels perpendicular to the readout pad.

If we assume now a charge carrier under the neighbouring pad that is lost on the way to the pad, then the resulting integral of the induced current is non-zero. This induces a charge of different sign on the readout pad and a signal is generated even though the charge carrier is terminating under the neighbouring pad. A charge carrier can be lost due to trapping or recombination. Since the two pad sCVD sensor showed a reduced CCE of 80 %, it is assumed that 20 % of the generated charge carriers are lost on the way to the pads and a larger signal sharing area between the two metallizations is therefore expected. In order to know the consequences of the sharing effect on the measurement of the signal response as a function of the impact position, a simulation with Superfish is done.

Figure 90 illustrates the geometry used in the simulation. The upper left pad was set to unit potential and used as the readout pad. All other pads are set to zero potential in order to receive the weighting field and potential. The gap between the metallizations is set to $5\ \mu\text{m}$ and the thickness d to $488\ \mu\text{m}$.

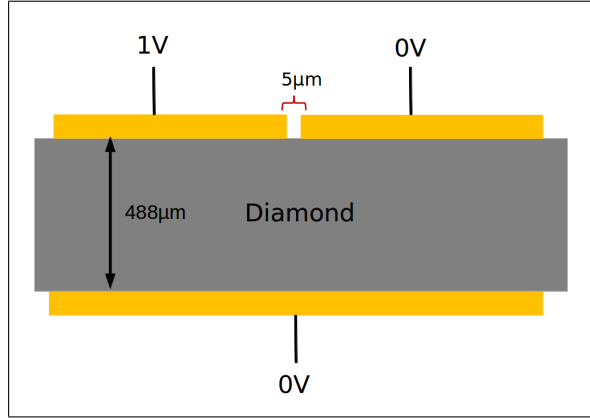


Figure 90: Illustration of the Superfish settings using the unit potential for the readout pad.

After feeding Superfish with these information the weighting field and potential for the two pad sCVD sensor geometry are obtained. Equation 4.23 allows to determine the induced charge of the readout pad by using the start and end point of the drift path of the charge carrier. Due to the CCE of 80 % it is assumed that the two pad sCVD sensor has 20 % of inefficient material. Therefore, three different configurations for the start and end of the drift path are possible:

1. the charge carrier is generated at the bottom pad and travels until 80 % of the sensor thickness.
2. the charge carrier is generated at 20 % of the sensor thickness and travels until 100 % of the sensor thickness corresponding to the top pad.
3. the charge carrier is generated at 10 % of the sensor thickness and travels until 90 % of the sensor thickness.

The first case is illustrated in Figure 91. A charge carrier is generated at the bottom pad with 0 % $\cdot d$ under the right pad that is not read out. Due to the electrical field the charge carrier moves perpendicular to the right pad and induces an instantaneous current. However, at a sensor thickness of 80 % $\cdot d$ the charge carrier is lost and the instantaneous current is interrupted since the charge carrier does not terminate at the right top pad. The integral of the instantaneous current is a non-zero value due to the missing 20 %.

All three cases are simulated and the induced charge is calculated as a function of the charge carrier position. This induced charge is proportional to the CCE with

$$\begin{aligned}
 CCE &= \frac{Q_{measured}}{Q_{expected}} \\
 Q_{measured} &\sim \Delta Q_A \\
 \Rightarrow CCE &\sim \Delta Q_A .
 \end{aligned} \tag{6.7}$$

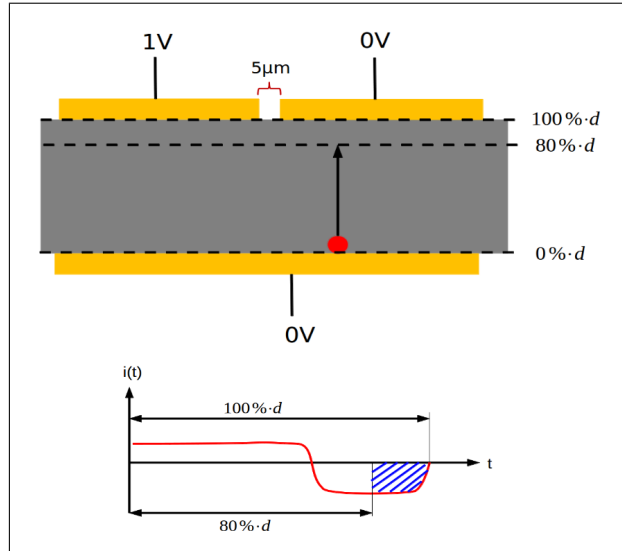


Figure 91: A charge carrier is generated under the neighboring pad and travels from the very bottom of the sensor material up to 80 % of the sensor thickness d where it is lost. The instantaneous current $i(t)$ on the readout pad is shown as a function of time. Since the charge carrier is lost at 80 % of the sensor thickness, 20% of the negative instantaneous current is missing in order to get an integral of zero.

Therefore, the simulated induced charged for the three previously mentioned cases are directly compared to the measured CCE (the data is taken from CH1 of Figure 85) and the results are given in Figure 92. The red dots are the CCE measurement, the green line is obtained for case 1, the magenta line for case 2 and the blue line for case 3. It is visible that the magenta line does not agree with the measurements and therefore case 2 is excluded. The blue one simulates the measurement points perfectly up to a position of -1 mm. However, the green line shows a good agreement to the CCE values as well. Case 1 and 3 illustrate that the large signal sharing area of around $400 \mu\text{m}$ around the metallization gap are due to the reduced CCE of 80 %.

The following conclusion are achieved, based on the information of the weighting potential and the measurements:

1. the sensor material has 20 % of inefficient material
2. the inefficient material is partially located close to the top pad
3. the inefficient material is not only located at the bottom pad
4. a reduced CCE leads to large signal sharing areas between two metallization pads

Summarizing, the detailed analysis of the gap between the two metallization pads shows a signal sharing effect that is observed for sensor with less than 100 % of CCE. The simulation of the test-beam data demonstrates that these observations are understood and even a localization of sensor material defects is possible [110].

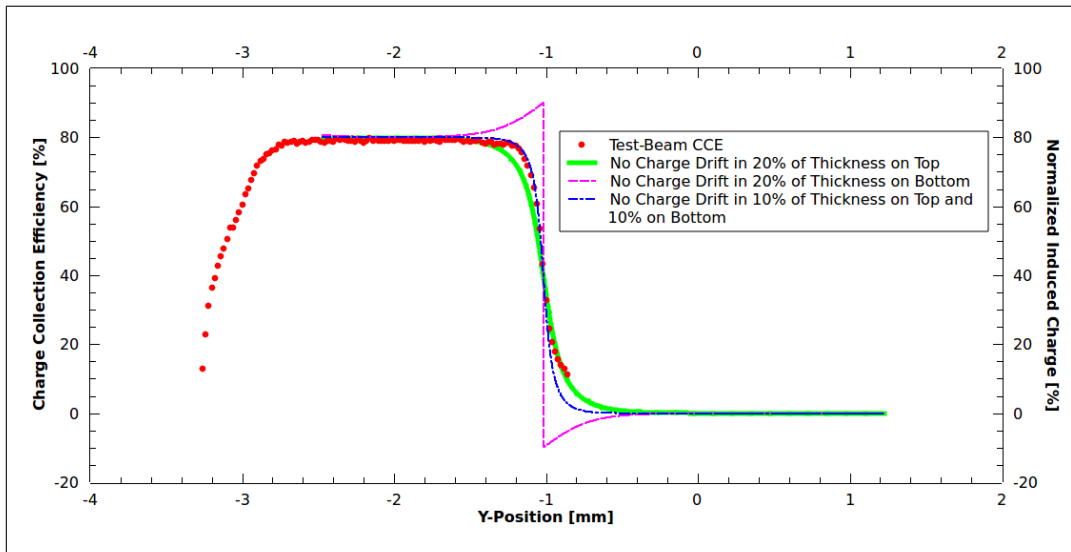


Figure 92: Simulations of the induced charge on the readout pad as a function of charge carrier position for the two pad sensor with reduced CCE of 80%. Three different cases are simulated whereas green represents the 1. case, magenta the 2. case and blue the 3. case. The red dots are the CCE measurement points.

7 Data Taking with the Beam Condition Monitor

The main purpose of BCM1F is to measure luminosity and MIB during the LHC fill independent of the main CMS data acquisition. Therefore, it still measures the beam condition also when CMS is not taking data. This chapter will firstly explain how the luminosity and MIB is measured and secondly show measurements results. The focus of the chapter is MIB and the reliability of this measurements.

7.1 Luminosity

7.1.1 Luminosity Estimation

Particles from MIB and collision products are separated by their arrival time in BCM1F. If an incoming bunch from the $+z$ or $-z$ (see Chapter 2) side reaches the location of BCM1F also MIB particles crossing the BCM1F sensors at the same time. After 6 ns the bunches collide in the CMS interaction point. Again 6 ns later the collision products and MIB particles of the outgoing bunch hit the BCM1F sensors. This happens for bunch crossings each 25 ns and is illustrated in Figure 93. Incoming bunches from the $+z$ side relate to beam 1 and incoming bunches from the $-z$ side relate to beam 2.

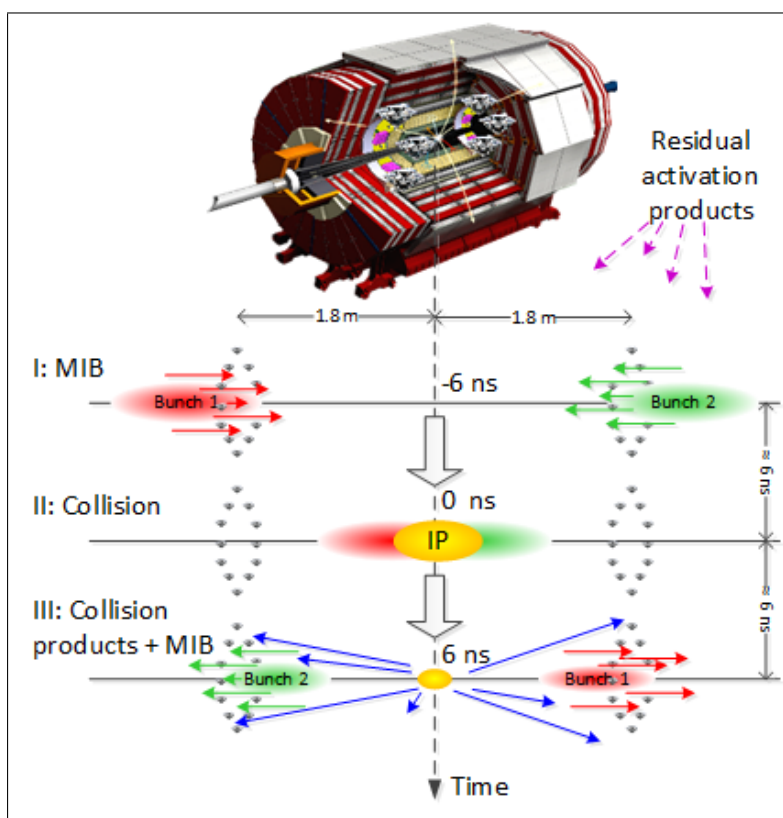


Figure 93: Illustration of arrival time of MIB and collision products in the BCM1F detector. [Courtesy of A. Zagodzinska]

The arrival time of charged particles in the sensor is fed into RHU histograms with a binning of 6.25 ns as explained in Chapter 3.1. An example of the rate as a function of time is shown

in Figure 94 for one bunch crossing. The first bin contains the background from the incoming bunch and the third bin, having the largest number of hits, is the sum of collision products and background particles of the outgoing bunch. The rate is read out and stored in time intervals of one lumi nibble being 0.364 s as already mentioned. In order to measure the luminosity, the content of the third bin of a bunch crossing is used.

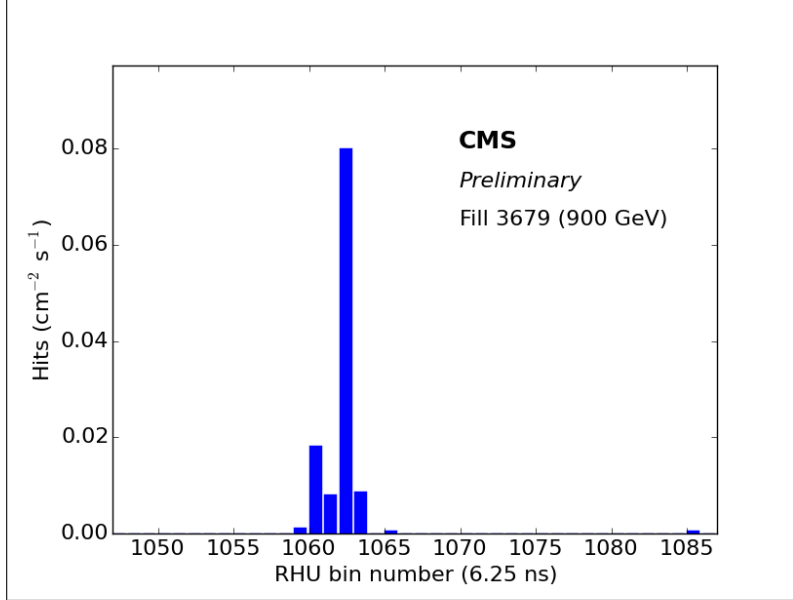


Figure 94: RHU rates as a function of RHU bin number taken during a LHC run with low collision rate. The first RHU bin represents MIB from the ingoing beam and 12 ns later the collision products plus outgoing beam are visible by a higher count rate.

The number of hits in each channel, n , follows a Poisson distribution. The probability to observe n hits reads:

$$P(n) = \frac{\mu^n e^{-\mu}}{n!}, \quad (7.1)$$

where μ is the mean value. The probability of zero hits $P(0)$, becomes

$$P(0) = e^{-\mu} \quad (7.2)$$

$$\mu = -\ln[P(0)] \quad (7.3)$$

$$= -\ln[1 - P(> 0)]. \quad (7.4)$$

This way of obtaining the mean value μ is called “Zero Counting Algorithm” and $P(> 0)$ is obtained from the measured rate in the third RHU bin. The luminosity can be expressed as a function of μ :

$$L = \frac{n_b f \mu}{\sigma_{visible}}, \quad (7.5)$$

where $\sigma_{visible}$ is the visible cross section in the detector and n_b the number of bunches [50].

Combining Equation 1.25 and Equation 7.5 the visible cross section reads:

$$\sigma_{visible} = \mu \frac{2\pi\Sigma_x\Sigma_y}{N_1N_2}, \quad (7.6)$$

where $\Sigma_{x/y}$ are the measured beam width in the horizontal and vertical plane (equivalent to $\sigma_{x/y}$). The visible cross section, Σ_x and Σ_y are measured in van-der-Meer scans [111]. During this scan the beams are systematically displaced in small steps in x- and y-direction and the rate in the RHU bin 3 of each displacement step is measured. No collision rates are expected when the displacement of the beam is large in comparison to Σ_x and Σ_y . In contrast, the collision rate reaches a maximum when the separation of the beams is zero and “head-on” collisions take place. The head-on collision rate is used to quantify the maximum mean value of hits μ from Equation 7.6. The measured collision rate for one bunch crossing as a function of displacement in the x- and y-direction is shown in Figure 95. The data is fitted by a double Gaussian due to the two overlapping beams having the width σ_1 and σ_2 . A fit determines the measured beam width Σ_x or Σ_y for each bunch crossing, related to σ_1 and σ_2 and their ratio. The horizontal beam width of the illustrated bunch crossing is $\Sigma_x = 123 \mu\text{m}$ and for the vertical beam width $\Sigma_y = 114 \mu\text{m}$.

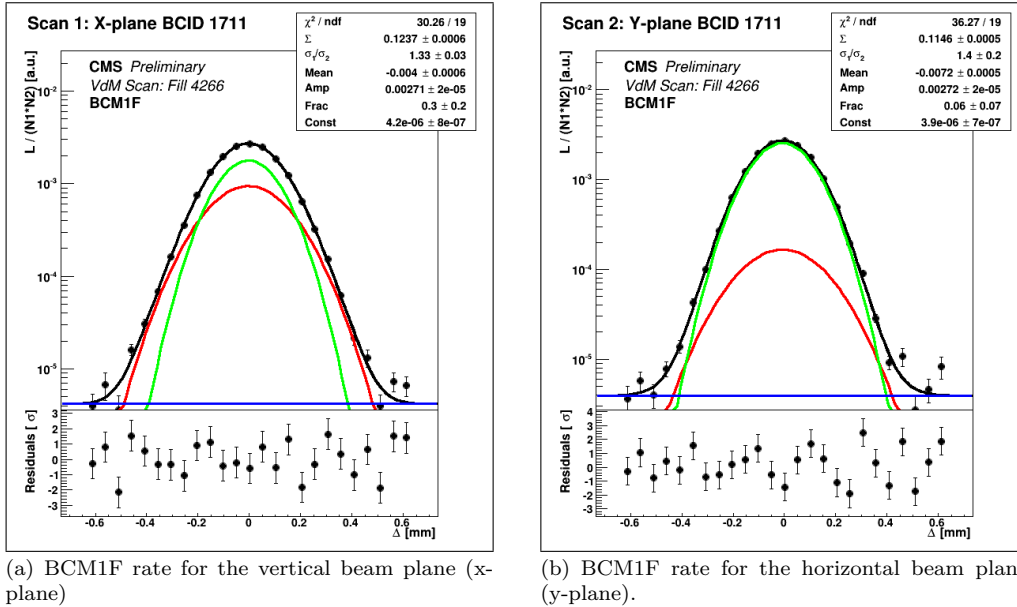


Figure 95: BCM1F rate measured during a van-der-Meer scan in August 2015 as a function of beam displacement. The data is fitted with a double Gaussian (green and red) with a constant (blue) representing the particle distribution for one crossing bunch of beam 1 and one of beam 2. The combined Gaussian fits form the black curve. [Courtesy of O. Karacheban]

7.1.2 Luminosity Measurement

The measured visible cross section from the van-der-Meer scan is then used for the luminosity determination during data taking that is calculated with Equation 7.5. The result of a luminosity measurement using BCM1F during a LHC fill from 2016 is shown in Figure 96. In addition, the two other luminometers, HF and PLT, are as well plotted. All three luminometers are in

agreement over the whole LHC fill, even when the LHC performed some tests during the fill where the luminosity was systematically changed.

The decrease of the luminosity over the LHC fill is due to two different reasons. One reason is a continuous decrease of the proton intensity due to beam losses and the collision itself. The second more severe reason is the transverse emittance growth of the bunches due to interactions of both beams as explained in Reference [112,113].

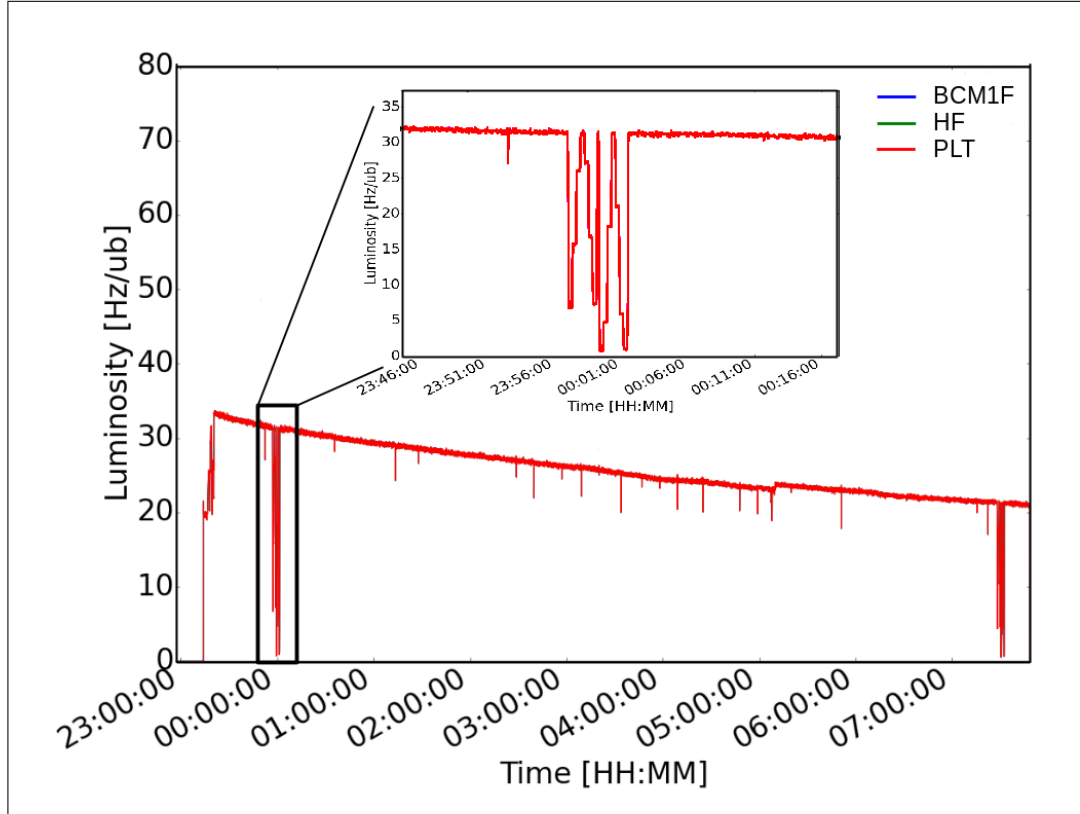


Figure 96: Luminosity measured by BCM1F (blue),HF (red) and PLT (green) as a function of time for one LHC fill. All three luminometers are overlaying and having the same measured luminosity during the fill. Optimization scans are performed at the end of the fill.

7.2 Machine Induced Background

Monitoring of the MIB is another crucial measurement of BCM1F. This information is distributed to the CMS and LHC control room. The inner tracker of CMS for example only starts to operate when the MIB is below a critical value. In addition, BCM1F is the only available tool for beam loss detection close to the CMS interaction point with the possibility to distinguish between beam 1 and beam 2 with 1 ns time resolution. In contrast, the LHC beam loss monitors are located outside of the CMS detector and the time resolution is 40 μ s. The vacuum gauges are close to the interaction of CMS but cannot differentiate between the two beams since there is only one beam pipe at this position. A feedback of the MIB rate measured by BCM1F is therefore essential for the LHC.

Different measurements were done to prove the right functionality of the MIB measurement.

7.2.1 Machine Induced Background Estimation

The rates in bin one of each bunch crossing of the RHU histogram are used for the MIB measurement. It is calculated for beam 1 and for beam 2 separately. In order to receive the MIB of beam 1, only RHU rates from the +z side BCM1F sensors are taken since the MIB of incoming bunches from the +z produces in these sensors a signal before the collision. Vice versa of beam 2 background measurements only the -z sensors (-z position) of BCM1F are used. Hereafter, the MIB of beam 1 is referred to as BKGD1 and for beam 2 as BKGD2.

Figure 97 shows the RHU rate as a function of arrival time after a bunch crossing of +z BCM1F sensors with high intensity beams. The rate in the first bin corresponds to BKGD1. It is likewise for BKGD2 using the RHU rates from -z BCM1F sensors. The content of the third bin, 12 ns after the MIB, is again used for the luminosity having a much higher rate than the MIB. A tail after the collision bin is visible called albedo having a short and long time component. Albedo is generated by particles created during the collision and arriving delayed in the BCM1F sensors as simulated and described in Reference [58].

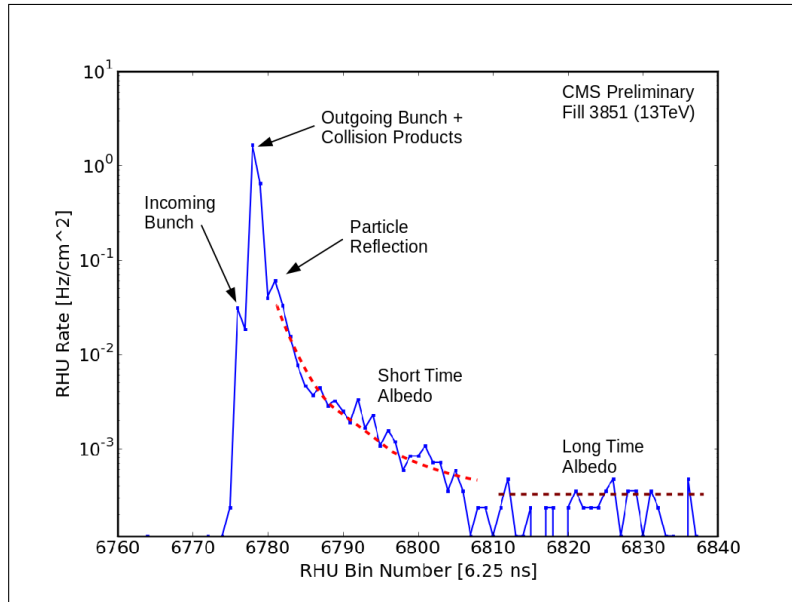


Figure 97: RHU rates as a function of the RHU bin taken during a LHC run with high intensity beams where the Albedo tail is visible.

Electrons and positrons contribute to the short tail and are present for up to 625 ns or 100 RHU bins (25 bunch crossings). 18.75 ns after the collision peak a third peak appears containing particles reflected from the endcap of the electromagnetic calorimeter. The long time component is mostly generated by photons and neutrons and visible as noise called grass as shown in Figure 98.

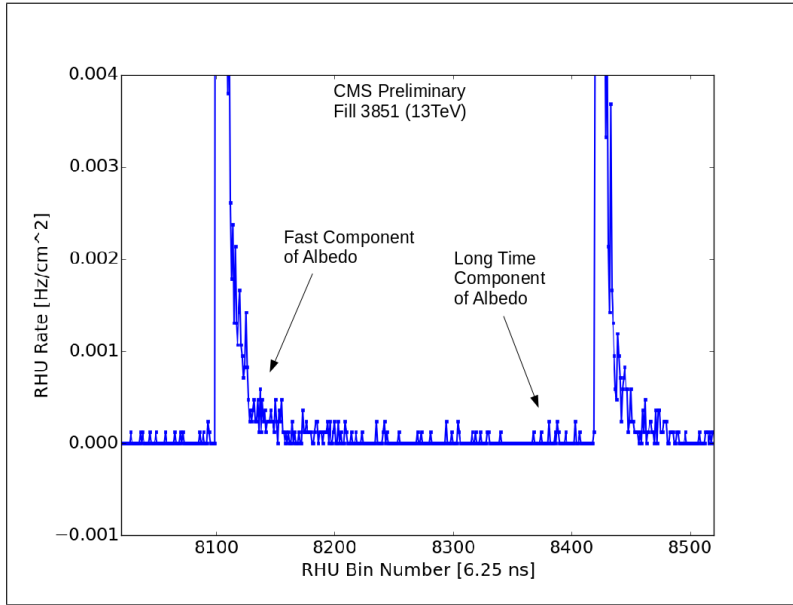


Figure 98: Rate as a function of the RHU bins for two consecutive bunch crossing.

In order to avoid the impact of the short time component of the albedo rate in the BKGD1 and BKGD2 estimation, only bunch crossing are taken into account if the previous 30 bunches do not collide, for example after the abort gap or the injection gap. If this criterion is valid for a certain bunch crossing, rates of the 1st bin of this bunch crossing will be taken and the long time albedo component is subtracted by averaging the rates from the 2nd bin of the previous 5 bunch crossings inside the 30 bunch crossings.

All used rates from the background bins are then added together and again normalized to 0.364 s, as described in Chapter 3.1, and the number of protons of the used bunches provided by the LHC group¹⁸.

7.2.2 Measurements of Machine Induced Background and the Vacuum in the Beam Pipe

Sources of the MIB are the residual gas particles. The density is enhanced by electron clouds as explained in Chapter 1.5. Therefore, the MIB rates depend on the vacuum pressure. Figure 99 shows the luminosity, the vacuum pressure and MIB rates at the +z and -z position as a function of time. The vacuum pressure is below $0.5 \cdot 10^{-10}$ mbar and the MIBs is below 0.05 counts/cm²s per 10^{11} protons. As soon as the collision starts and the luminosity goes up to $2000 \mu\text{b}^{-1}\text{s}^{-1}$, the vacuum pressure and MIBs start to increase. The collision products may cause an outgassing of the vacuum chambers resulting in a higher vacuum pressure of $4.5 \cdot 10^{-10}$ mbar at the +z and $3.5 \cdot 10^{-10}$ mbar at the -z side of CMS.

¹⁸The bunch current is measured by the fast beam current transformer (FBCT) using toroid transformers [114].

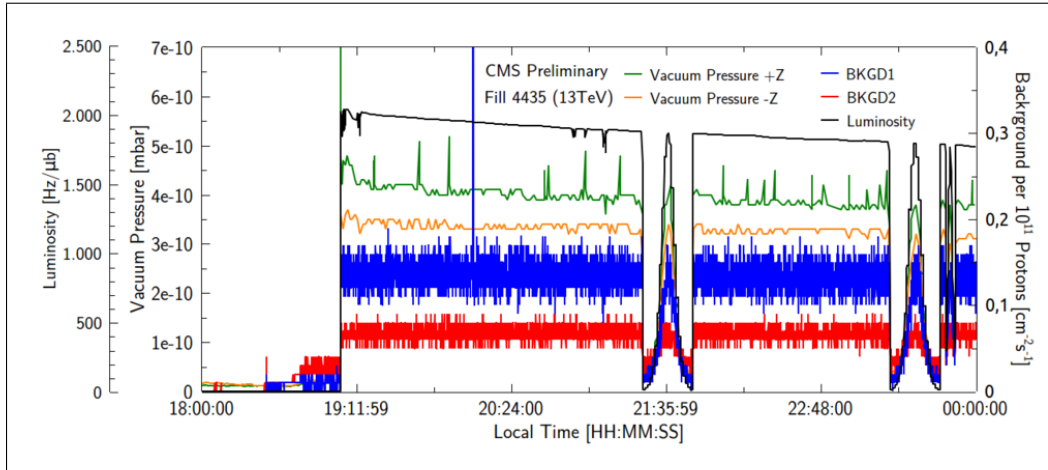
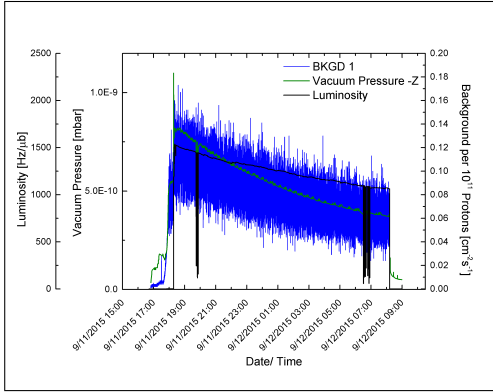


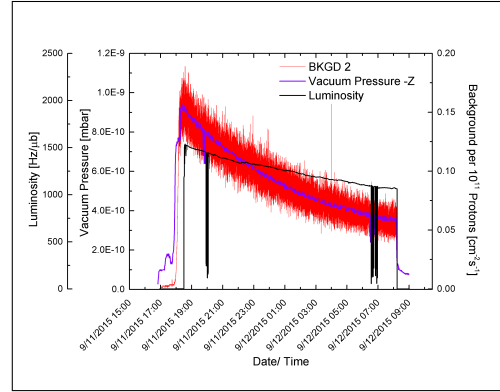
Figure 99: MIB measured during one LHC fill for beam 1 (BKGD1) in blue and for beam 2 (BKGD2) in red. The green and orange curves are the vacuum pressure during this LHC fill measured at the +z and -z side of CMS IP. The corresponding luminosity is given in the black curve.

BKGD1 follows the vacuum pressure on the +z side being 1.5 counts/cm²s per 10¹¹ protons and BKGD2 the vacuum pressure on the -z side being 0.6 counts/cm²s per 10¹¹ protons. Both the vacuum pressure on the +z side and BKGD1 are higher than the vacuum pressure on the -z and BKGD2. During the van-der-Meer scan the number of collision products is successively reduced and therefore the vacuum pressure is decreased. BKGD1 and BKGD2 follow again the vacuum pressure. This measurement shows that MIB is roughly proportional to the vacuum pressure.

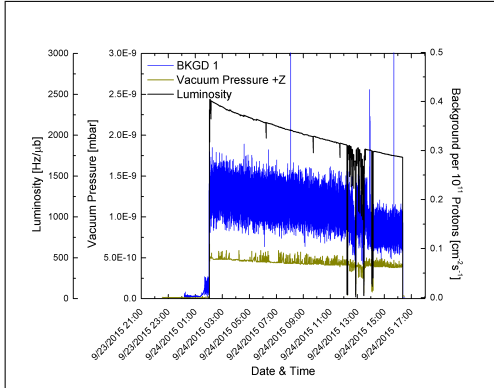
Generally, the electron cloud causes a raise of the vacuum pressure. However, the magnetic field of the CMS solenoid squeezes the electron cloud to the beam axis such it cannot enter the walls of the vacuum chamber. In the LHC operation in 2015 the CMS magnet was switched off for a while due to cooling problems. Therefore, measurements with an increased electron cloud effect were possible. Figure 100 shows the vacuum pressure and MIB for two different LHC fills. Data of the fill, illustrated in Figure 100(a) and 100(b), is taken while the magnet is switched off and Figure 100(c) and 100(d) while the magnet is switched on.



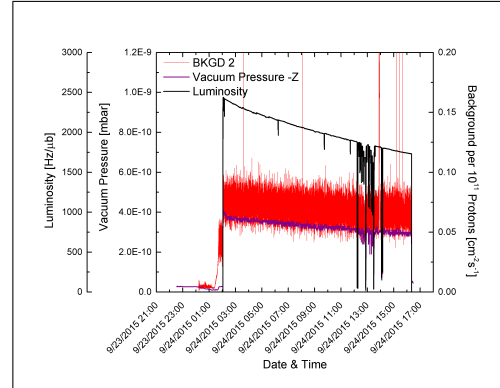
(a) MIB of beam 1 (blue), vacuum pressure at +z (green) and luminosity (black) during a LHC fill when the CMS magnet was switched off.



(b) MIB of beam 2 (red), vacuum pressure at -z (violet) and luminosity (black) during a LHC fill when the CMS magnet was switched off.



(c) MIB of beam 1 (blue), vacuum pressure at +z (green) and luminosity (black) during a LHC fill when the CMS magnet was switched on.



(d) MIB of beam 1 (red), vacuum pressure at -z (violet) and luminosity (black) during a LHC fill when the CMS magnet was switched on.

Figure 100: MIB for beam 1 and beam 2 with the corresponding vacuum pressure +z and -z while the CMS magnet is switched off (Figure 100(a) for beam 1 and 100(b) for beam 2) and switched on (Figure 100(c) for beam 1 and 100(d) for beam 2).

The initial vacuum pressure at the beginning of the collision is $8 \cdot 10^{-10}$ mbar for the +z side and $9 \cdot 10^{-10}$ mbar for the -z side while the magnet is switched off. The starting value of BKGD1 is in average 0.1 counts/cm²s per 10^{11} protons and of BKGD2 0.16 counts/cm²s per 10^{11} protons. In addition, an exponential decrease of the vacuum pressure is observed as well as for the MIB. This observation points to a reduction of the outgasing effect during the fill. This is considered as a conditioning of the surface of the vacuum chamber. If the magnet is switched on, the vacuum pressure and MIB are almost constant over time. Apparently, the outgasing effect due to the electron cloud is suppressed. This is also visible in a lower vacuum pressure at the beginning of the fill being $5 \cdot 10^{-10}$ mbar and $4 \cdot 10^{-10}$ mbar for the +z and -z side of CMS. BKGD2 follows this observation with a reduced MIB of 0.075 counts/cm²s per 10^{11} protons in average. However, BKGD1 showed a high MIB of 0.2 counts/cm²s per 10^{11} protons in average. This was not a beam effect but due to the malfunctioning of some sensors on the +z position. Some sensors on the BKGD1 side showed large currents and erratic signals while the magnet was switched off. Therefore, the bias voltage of such sensor was reduced while the magnet is off and increased again as soon as the magnet was on. At lower bias voltage the sensors are not fully efficient. A higher

rate is then measured when the bias voltage was increased while the magnet was switched on. A few sensors on the $-z$ position were working perfectly and a change of the bias voltage was not needed.

The presented analysis of the electron cloud shows the first time the effect of the CMS magnet switched on and off on the vacuum pressure and MIB.

7.2.3 Machine Induced Background as a Function of Collimator Settings

Another source of MIB is secondary particles originating from the interaction between protons and collimators as mentioned in Chapter 1.5. The number of secondary particles is intentionally enhanced during a LHC machine development by venting the vacuum pipes with a small amount of hydrogen on the $+z$ and $-z$ side of CMS right upstream the TCT collimators, around 150 m away from the CMS IP. This leads to an increased vacuum pressure resulting in a higher amount of deflected particles crossing the TCT collimators in front of CMS. It is the first measurement proving the proportionality between secondary shower rate and the MIB. Data of the vacuum gauge on the $+z$ and $-z$ side of CMS is used to compare it to BKGD1 and BKGD2.

Figure 101 shows the vacuum pressure on the $+z$ and $-z$ side of the CMS as a function of time and the measured BKGD1 and BKGD2 respectively. The background rates follow the vacuum pressure as expected. In addition, a linear dependency between both quantities is observed in Figure 102 showing that deflection of beam particles and the production of the secondary shower is proportional to the MIB rates.

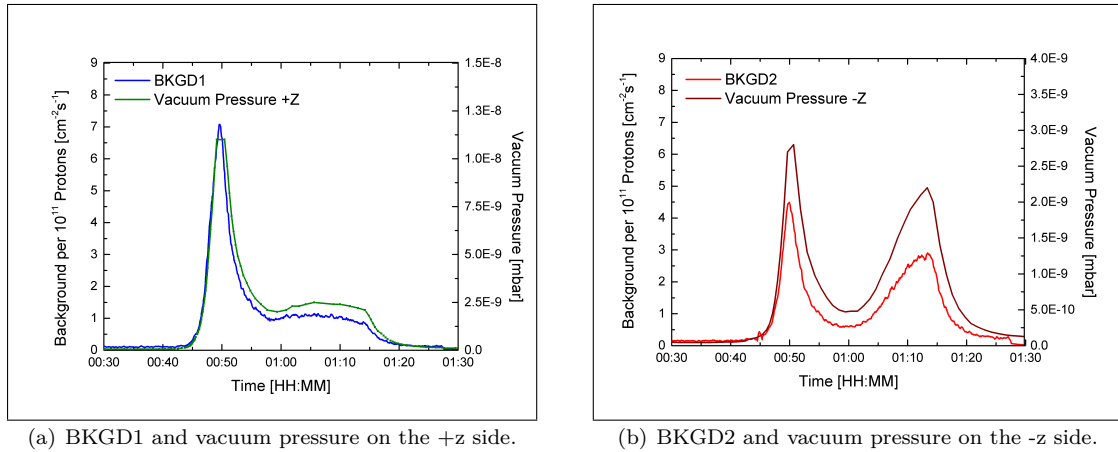


Figure 101: Vacuum pressure and MIB as a function of time for the $+z$ and $-z$ side. The data is taken during a machine development when vacuum pressure is intentionally increased.

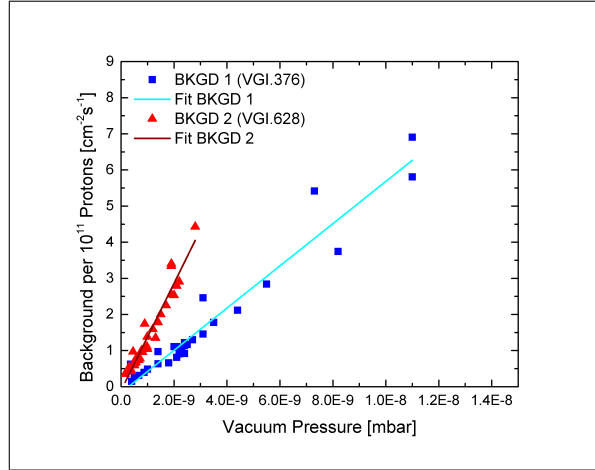


Figure 102: BKGD1 and BKGD 2 rates as a function of the vacuum pressure on the +z and -z side of CMS respectively.

The MIB is also studied for different settings of the TCT collimators next to CMS. The LHC settings at the start-up of Run 2 in 2015 after LS 1 were done with a high safety margin. Parameters like β^* 80 cm were used as during the operation in 2015. The half-opening of the TCT collimators are set to 15σ being close enough to intercept sufficiently beam losses and being large enough to reduce the MIB. However, in order to increase the luminosity a smaller emittance and β^* is required as can be seen in Equation 1.27. This is only feasible if the collimator half-opening is reduced leading to a higher number of intercepted beam losses. However, an increase of secondary particles downstream the collimators is expected. A first quantification is given by the following measurement analysis of the data from the machine development.

The scan was performed with the following program:

1. injection of 15 pilot bunches and 1 nominal bunch¹⁹ per beam with $\beta^*=40$ cm.
2. changing the half-opening of the TCT collimators next to CMS in 0.5σ steps.
3. provoking beam losses²⁰ in beam 1 horizontal plane, beam 1 vertical plane, beam 2 horizontal plane, beam 2 vertical plane.
4. same as in 3 plus moving in TCLA absorbers (see Chapter 1.2) to improve the cleaning of the beam losses.

The analysis of the data uses raw RHU data by summing up all signals for each bunch crossing separately over a time interval of about 1 s. This data is compared to the BLM dose close to the TCP collimator in IR7 where all beam losses around the LHC are visible. This measured beam loss dose is proportional to the bunch intensity [20].

¹⁹The nominal bunch has around $1.2 \cdot 10^{11}$ protons corresponding to the nominal settings of the LHC and the pilot bunches around 10^9 protons.

²⁰Beam losses are produced by exciting the bunches with a transverse damper (ADT) by applying an electrical field to two electrodes [115, 116].

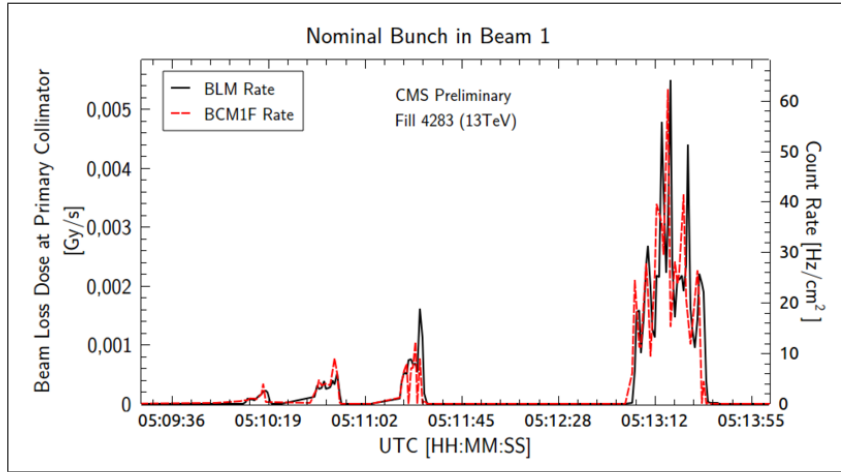


Figure 103: Beam losses of the nominal bunch from beam 1 as a function of time measured with the BLMs (black curve) and the BCM1F (red dashed curve). The location of the used BLM is TCP.D6L7 (see Figure 9).

Figure 103 shows the BCM1F rate and BLM dose rate from the provoked beam losses in the nominal bunch of beam 1 (vertical) at a TCT collimator half-opening of 8.8σ . Four beam losses are visible and the first three are small compared to the fourth one. Both BCM1F rates and BLM dose as a function of time show the same beam loss pattern. The rates of BCM1F and BLM dose of the nominal bunch of beam 2 (horizontal) with again 8.8σ are shown in Figure 104. They are significantly smaller but again some relation between BCM1F rates and BLM dose is visible. This might be due to the excitation process itself. Even smaller beam losses are observed for the pilot bunches having less number of protons. One of these losses with 8.3σ half-opening of the TCT collimator is shown in Figure 105. Again BCM1F and BLM measure the same beam loss pattern.

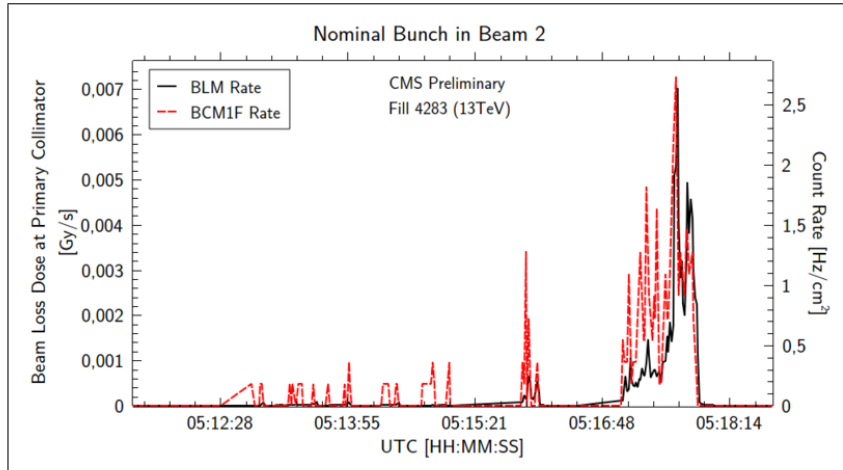


Figure 104: Beam losses of the nominal bunch from beam 2 as a function of time measured with the BLMs (black curve) and the BCM1F (red dashed curve). The location of the used BLM is TCP.D6R7 (see Figure 9).

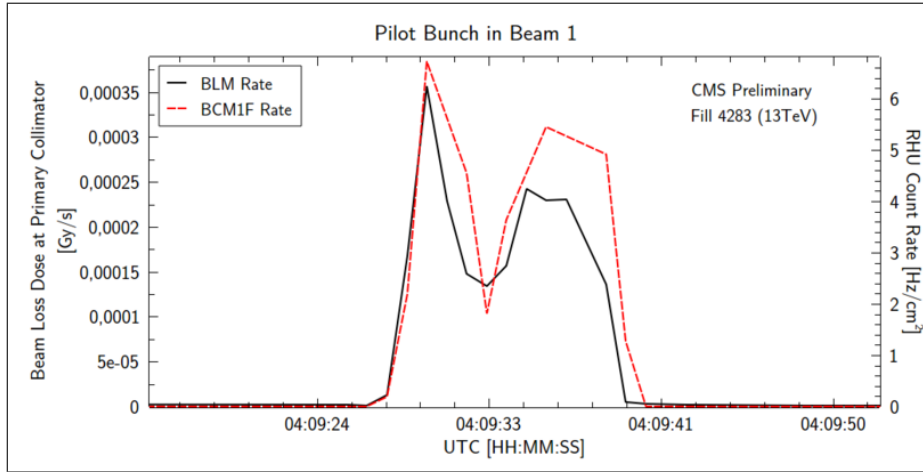


Figure 105: Beam losses of the pilot bunch from beam 1 as a function of time measured with the BLMs (black curve) and the BCM1F (red dashed curve). The location of the used BLM is TCP.D6L7 (see Figure 9).

This BCM1F rate is not yet corrected for the number of protons of the used bunch being continuously decreasing due to the lost protons. It is therefore normalized by the BLM dose measured at the TCP collimator for the horizontal and vertical direction, respectively in IR7. Figure 106 shows the normalized BCM1F rate of the horizontal plane of beam 1 for different TCT collimator half-openings. The same is given for the vertical plane of beam 1 in Figure 107. A decrease of the normalized BCM1F rate for higher TCT collimator half-opening is visible in both cases. This is due to the reduced number of protons hitting the collimator with higher half-opening and producing a smaller amount of secondary showers. These secondary showers become even less if the TCLA absorbers are moved in (additional cleaning) compared the absorbers moved out (no additional cleaning). A detailed analysis of a normalized BCM1F rate of beam 2 is not possible since the beam loss rate was too small to be visible with BCM1F.

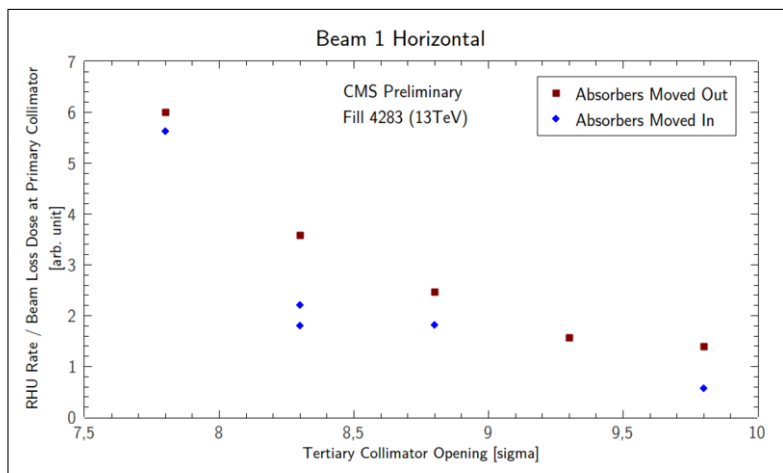


Figure 106: Normalized BCM1F rates of horizontal beam losses of beam 1 as a function of the TCT (tertiary) collimator opening gap.

8 Summary and Conclusion

BCM1F measured successfully luminosity and machine induced background during Run 1. Data was sent to the LHC and CMS control room in order to optimise the beam parameters and to send feedback for losses inside CMS. Run 2 involved an increase of the beam energy from 4 TeV to 6.5 TeV and decrease of the bunch spacing from 50 ns to 25 ns. Due to the success of BCM1F and the enhanced requirements an upgrade of BCM1F was done.

The upgrade comprised the sCVD sensors, the front-end ASIC and the holding carriage. 12 sCVD sensors on each side of the CMS interaction point were installed to ensure redundancy. Each sensor was metallized with a two pad to reduce the occupancy. Signals from the sCVD sensors are amplified by a dedicated amplifier based on 130 nm CMOS technology. The amplifier output pulse has a FWHM of less than 10 ns and allows a signal response up to 150 fC (corresponding to 50 times a MIP signal) without showing an undershoot. Both the sCVD sensor and amplifier are placed on the new holding carriage, the C-shape. It connects the amplifier with the AOH by a flexible ribbon cable. The AOH converts the electrical signal to an optical signals and is placed further away from the beam, compared to the Run 1 BCM1F settings, reducing the radiation damage on the AOH.

58 sCVD sensors were fully optically and electrically characterized in order to equip BCM1F with 24 sCVD sensors of a quality that promises stable operation. Each sensor was first optically inspected to measure the overall sensor thickness and then sent for metallization. Two types of metallization were available for two pads, Cr/Au and W/Ti. Again after the metallization an optical inspection was done to obtain the metallization geometry. Afterwards an electrical characterization was done by measuring the leakage current, the signal stability over 5 h and the CCE. Only sensors fulfilling certain criteria were considered for installation on the C-shape that are given in Chapter 4.4. The leakage current must be small enough, the signal stable over the complete time episode and the CCE measurements stable up to 1 kV for at least one polarity. Most of the sCVD sensors matched the selection criterion for one polarity but not for both polarities. Only 33 sCVD sensors were selected for the BCM1F installation and 9 of them fulfilled the selection criteria for both polarities. Further test were done by comparing the metallization type and pattern. However, the metallization pattern did not show an influence on the electrical behaviour. In contrast, the comparison of the metallization type showed that the leakage current is reduced but still present for the Cr/Au metallization. This measurement showed in addition that the increased leakage current is due to material defects. These sensors were not installed. For a better understanding further studies and measurement campaigns are required. Future simulations may help to get an insight into the electrical behaviour of the sensor material in more detail.

Two sCVD sensors, a reference sensor with a one pad and a sensor with a two pad, were chosen for the test-beam to test the complete front-end system. Measurements were done at the DESY-II facility with a 5 GeV electron beam. One measurement was the signal response showing a signal with a FWHM of less than 10 ns for both sensors. The specifications of the front-end ASIC are verified. The S/N ratio was measured to be 40 for the one pad sensor and 30 for the two pad sensor. The smaller S/N ratio of the two pad sensor results from a reduced CCE of 80 % where the one pad sensor has in contrast a CCE of 100 %. A study of the CCE as a function of the electron impact position was done. It showed a reduced CCE under the metallization edge and around the gap between the two metallization pads over a distance of 400 μm . Simulations with the program

Superfish, calculating the electric field, were done to explain these two effects. The reduction of the CCE under the edge of the metallization is enhanced by the bias electrode covering the complete sensor material and being larger than the metallization pad itself. This leads to a deformation of the electric field under the metallization and to a reduced CCE. All measurement results of the two pad sensor with a CCE of 80% indicated charge trapping within the sensor bulk. The simulation showed that an additional reduction of the CCE around the gap between the two metallization is due to signal sharing. Charge created under the readout electrode is trapped and generates a signal also in the neighbouring electrode as explained by Ramo's theory [79]. Both measurements and simulation are in good agreement. The simulation showed that inefficient sensor material where the charge is trapped is located partially under the top electrode. Summarizing, the BCM1F test-beam demonstrates that the upgraded BCM1F is fully functioning and the measurement results are understood.

The upgraded BCM1F was installed during LS 1 and operating since the start of Run 1. The sensor signals are analyzed by ADCs, μ TCA's and RHUs. The ADC with a sampling time of 2 ns will be replaced by μ TCA since both are used for the signal sampling but the μ TCA has a smaller sampling time of 0.8 ns and an integrated peak finding algorithm. Data of the ADC and μ TCA are used to analyse the amplitude spectrum of the incoming signals. The position of the MIP peak and saturation position of the amplitude spectrum give information about radiation damage and the functionality of BCM1F. The RHU measures the arrival time of the signals with a binning of 6.25 ns. The position of BCM1F was chosen such that first machine induced background particles of an incoming bunch are counted in the RHU, and then after 12 ns, collision products. Therefore, rates coming from machine induced background and luminosity are measured separately by the RHU.

Luminosity is measured by BCM1F in order to measure the cross sections of the physics processes happening during the collision. BCM1F is decoupled from the main CMS data taking and measures luminosity even if CMS is not taking data. PLT and HF are two additional luminometers inside CMS measuring luminosity. A comparison shows that all three luminometers are in good agreement. It is also essential to measure machine induced background to protect CMS in case of adverse beam condition. Additionally, BCM1F sends feedback to the CMS pixel detector which only turns on if the machine induced background is below a certain threshold.

Machine induced background is caused by different sources. Firstly, residual gas particles cause a deflection of the protons within the LHC ring and the interaction with material of the LHC produce secondary shower measured by the BCM1F sensors. Secondly, deviated protons may hit the collimators right before CMS and produce secondary particles downwards that hit the BCM1F sensors.

A dependence of the machine induced background on the vacuum pressure is demonstrated. The effect of the electron cloud leads in addition to an increase of the vacuum pressure. Electron cloud is however suppressed inside CMS if the CMS magnet is switched on. Data of the BCM1F measured machine induced background show an increase while the magnet was switched off, and an increase of the vacuum pressure. This correspondence is shown for the first time. Two types of LHC tests were done to prove the functionality of BCM1F. During the first test hydrogen gas was flooded into the LHC ring right in the vicinity of the collimators on both sides of CMS. The increase of the vacuum pressure led to an increase of beam losses hitting the collimator and producing a secondary shower that was measured by BCM1F. The BCM1F machine induced background rates followed

the vacuum pressure as it was expected and now proven. A second LHC test involved an excitation of bunches producing again beam losses hitting the collimators. Such beam losses were provoked for different collimator settings where the smallest half opening of the collimator produces the highest amount of secondary showers. Firstly, the same loss pattern was observed comparing BCM1F rates and BLM dose installed in the LHC ring. Secondly, the BCM1F rates depended on the collimator settings. The BCM1F rates were increasing with a decreasing half opening gap of the collimator as it was expected. This was also investigated for the first time.

All in all, it is shown in this thesis that BCM1F is a reliable tool to measure machine induced background. The data taken is in agreement with all supplement measurement devices such as the vacuum pressure and the BLMs.

List of Figures

1	Illustration of the Standard Model containing fermions and bosons	22
2	Feynman diagrams for Higgs production	23
3	LHC schematic with its 8 insertion regions	24
4	Accelerator complex including the pre-accelerators	25
5	LHC bunch structure	25
6	Particle trajectory within a sector magnet	26
7	Illustration of magnetic field of quadrupole	27
8	Photo of collimator	28
9	Locations of collimators in the LHC ring	28
10	Layout of beam cleaning	29
11	Ionization chambers installed outside of a magnet	30
12	Photo of inside of an ionization chamber	30
13	Illustration of particle movement relative to the closed orbit	31
14	Betatron oscillation and its envelope	32
15	Illustration of electron cloud	35
16	CMS layout	37
17	Quarter of CMS with BRIL detector locations	42
18	BCM1F sensor carriage	43
19	Readout scheme of BCM1F sensors	44
20	BCM1F signal measured with ADC	44
21	Limitations of BCM1F front-end	45
22	BCM1F holding carriage	46
23	Metallization with two pads	47
24	Pulse shape with upgraded amplifier.	47
25	BCM1F signal processing with ADC	48
26	BCM1F signal processing with μ TCA	49
27	BCM1F arrival time histogram taken with BCM1F	50
28	Diamond lattice	51
29	Illustration of CVD reactor	52
30	Illustration of CVD diamond growth	53
31	Illustration of pCVD diamond structure	54
32	Band structure for ohmic and Schottky contact	56
33	Energy loss of muons, pions and protons for hydrogen, gaseous helium, carbon, aluminium, iron, tin and lead.	58
34	Energy loss of electrons in diamond with a supposed density of 3.53 g/cm^3 . The data is taken from the ESTAR database on www.nist.gov	59
35	Landau distribution	60
36	Illustration of point defects in diamond	64
37	Illustration of defect mechanism	64
38	Laser microscope for optical inspection	67
39	Three dimensional picture of sensor scanned with laser microscope	68
40	Analysis program of optical measurement	68

LIST OF FIGURES

41	Thickness values for 59 measured sensors	69
42	Optical inspection of metallized sensors	69
43	Schematic of setup for the leakage current	70
44	Leakage current Measurement for three sensors	71
45	Schematic of setup for the signal current	72
46	Signal stability measurement for two sensors	73
47	Setup for the charge collection efficiency	74
48	Scheme of signal treatment for CCE measurement	75
49	ADC spectra for 60 V and 600 V	76
50	CCE as function of bias voltage for two sensors	77
51	Quality of sensor classified by the leakage current	80
52	Sensor quality classified by signal current	81
53	Sensor quality classified by the CCE	82
54	IV comparison for W/Ti and Cr/Au of metallizations	83
55	Comparison of signal stability for W/Ti and Cr/Au metallization	84
56	IV comparison for one and two pad metallization	85
57	Comparison of signal stability for one and two pad metallization	86
58	Test-Beam Layout	87
59	Schematic of Setup	88
60	Scheme of signal and trigger processing	88
61	Picture of test-beam area	89
62	DUT Box between the two telescope arms.	90
63	Picture of PCB used for the test-beam	90
64	Diamond sensors on the PCB	91
65	Geomtery of Mimosa-26 sensors	93
66	Setup of alignment run	93
67	Definition of variables for track reconstruction	94
68	Fitted telescope tracks	95
69	Number of reconstructed tracks	96
70	Sampled DUT signal	96
71	Electron beam profile measured with the telescope impact position	98
72	Laboratory measurements for one pad sensor.	99
73	Laboratory measurements for two pad sensor.	100
74	Circuit diagram for calibration.	101
75	Signal amplitude for calibration	101
76	Signal of one pad sensor.	102
77	Signals from each channel of the two pad sensor	103
78	Geometry of one pad sensor	104
79	Geometry of two pad sensor.	104
80	Amplitude spectrum of one pad sensor.	105
81	CCE and S/N of one pad sensor measured during the test-beam.	106
82	Amplitude spectra of two pad sensor.	106
83	CCE and S/N ratio as a function of bias voltage of the two pad sensor measured during the test-beam.	107

LIST OF FIGURES

84	Homogeneity study of one pad sensor	109
85	Homogeneity study of two pad sensor	110
86	Illustration of the electrical field lines for parallel plate geometry.	111
87	Superfish simulations for a parallel plate geometry with top and bottom pad having the same size.	111
88	Superfish simulations for a parallel plate geometry with a longer bottom pad.	112
89	Illustrations of of weighting field.	113
90	Illustrations of Superfish settings.	114
91	Illustration of moving charge carrier for a sensor with 80% CCE	115
92	Superfish simulation for the two pad sensor.	116
93	Illustration of arrival time of MIB and collision products	117
94	RHU rates during collision with low collision rate	118
95	Measured BCM1F rate during a van-der-Meer scan in the vertical and horizontal plane from August 2015.	119
96	Luminosity measurement of BCM1F, HF and PLT	120
97	RHU rates during collision with high intensity beams.	121
98	Fast and long time component of albedo rate	122
99	Correlation of MIB with vacuum pressure and luminosity	123
100	MIB for beam 1 and beam 2 while the CMS magnet was switched off	124
101	Vacuum pressure and background as a function of time measured during machine development	125
102	BKGD1/2 rates as a function of the vacuum pressure on the +z and -z side of CMS	126
103	Beam losses of a nominal bunch from beam 1 measured by BLMs and RHU during machine development	127
104	Beam losses of a nominal bunch from beam 2 measured by BLMs and RHU during machine development	127
105	Beam losses of a pilot bunch of beam 1 measured by BLMs and RHU during machine development	128
106	BCM1F rates for the horizontal beam losses of beam 1 as a function of collimator settings	128
107	BCM1F rates for the vertical beam losses of beam 1 as a function of collimator settings	129

List of Tables

1	Comparison of the nominal LHC parameters with the operational ones in Run 1 (2012) and Run 2 (2016).	21
2	Decay channels of Higgs boson with their branching fractions and the mass resolution when reconstructing the mass of the Higgs boson from the decay products.	23
3	Detectors within the BRIL project with their location, type of sensor and responsibility.	42
4	Variables for Bethe Bloch formula.	57
5	Fit parameters of pedestal and signal distribution of Figure 49 measured for 60 V and 600 V.	76
6	Summary of the sensor characterization	79
7	Summary of sensor meeting all three selection criteria for one and both polarities.	83
8	Front-end ASIC, opto-hybrid and ADC channel numbers used for the DUT test-beam board.	91
9	Calibration factor k and sensor thickness of each sensor pad connected to the front-end ASIC.	102
10	Decrease of CCE for CH1 and CH2 of two pad sensor measured at 130 V	108
11	Decrease of CCE for CH1 and CH2 of two pad sensor measured at 300 V	108
12	Decrease of CCE for CH1 and CH2 of two pad sensor measured at 500 V	108

References

- [1] G. Aad et al. Observation of a New Particle in the Search for the Standard Model Higgs Boson with the ATLAS Detector at the LHC. *Physics Letters B*, 716(1, pp. 1-29), 2012.
- [2] S. Chatrchyan et al. Observation of a New Boson at a Mass of 125 GeV with the CMS Experiment at the LHC. *Physics Letters B*, 716(1, pp. 30-61), 2012. <http://www.sciencedirect.com/science/article/pii/S0370269312008581>.
- [3] R. Schmidt et al. Protection of the CERN Large Hadron Collider. *New Journal of Physics*, 8(11):290, 2006.
- [4] Website, <http://cerncourier.com/cws/article/cern/54381>, found on the 02.08.2016.
- [5] F. Englert and R. Brout. Broken Symmetry and the Mass of Gauge Vector Mesons. *Phys. Rev. Lett.*, 13, pp. 321-323, 1964.
- [6] P. W. Higgs. Broken Symmetries and the Masses of Gauge Bosons. *Phys. Rev. Lett.*, 13, pp. 508-509, 1964.
- [7] Website, <http://www.physik.uzh.ch/groups/serra/StandardModel.html>, found on the 09.08.2016.
- [8] D. Denisov. Moriond QCD 2013 Experimental Summary. In *Proceedings, 48th Rencontres de Moriond on QCD and High Energy Interactions: La Thuile, Italy, March 9-16, 2013*, pages 379–406, 2013. <https://inspirehep.net/record/1240505/files/arXiv:1306.6908.pdf>.
- [9] CMS Collaboration. Properties of the Higgs-like Boson in the Decay H to ZZ to $4l$ in pp Collisions at $\sqrt{s} = 7$ and 8 TeV. 2013, CMS-PAS-HIG-13-002.
- [10] ATLAS Collaboration. Study of the Spin and Parity of the Higgs Boson in Diboson Decays with the ATLAS Detector. *Eur. Phys. J.*, C75(10):476, 2015. CERN-PH-EP-2015-114.
- [11] ATLAS Collaboration. Higgs Pair Production at the High Luminosity LHC. 2015, CMS-PAS-FTR-15-002.
- [12] ATLAS Collaboration. Prospects for Measuring Higgs Pair Production in the Channel $H(\rightarrow \gamma\gamma)H(\rightarrow b\bar{b})$ Using the ATLAS Detector at the HL-LHC. 2014, ATL-PHYS-PUB-2014-019.
- [13] K.A. Olive et al. (Particle Data Group). Passage of Higgs Boson Physics. *Chin. Phys. C*, 38, 090001 (2014) and 2015 update.
- [14] M. Benedikt et al. *LHC Design Report, Volume 3*. CERN, Geneva, 2004.
- [15] S. Baird. Accelerator for Pedestrians; Rev. Version. Technical report. Technical Report, AB-Note-2007-014, CERN-AB-Note-2007-014, CERN, Geneva, 2007.
- [16] O. Brüning. *LHC Design Report, Volume I*. CERN, Geneva, 2004.
- [17] S. Redaelli et al. Operational Performance of the Collimation. *Proceedings of HB2010*. Morschach, Switzerland, 2010, TUO2C05.

- [18] M. Stockner et al. Measurements and Simulations of Ionization Chamber Signals in Mixed Radiation Fields for the LHC BLM System. In *2006 IEEE Nuclear Science Symposium Conference Record*, volume 3, pp. 1342-1345, 2006.
- [19] E. B. Holzer et al. Beam Loss Monitoring for LHC Machine Protection. *Phys. Procedia*, 37:2055–2062. 8 p, 2012.
- [20] M. Hempel. Application of Diamond Based Beam Loss Monitors at LHC. Master's thesis, DESY, Zeuthen, 2013. DESY-THESIS-2013-014, CERN-THESIS-2012-307, <http://www-library.desy.de/cgi-bin/showprep.pl?thesis13-014>.
- [21] K. Wille. *The Physics of Particle Accelerators*. Oxford University Press, 2000.
- [22] H. Wiedemann. Springer Verlag, 2007.
- [23] T. Baer. Very Fast Losses of the Circulating LHC Beam, Their Mitigation and Machine Protection. PhD Thesis, Hamburg University, 2013, CERN-THESIS-2013-233, <http://cds.cern.ch/record/1637966>.
- [24] O. Dom Inguez and F. Zimmermann. Benchmarking Electron-Cloud Simulations and Pressure Measurements at the LHC. *E-CLOUD 12: Joint INFN-CERN-EuCARD-AccNet Workshop on Electron-Cloud Effects, La Biodola, Isola d Elba, Italy, 2012*. CERN-2013-002, pp. 79-83.
- [25] Website, <http://ab-abp-rlc-ecloud.web.cern.ch/ab-abp-rlc-ecloud/>, found on the 06.08.2016.
- [26] The CMS Collaboration. The CMS experiment at the CERN LHC. *Journal of Instrumentation*, 3(08):S08004, 2008.
- [27] Y. Allkofer et al. Design and Performance of the Silicon Sensors for the CMS Barrel Pixel Detector. *Nuclear Instruments and Methods in Physics Research Section A: Accelerators, Spectrometers, Detectors and Associated Equipment*, 584(1):25 – 41, 2008.
- [28] CMS Collaboration. Commissioning and Performance of the CMS Pixel Tracker with Cosmic Ray Muons. *Journal of Instrumentation*, 5(03):T03007, 2010.
- [29] Vardan Khachatryan et al. CMS Tracking Performance Results from early LHC Operation. *Eur. Phys. J.*, C70:1165–1192, 2010.
- [30] R.M. Brown. Avalanche Photodiodes and Vacuum Phototriodes for the CMS Electromagnetic Calorimeter. *Nuclear Instruments and Methods in Physics Research Section A: Accelerators, Spectrometers, Detectors and Associated Equipment*, 572(1):26 – 28, 2007. Frontier Detectors for Frontier Physics Proceedings of the 10th Pisa Meeting on Advanced Detectors, 2007.
- [31] K. W. Bell et al. Vacuum Phototriodes for the CMS Electromagnetic Calorimeter Endcap. *IEEE Transactions on Nuclear Science*, 51(5):2284–2287, 2004.
- [32] CMS HCAL Collaboration. The Compact Muon Solenoid (CMS) Hadron Calorimeter. *Nuclear Physics B Proceedings Supplements*, 78:182–185, 1999.

- [33] CMS Collaboration. The CMS magnet project: Technical Design Report. Technical Design Report CMS, 1997, CERN, Geneva.
- [34] *The CMS muon project: Technical Design Report*. Technical Design Report CMS. CERN, Geneva, 1997.
- [35] A. Kornmayer. The CMS Pixel Luminosity Telescope. *Nuclear Instruments and Methods in Physics Research Section A: Accelerators, Spectrometers, Detectors and Associated Equipment*, 824:304 – 306. Frontier Detectors for Frontier Physics: Proceedings of the 13th Pisa Meeting on Advanced Detectors, 2016.
- [36] J. Mans et al. CMS Technical Design Report for the Phase 1 Upgrade of the Hadron Calorimeter. 2012.
- [37] M. Guthoff and W. De Boer. Radiation Damage to the Diamond-Based Beam Condition Monitor of the CMS Detector at the LHC. CERN, Geneva, 2014, <https://cds.cern.ch/record/1977429>.
- [38] Anne Dabrowski. Upgrade of the CMS Instrumentation for Luminosity and Machine Induced Background Measurements. Technical Report, CERN, Geneva, 2014, CMS-CR-2014-362, <http://cds.cern.ch/record/1966978>.
- [39] S. Orfanelli et al. Design of a Novel Cherenkov Detector System for Machine Induced Background Monitoring in the CMS Cavern. Proceedings of the 2nd International Beam Instrumentation Conference IBIC, MOCL2, Oxford, UK, 2013.
- [40] A. Pozdnyakov et al. CMS Internal Note, 2013, CMS IN-2013/010.
- [41] O. R. Jones. Lhc beam instrumentation. Proceedings of the Particle Accelerator Conference PAC07, Albuquerque, New Mexico, USA, 2007, THXC01.
- [42] E. Castro et al. Performance of the Fast Beam Condition Monitor BCM1F in the CMS Experiment at LHC. Proceedings of European Workshop on Beam Diagnostics and Instrumentation for Particle Accelerators DIPAC2011, Hamburg, Germany, 2011, MOPD83.
- [43] A. Bell et al. Fast Beam Conditions Monitor BCM1F for the CMS Experiment. *Nuclear Instruments and Methods in Physics Research Section A: Accelerators, Spectrometers, Detectors and Associated Equipment*, 614(3):433 – 438, 2010.
- [44] J. Kaplon and W. Dabrowski. Fast CMOS Binary Front-End for Silicon Strip Detectors at LHC Experiments. In *Nuclear Science Symposium Conference Record, 2004 IEEE*, volume 1, pages 34–38 Vol. 1, 2004.
- [45] A. Bell et al. Fast Beam Conditions Monitor BCM1F for the CMS Experiment. Technical report. CERN, Geneva, 2009, arXiv:0911.2480, CMS-NOTE-2009-018.
- [46] G. Cervelli et al. A Radiation Tolerant Laser Driver Array for Optical Transmission in the LHC Experiments. Proceedings of the Seventh Workshop on Electronics for LHC Experiments, Stockholm, Sweden 2001.

REFERENCES

- [47] Jan K. Troska et al. Optical Readout and Control Systems for the CMS Tracker. *IEEE Trans. Nucl. Sci.*, 50(4):1067–72, 2003.
- [48] M. Nakahashi et al. Specification and Inspection Procedure for Analog Receiver Module. 2002, DOC-020308A.
- [49] CAEN S.p.A. *Technical Information Manual Mod.V1721-V1731, 8 CH. 8 BIT 500 MS/s 1 GS/s Digitizer*. Manual Rev. 22, 2013.
- [50] O. Novgorodova. *Characterisation and Application of Radiation Hard Sensors for LHC and ILC*. PhD thesis, Technical University of Brandenburg, Brandenburg, 2013. DESY-THESIS-2013-052, <http://www-library.desy.de/cgi-bin/showprep.pl?desy-thesis-13-052>.
- [51] D. Przyborowski. Development of Front-End Electronics for Beam-Condition Monitor at CMS. Contribution at the 1st ADAMAS Workshop, GSI, Darmstadt, 2012, <http://www-adamas.gsi.de/ADAMAS01/talks/przyborowski.pdf>.
- [52] A. A. Zagozdzińska. The CMS Fast Beams Condition Monitor Backend Electronics based on MicroTCA Technology. Technical Report, CERN, Geneva, 2015, CMS-CR-2015-315.
- [53] O. Karacheban. *Luminosity Measurements at CMS*. PhD thesis, BTU Cottbus, 2016. Work in progress.
- [54] Webpage of PICMG <https://www.picmg.org/openstandards/microtca/>.
- [55] Webpage of 4DSP <http://www.4dsp.com/fmc125.php>.
- [56] M. Penno. A Real-time Histogramming Unit for Luminosity and Beam Background Measurements for each Bunch Crossing at the CMS Experiment. *TWEPP 2013 - Topical Workshop on Electronics for particle Physics*. Perugia, Italy, 2013.
- [57] J. L. Leonard et al. Upgraded Fast Beam Conditions Monitor for CMS Online Luminosity Measurement. PoS, TIPP2014, page 346, 2014.
- [58] S. Müller. The Beam Condition Monitor 2 and the Radiation Environment of the CMS Detector at the LHC. PhD Thesis, Karlsruhe University, 2011, CERN-THESIS-2011-085 <http://cds.cern.ch/record/1319599>.
- [59] M. Hempel et al. Bunch-by-Bunch Beam Loss Diagnostics with Diamond Detectors at the LHC. Proceedings for 52nd Advanced Beam Dynamics Workshop on High-Intensity and High-Brightness Hadron Beams HB2012, Beijing China, 2012.
- [60] A. Gicquel et al. CVD Diamond Films: from Growth to Applications. *Current Applied Physics*, 1(6):479 – 496, 2001. <http://www.sciencedirect.com/science/article/pii/S156717390100061X>.
- [61] Paul W. May. Diamond Thin Films: A 21st-Century Material. *Philosophical Transactions of the Royal Society of London A: Mathematical, Physical and Engineering Sciences*, 358(1766):473–495, 2000. <http://rsta.royalsocietypublishing.org/content/358/1766/473>.

REFERENCES

- [62] Website, <http://www.chm.bris.ac.uk/pt/diamond/growthmodel.htm>, found on the 17.07.2016.
- [63] K. E. Spear and M. Frenklach. High Temperature Chemistry of CVD (Chemical Vapor Deposition) Diamond Growth. *Pure and Appl. Chem.* pp. 1773-1783, 1994.
- [64] G. Chiodini. Diamond Particle Detectors for High Energy Physics. pp. 37-42, 2011.
- [65] T. Behnke et al. The Charge Collection Properties of CVD Diamond. *Nuclear Instruments and Methods in Physics Research Section A: Accelerators, Spectrometers, Detectors and Associated Equipment*, 414(2-3):pp. 340 – 356, 1998.
- [66] C. Simons and R. Visincaa. Microstructuring of Diamonds with Laserlithography. *2nd ADAMAS workshop at GSI*, 2013. http://www-adamas.gsi.de/ADAMAS02/talks/simons_ADAMAS02.pdf.
- [67] F. Hartmann. *Evolution of Silicon Sensor Technology in Particle Physics*. Springer Tracts in Modern Physics Volume 231. Springer, Berlin Heidelberg, 2009.
- [68] J. Bol. Diamond beam monitors for intense primary particle beams. PhD Thesis, Karlsruhe University, 2006, IEKP-KA-2006-8, <http://www-ekp.physik.uni-karlsruhe.de/theses/phd/2006.html>.
- [69] E. Berdermann. Diamond for Particle and Photon Detection in Extreme Conditions. *Comprehensive Hard Materials*, Elsevier Science, p. 407-467, 2014, <http://repository.gsi.de/record/64853>.
- [70] C. Grupen and B. Schwartz. *Particle Detectors*. Cambridge University Press, The Edinburgh Building, Cambridge, UK, 2008.
- [71] K.A. Olive et al. (Particle Data Group). Passage of Particles Through Matter. *Chin. Phys. C*, 38, 090001 (2014) and 2015 update.
- [72] H. Bichsel. Straggling in Thin Silicon Detectors. *Rev. Mod. Phys.*, 60:663–699, 1988.
- [73] L. Landau. On the Energy Loss of Fast Particles by Ionization. *J. Phys. (USSR)*, 8:201–205, 1944.
- [74] P. V. Vavilov. Ionization Losses of High-Energy Heavy Particles. *Sov. Phys. JETP*, 5:749–751, 1957.
- [75] M. Barone et al. Astroparticle, Particle and Space Physics, Detectors and Medical Physics Applications. *Proceedings of the 9th Conference*. Villa Olmo, Como, Italy, 2005.
- [76] H. Pernegger et al. Measurements of Charge Carrier Properties in Single-Crystal CVD Diamond Using the Transient-Current Technique. *J. Appl. Phys.*, 97, 2005.
- [77] M. Pomorski. Electronic Properties of Single Crystal CVD Diamond and its Suitability for Particle Detection in Hadron Physics Experiments. PhD Thesis, Johann Wolfgang Goethe University, Frankfurt am Main, 2008, http://www-carat.gsi.de/publications/pomorski_thesis_final_LQ.pdf.

REFERENCES

- [78] C. Canali et al. Electrical Properties and Performances of Natural Diamond Nuclear Radiation Detectors. *Nuclear Instruments and Methods*, 160(1):73 – 77, 1979. <http://www.sciencedirect.com/science/article/pii/0029554X79901678>.
- [79] S. Ramo. Currents Induced by Electron Motion. *Proceedings of the IRE*, 27(9):584–585, 1939.
- [80] H. Spieler. *Semiconductor Detector Systems*. Oxford University Press, 2005.
- [81] L.S. Pan and D.R. Kania. *Diamond: Electronic Properties and Applications: Electronic Properties and Applications*. Electronic Materials: Science & Technology. Springer US, 1994. <https://books.google.de/books?id=ZtffEoXkU8wC>.
- [82] A. Oh. *CVD Diamant als Material für Teilchendetektoren*. PhD thesis, Hamburg University, 1999. DESY-THESIS-1999-022, <https://cds.cern.ch/record/403633/files/cer-000330326.pdf>.
- [83] M. Ohlerich. *Investigations of the Physics Potential and Detector Development for the ILC*. PhD thesis. PhD Thesis, TU Cottbus, 2010, <http://www-library.desy.de/cgi-bin/showprep.pl?desy-thesis-10-008>.
- [84] Website, <https://www.e6.com/>.
- [85] KEYENCE CORPORATION. Automatically Measure and Analyze 3D Surfaces. <http://www.keyence.com/ss/products/microscope/vkx/>.
- [86] E. Voekl et al. *Microscopy and Microanalysis 2002*, volume 8. Cambridge University Press, Microscopy Society of America, Microbeam Analysis Society, Microscopy Society of Canada, International Metallographic Society, 2002.
- [87] Keithley Instruments Inc. *Keithley-Model 6485 Picoammeter, Instruction Manual*. Cleveland, Ohio, U.S.A., 2001, Document Number: 6485-901-01 Rev. A.
- [88] Keithley Instruments Inc. *Keithley-Model 2410 1100V Source Meter, Service Manual*. Cleveland, Ohio, U.S.A., 1997, Document Number: 2410-902-01 Rev. B.
- [89] S. Muller et al. Study of leakage currents in pCVD diamonds as function of the magnetic field. 2009. [Phys. Status Solidi A206,2091(2009)].
- [90] CAEN S.p.A. *Technical Information Manual Mod.N625*. Manual Rev. 3, 2004.
- [91] CAEN S.p.A. *Technical Information Manual Mod.V965/V965A*. Manual Rev. 8, 2008.
- [92] CAEN S.p.A. *Technical Information Manual Mod.V844/N844P/N845*. Manual Rev. 7, 2011.
- [93] CAEN S.p.A. *Technical Information Manual Mod.V993*. Manual Rev. 3, 2004.
- [94] T. Tachibana et al. Correlation of the Electrical Properties of Metal Contacts on Diamond Films with the Chemical Nature of the Metal-Diamond Interface. II. Titanium Contacts: A Carbide-Forming Metal. *Phys. Rev. B*, 45:11975–11981, 1992. <http://link.aps.org/doi/10.1103/PhysRevB.45.11975>.

REFERENCES

- [95] T. Behnke et al. 2007, EUDET-Memo-2007-11.
- [96] D. Cussans. Description of the JRA1 Trigger Logic Unit (TLU), v02c. 2009, EUDET-Memo-2009-4.
- [97] E. Corrin. The EUDET High Resolution Beam Telescope - The Final Digital Readout . *EUDET-Memo-2009-6*, November 2009.
- [98] J.Behr. Test Beam Measurements with the EUDET Pixel Telescope. 2010, EUDET-Report-2010-01.
- [99] J. Baudot et al. First Test Results of MIMOSA-26, A Fast CMOS Sensor With Integrated Zero Suppression and Digitizer Output. *IEEE NSS*, 2009.
- [100] A. Cotta Ramusino. The EUDET Data Reduction Board (EUDRB). 2008, EUDET-Memo-2008-38.
- [101] ROOT, Data Analysis Framework, Copyright CERN 2014-17, <https://root.cern.ch/>.
- [102] E. Corrin. EUDAQ Software User Manual. 2010, EUDET-Memo-2010-01.
- [103] Eutelescope Class List. <http://ilcsoft.desy.de/Eutelescope/current/doc/html/annotated.html>.
- [104] P. Niezurawski and A.F. Zarnecki. EUDET Telescope Geometry and Resolution Studies. 2007, *EUDET-Report-2007-01*.
- [105] D. M. Caughey, R. E. Thomas, and K. W. Bell et al. Carrier Mobilities in Silicon Empirically Related to Doping and Fieldp. *Proc. of the IEEE*, 55:2129, 1967.
- [106] M. Pomorski. Electronic Properties of Single Crystal CVD Diamond and its Suitability for Particle Detection in Hadron Physics Experiments. *PhD Thesis*, 2008.
- [107] S. Schuwalow. Polarization Effects in Radiation Damaged scCVD Diamond Detectors. Contribution at the 4th NoRHdia Workshop, GSI, Darmstadt, 2008 http://www-norhdia.gsi.de/talks/4th/S_Schuwalov.pdf.
- [108] E. Berdermann et al. Performance of Diamond Detectors in a Fragmentation Experiment. *Proceedings of the Nuclear Physics Conference in Bormio*, 2007.
- [109] R. F. Holsinger. Superfish-A Computer Program for Evaluation of RF Cavities with Cylindrical Symmetry. *Particle Accelerators* 7, pages 213–222, 1976.
- [110] M. Hempel et al. Measurements of the Performance of a Beam Condition Monitor Prototype in a 5 GeV Electron Beam. *Nuclear Instruments and Methods in Physics Research A*, 826:65–71, 2016. <http://www.sciencedirect.com/science/article/pii/S0168900216302108>.
- [111] S. van der Meer. Calibration of the effective beam height in the ISR. Technical report. CERN, Geneva, 1968, CERN-ISR-PO-68-31. ISR-PO-68-31, <https://cds.cern.ch/record/296752>.

REFERENCES

- [112] T. Pieloni et al. Emittance Growth due to Beam-Beam Effects with a Static Offset in Collision in the LHC. In *Particle accelerator. Proceedings, 23rd Conference, PAC'09, Vancouver, Canada, 2009*. <http://accelconf.web.cern.ch/AccelConf/PAC2009/papers/we6pfp039.pdf>.
- [113] W. Herr. Effects of PACMAN bunches in the LHC. 1996. CERN-LHC-PROJECT-REPORT-039.
- [114] D. Belohrad, L.K. Jensen, O.R. Jones, M. Ludwig, and JJ Savioz. The LHC Fast BCT system: A comparison of Design Parameters with Initial Performance. Technical report, CERN, Geneva, 2010. CERN-BE-2010-010, <https://cds.cern.ch/record/1267400>.
- [115] W. Höfle. Transverse Damper. *Proceedings of Chamonix 2012 Workshop on LHC Performance*. p. 157, Geneva, CERN, 2012, <http://cds.cern.ch/record/1424362>.
- [116] D. Boussard, W. Höfle, and T. P. Linnecar. The LHC Transverse Damper (ADT) Performance Specification. Technical report. CERN, Geneva, 2000, SL-Note-99-055-HRF, <https://cds.cern.ch/record/702559>.

Acknowledgment

Zum Schluss möchte ich mich bei allen bedanken, die mir diese Arbeit ermöglicht haben und die mir mit Rat und Tat beiseite standen.

Als erstes möchte ich mich dabei vor allem bei Prof. Dr. Lohmann bedanken, der mich dabei unterstützte, mich für eine Technical Student Position am CERN zu bewerben und dort für 1 Jahr zu arbeiten. Nach dieser einmaligen Erfahrung durfte ich dann in seiner CMS Gruppe am DESY Zeuthen eine Doktorstelle antreten. Während dieser Zeit habe ich viel gelernt, nicht nur in Sachen Diamantsensoren, sondern auch auf vielen anderen Gebieten wie z.B. der Organisation, Stressbewältigung und Teamwork. Vielen Dank für diese Erfahrung und die Möglichkeit einen Traum wahr werden zu lassen, einmal einen Dokortitel zu erhalten. Während meiner Schulzeit habe ich nie damit gerechnet, dass mir das einmal ermöglicht wird. Besonders eines bleibt mir für ewig in Erinnerung "Machen Sie Fehler, aber machen Sie diese nicht mehrmals".

Desweiteren möchte ich mich noch einmal bei Rüdiger Schmidt bedanken, in dessen Gruppe ich am CERN für ein Jahr arbeiten durfte. Während dieser Zeit habe ich nicht nur viel über Beschleunigerphysik und den LHC gelernt, sondern auch wunderbare Menschen kennen gelernt und viele tolle Erlebnisse gehabt. Hiermit möchte ich mich auch bei Najoua Kachouri und ihrer Familie bedanken, die für mich in diesem Jahr wie eine zweite Familie zu mir waren. Ich möchte mich aber auch für die tollen Erlebnisse mit Florian, Nerea, Maitane, Jiri, Jakub, James, ... bedanken.

Während meiner Zeit am DESY habe ich auch immer viel Unterstützung von vielen Leuten erhalten. Ich bedanke mich bei Elena Castro-Carballo, Sergey Schuwalow, Wolfgang Lange und Hans Henschel für alle Fragen, die sie mir beantwortet haben und mir immer Ratschläge gegeben haben. Nicht unbenannt sollen meine tollen Kollegen bleiben, die mir viel mit ihren Gesprächen geholfen haben und mich immer auf neue Ideen und Ansätze gebracht haben. Dabei möchte ich mich insbesondere bedanken bei Olena Karacheban, Konstantin Afanaciev, Martin Stegler und Jessica Leonard. Vielen Dank auch für die tollen gemeinsamen Abende an Sam, Elias und Jason. Ohne die Hilfe und sehr schnelle Arbeit der Werkstätten wäre auch der Test-Beam nie zustande gekommen. Deswegen möchte ich mich ganz doll für diese Arbeit bei der DESY Elektronik und Mechanik Werkstatt bedanken, besonders aber bei Jürgen Pieper.

Vielen Dank auch an die BRIL Gruppe am CERN für den Erfahrungsaustausch und die Unterstützung bei allen Messungen, die ich gemacht habe. Die On-Call Schichten waren zwar nicht schön, aber man hat viel dabei gelernt und die komplexen Zusammenhänge verstanden.

Einmal im Jahr findet der ADAMAS Workshop über Diamantsensoren statt, den ich fachlich sehr genossen habe. Vielen Dank an alle Leute, die diesen Workshop organisieren und auch an alle Teilnehmer. Der Workshop war mir immer wichtig und hat viel zum Erfahrungsaustausch beigetragen. Danke auch für die tolle Gesellschaft während des Workshops.

Vielen Dank auch an die Universitäts-Mitarbeiter der BTU Cottbus für das tolle Physik-Studium. Keine andere Universität hätte ich mir ausgesucht. Dabei möchte ich mich besonders bei Prof. Dr. Besthorn und Prof. Dr. Reif bedanken, bei denen ich unter anderem Übungen leiten durfte.

Am Ende möchte ich mich bei meinen Freunden bedanken. Viele meiner Freunde haben mir oft zugehört und meine Sorgen und Ängste ernst genommen. Sie haben mich immer unterstützt, auch wenn die Zeit für sie immer zu kurz geraten ist. Vielen Dank an Lisa, Julia, Lena, Andi, Eike und die Mainz Gang.

Vom Herzen möchte ich mich auch besonders bei meiner Familie bedanken. Ohne euch hätte

ich kein Physik studiert und ohne die finanzielle Unterstützung hätte ich dieses Studium auch nicht so schnell durchziehen können. Vielen Dank an meine Eltern und Partner, Schwester und Großeltern. Ganz zum Schluss möchte ich mich bei Hannes bedanken. Oft weiß ich nicht, wie ich diese Dankbarkeit zum Ausdruck bringen kann. Er stand mir immer bei und hat mich in jeder Lebenslage unterstützt und mich ermutigt, dass wir alles schaffen können und auch geschafft haben. Das größte Glück dabei ist wohl unser Sohn, der mir schon jetzt, mit seinem knapp 2 Jahren, so vieles gelehrt hat. Danke für diese kleine Familie.

Lebenslauf

Persönliche Daten

Name	Maria Hempel
Geburtsdatum	28. September 1987
Geburtsort	Berlin
Familienstand	ledig, 1 Kind

Ausbildung

02/2013 - 02/2017	Promotion, BTU Cottbus <i>Doktorarbeit am DESY Zeuthen</i>
09/2010 - 01/2013	Master of Science (Physik), BTU Cottbus, Masterarbeit am CERN mit Kooperation des DESY: <i>“Application of Diamond Based Beam Loss Monitors at LHC”</i>
10/2007 - 09/2010	Bachelor of Science (Physik) Bachelorarbeit am DESY Zeuthen: <i>“Study of the Performance of the Data Acquisition Chain for BCM1F Software Upgrade”</i>
09/2000 - 06/2007	Abitur, Berlin

Berufserfahrung

01/2013 - 12/2013	Technical Student, CERN, Genf <i>Datenauslese und Analyse von Diamantsensoren</i>
08/2011 - 10/2011	Wissenschaftliche Mitarbeiterin, DESY, Zeuthen <i>Elektrische Vermessungen von Diamantsensoren</i>
04/2011 - 07/2011	Studentische Hilfskraft, BTU Cottbus <i>Leitung und Betreuung von Übungen der Theoretischen Physik</i>
08/2009 - 09/2009	Wissenschaftliche Mitarbeiterin, BESSY, Berlin <i>Spektroskopische Vermessung von Silizium Sensoren</i>

Veröffentlichungen

HB2012 Konferenz	M. Hempel et al. <i>“Bunch-by-Bunch Beam Loss Diagnostics with Diamond Detectors at the LHC”, 52nd Advanced Beam Dynamics Workshop on High Intensity and High Brightness Beams, MOP203, Beijing, China</i>
IBIC2013 Konferenz	M. Hempel et al. <i>“Performance of Detectors Using Diamond Sensors at the LHC and CMS”, MOPC43, 2nd International Beam Instrumentation Conference Oxford, UK</i>
IBIC2014 Konferenz	M. Hempel et al. <i>“Performance of the Fast Beam Condition Monitor at CMS”, MOPD03, 3rd International Beam Instrumentation Conference, Monterey, USA</i>
NIM-A Journal	M. Hempel et al. <i>“Measurements of the Performance of a Beam Condition Monitor Prototype in a 5GeV Electron Beam”, Nuclear Instruments and Methods in Physics Research A, 826 (2016) Seite 65-71</i>